Analysis of Solidification and Porosity in Aluminium Casting

Thesis submitted by

Samir Chakravarti

Doctor of Philosophy (Engineering)

Department of Mechanical Engineering
Faculty Council of Engineering & Technology
Jadavpur University
Kolkata, India

2023

JADAVPUR UNIVERSITY
KOLKATA- 700 032, INDIA

Index No. 296/16/E

1. Title of the thesis:

Analysis of Solidification and Porosity in Aluminium Casting

2. Name, Designation & Institution of the Supervisor :

Dr. Swarnendu Sen
Professor
Department of Mechanical Engineering,
Jadavpur University
Kolkata- 700 032, India

3. List of Publications :

Journal Publications:

1. Chakravarti, S., Sen, S., & Bandyopadhyay, A. (2018). A study on solidification of large iron casting in a thin water cooled copper mould. Materials Today: Proceedings, 5(2), 4149-4155.
2. Chakravarti, S., & Sen, S. (2023). An investigation on the solidification and porosity prediction in aluminium casting process. *Journal of Engineering and Applied Science*, *70*(1), 1-24.
3. Chakravarti, S., & Sen, S. (2023). Simulation of Commencement and Size of the Hot Spot in Permanent Mould Casting. *Key Engineering Materials*, *941*, 11-18.
4. Chakravarti, S., & Sen, S. (2023). Study on the Behaviour of Surface Wear and Friction for a Pure Aluminium Casting Product Using Permanent Mould. *Key Engineering Materials*, *944*, 41-49.
5. Samir Chakravarti and Swarnendu Sen. Simulation Modelling of Solidification and Porosity Formation in Aluminium Casting: Investigating the Influence of Casting Parameters (Under preparation).
6. Samir Chakravarti and Swarnendu Sen. Evaluating the Effects of Mould Preheating on Porosity in Permanent Mould Casting Process (Under preparation).

International Conference Publications:

1. Chakravarti, S., & Sen, S. (2023). "A Study on Solidification of Aluminium Casting in Steel Mould." 2nd International Conference on Energy Resources & Technologies for Sustainable Development (ICERTSD 2023), Department of Mechanical Engineering, Indian Institute of Engineering Science and Technology, Shibpur (accepted).

4. List of Patents : NIL

5. List of Presentations in National/ International Conferences/Workshops:

International Conferences

1. Chakravarti, S., & Sen, S. (2023). "A Study on Solidification of Aluminium Casting in Steel Mould." 2nd International Conference on Energy Resources & Technologies for Sustainable Development (ICERTSD 2023), Department of Mechanical Engineering, Indian Institute of Engineering Science and Technology, Shibpur
2. Chakravarti, S., & Sen, S. (2022). "Study on the behaviour of surface wear and friction for a pure aluminium casting product using permanent mould." International Conference on Aspects of Materials and Mechanical Engineering (ICMME 2022), GLA University, Mathura, India.
3. Chakravarti, S., & Sen, S. (2022). "Simulation of Commencement and Size of the Hot Spot in Permanent Mould Casting." International Conference on Modern Materials for Engineering and Research (ICMMER 2022), Sengunthar Engineering College, Tiruchengode, Tamil Nadu, India.

"Statement of Originality"

I ***Samir Chakravarti*** registered on ***4th July, 2016*** do hereby declare that this thesis entitled "***Analysis of Solidification and Porosity in Aluminium Casting"*** contains literature survey and original research work done by the undersigned candidate as part of Doctoral studies.

All information in this thesis have been obtained and presented in accordance with existing academic rules and ethical conduct. I declare that, as required by these rules and conduct, I have fully cited and referred all materials and results that are not original to this work.

I also declare that I have checked this thesis as per the "Policy on Anti Plagiarism, Jadavpur University, 2019", and the level of similarity as checked by iThenticate software is **03 %**.

Samir Chakravarti
Signature of the candidate:

Date: 26/06/2023

Certified by the Supervisor
(Signature with date, seal)

Professor
Dept. of Mechanical Engineering
Jadavpur University, Kolkata-32

CERTIFICATE FROM THE SUPERVISOR

This to certify that the thesis entitled "**Analysis of Solidification and Porosity in Aluminium Casting**" submitted by **Shri Samir Chakravarti,** who got his name registered **on 4th July, 2016** for the award of Ph. D. (Engineering) degree of Jadavpur University is absolutely based upon his own work under the supervision of **Prof. Swarnendu Sen** and that neither his thesis nor any part of the thesis has been submitted for any degree/diplomaor any other academic award anywhere before.

Swarnendu Sen 26/6/2023

.....

Signature of the Supervisor
and date with Office Seal

Professor
Dept. of Mechanical Engineering
Jadavpur University, Kolkata-32

Dedicated to the cherished memory of Prof. Asish Bandyopadhyay, whose guidance and wisdom continue to inspire me, even in his absence.

ACKNOWLEDGEMENT

I would like to pay tribute to Late Prof. Asish Bandyopadhyay, whose wisdom and guidance have left an indelible mark on my academic journey. Though he is no longer with us, his teachings and mentorship continue to influence my work. I am forever grateful for his profound knowledge, intellectual rigor, and passion for research.

I extend my sincere appreciation to my respected supervisor, Prof. Swarnendu Sen, for his expertise, dedication, and constant encouragement. His insightful feedback, constructive criticism, and unwavering support have pushed me to strive for excellence. I am grateful for his guidance, which has been a source of inspiration for me. Working under their supervision has been an absolute pleasure for me. I am truly grateful to my supervisor for their immense contribution and support, without which I would not have been able to complete this dissertation. I am indebted to him for his guidance and assistance throughout the process.

I express my heartfelt gratitude to the Head and former Heads of the Mechanical Engineering Department at Jadavpur University for their invaluable support. Their guidance and support were instrumental in the successful completion of this work. Furthermore, I would like to acknowledge and express my gratitude to Jadavpur University for providing me with the necessary resources and environment to pursue my research. The support and opportunities offered by the university have been instrumental in shaping my academic and research endeavours. Additionally, I would like to express my appreciation to the faculty members, staff, and fellow researchers at Jadavpur University who have contributed to my growth and learning. I would like to express my appreciation to my colleagues at Kalyani Government Engineering College for their support. Their collaborations and discussions have enriched my research experience.

I am indebted to my parents, Late Rabindranath Chakravarti and Tapati Chakravarti, for their unending love, support, and belief in my capabilities. Their sacrifices and unwavering faith in my abilities have been a constant source of motivation. I am grateful to my beloved wife, Debasrita, who has been my pillar of strength and immense source of both intellectual and emotional support. I would also like to extend my gratitude to my son, Samadarshi, whose innocent presence and infectious laughter has been a constant reminder of what truly matters. I am grateful to my extended family for their unwavering support and encouragement throughout this journey.

Lastly, I extend my gratitude to all those who have directly or indirectly contributed to this research. Their assistance, feedback, and support have been invaluable, and I am thankful for their contributions.

Date: 26/06/2023

Place: Jadavpur

Samir Chakravarti

(Samir Chakravarti)

CONTENTS

Page No.

ABSTRACT

This thesis explores metal casting, specifically the permanent mould casting of aluminium in steel mould. The advantages of permanent mould casting, including cost-effectiveness and high-quality part production, are discussed. The significance of the solidification process in metal casting is examined, considering factors that affect casting quality, strength, and characteristics. Techniques for predicting and reducing porosity defect in casting are explored. The thesis proposes the use of Ansys Fluent simulation software to enhance the casting process. Computational fluid dynamics (CFD) models are highlighted for their ability to reduce trial-and-error testing and provide insights into mould filling, solidification, cooling, and porosity defect detection. The thesis aims to create a CFD model that comprehensively analyses the solidification process from the start of metal pouring. By optimizing casting parameters and minimizing porosity, the study seeks to improve casting quality. The CFD model predicts porosity location and identifies areas with the highest porosity, enabling better control of the solidification process. The study focuses on permanent mould casting of pure aluminium with a steel mould. One-dimensional casting solidification models estimate solidification time and front, while a three-dimensional model using Ansys Fluent simulates the process more extensively. The model considers air and aluminium as a two-phase system and turbulent flow within the mould cavity. It allows for variations in pouring velocity, pouring temperature, and mould initial temperature. The study explores the importance of parameters related to porosity defects and their impact on casting quality. Optimal pouring velocity and temperature are determined to reduce porosity. The length of fully-filled solid aluminium and the presence of a solid aluminium-air layer are analysed. The findings reveal the influence of pouring parameters on porosity formation and propose strategies to minimize porosity. The thesis concludes by summarizing the research's contributions, identifying areas for further investigation, and acknowledging encountered limitations and challenges. Continued research in aluminium casting with metal mould is encouraged to advance the field

NOMENCLATURE

Symbols	Description	Unit
A	Area	mm^2 or m^2
B	Constant	-
b	Breadth	mm
C	Constant	-
C_β	Constant	-
$C_{\varepsilon 1}$	Model constant	-
$C_{\varepsilon 2}$	Model constant	-
$C_{\varepsilon 3}$	Constant by which ε is affected from the buoyancy	-
C_μ	Model constant	-
C_{mush}	Mushy zone constant	-
c or c_p	Specific heat at constant pressure	J/kg K
δ	Volumetric coefficient of thermal expansion	K^{-1}
d	Depth	mm
D	Diameter	mm
E	Total energy	J/kg
e	Relative error	-
ε	Turbulent dissipation rate	J/(kg·s
$erf(\zeta)$	Error function	-
$erfc(\zeta)$	Complementary error function	-
$\vec{F}$	Source term vector	N
γ	Kinematic viscosity	m^2/s
$\vec{g}$	Gravitational vector	m/s^2
g_i	Gravitational vector in the i-th direction	m/s^2

G_b	Turbulence kinetic energy due to the buoyancy	N/kg
G_k	Generation of turbulence kinetic energy due to the mean Velocity gradients	N/kg
g_r	Grid refinement ratio	-
GCI	Grid convergence index	-
H	Height	mm
h	Enthalpy	J/kg
h_1	Sensible heat	J/kg
h_2	Latent heat	J/kg
h_c	Convection heat transfer coefficient	W/m^2 K
ΔT	Difference in temperature	K
η	Integration variable	-
η_0	Constant	-
k	Turbulent kinetic energy	J/kg
K_m	Mould constant	-
L_o	Length of the outside wall surface	mm or m
L	Latent heat of solidification	J/kg
ℓ	Length	mm
λ	Theramal conductivity	W/m K
$\dot{m}$	Mass transfer rate	kg/s
μ	Viscosity	kg/m s
ρ	Density	kg/m^3
oc	Order of convergence	-
p	Pressure	N/m^2
Pr	Prandtl number	-
φ	Volume fraction	-
Ra	Rayleigh number	-

Re	Reynolds number	-
R_ε	Correction factor	N/kg
R_{ij}	Reynolds stress tensor	N/m²
$s(t)$	Depth of solidification	mm or m
S	Modulus of the mean rate-of-strain tensor	s^{-1}
S_{ij}	Mean rate of strain tensor	s^{-1}
$\bar{\bar{\tau}}$	Stress tensor	N/m²
T	Temperature	K
T_0	Mould initial temperature or mould temperature or mould preheat temperature	K
T_S	Wall surface temperature	K
T_f	Freezing temperature	K
T_F	Mean film temperature	K
T_i or T_p	Initial liquid temperature or pouring temperature	K
T_∞	Constant of integration	-
t	Time	s
t_p	Pouring time	s
t_s	Solidification time	s
u	Velocity	mm/s or m/s
u_i	Velocity component in the i-th direction	-
$\acute{u}$	Fluctuating component of velocity	mm/s or m/s
u_i'	Fluctuating velocity in the *i*-th direction	mm/s or m/s
$\overline{u}$	Mean component of velocity	mm/s or m/s
$\vec{v}$	Velocity vector	mm/s or m/s
v_p	Pouring velocity	mm/s
x	Distance from mould-casting interface	mm or m

x_i	Spatial coordinate in the i-th direction	-
ψ	Scalar quantity	-
ϵ	Constant	-
ζ	Constant	-
α	Thermal diffusivity	m^2/s
$\propto_k$	Inverse effective Prandtl number for k equation	-
$\propto_\varepsilon$	Inverse effective Prandtl number for ε equation	-
V	Volume	mm^3

Suffixes/ Abbreviations:

Terms	**Meaning**
a	Air
Al	Aluminium
c	Casting
eff	Effective
li	Liquidus
l	Liquid phase
r	Riser
s	Solid phase
so	Solidus
sp	Sprue
st	Steel
t	Turbulent
CFD	Computational fluid dynamics
RANS	Reynolds-averaged Navier-Stokes equations
VOF	Volume of fluid

List of Figures

Page No.

List of Tables

Page No.

CHAPTER 1: INTRODUCTION AND BACKGROUND

1.1 Introduction

The process of metal casting has been around for thousands of years and is still widely used today in a variety of industries. The technique involves heating a material until it becomes a liquid by using a furnace, after which it is poured into a pre-prepared mould cavity where it solidifies. Once the product has solidified, it is removed from the mould cavity. Then it is trimmed, and cleaned to shape [1]. Metal casting is an important process for producing large quantities of parts efficiently and cost-effectively [2, 3]. There are several types of metal casting processes used in manufacturing like sand casting, investment casting, die casting, permanent mould casting etc. [1].

Permanent mould casting offers several advantages over other casting methods [4, 5]. Permanent mould casting is a highly efficient and cost-effective process for producing high-quality parts with excellent dimensional accuracy, surface finish, and mechanical properties. The process involves the use of durable moulds made of materials that can withstand repeated use and maintain their shape over time. The moulds can be reused hundreds or even thousands of times, making the process ideal for producing large quantities of parts. Permanent mould casting is faster than other casting methods and can produce complex-shaped parts with intricate details. These advantages make it an ideal casting method for many different industries, from automotive to aerospace.

The permanent mould casting can be used to produce parts from a wide range of metals and alloys, allowing for the production of parts with different mechanical properties and corrosion resistance. Among the metals, the casting of aluminium has recently received a lot of attention because of their extensive industrial applications and great technological value. This is because of its many benefits including lightweight, good strength-to-weight ratio, high thermal

conductivity, exceptional corrosion resistance, high castability, and desirable tensile strength [6, 7, 8, 9]. Aluminium is therefore widely employed, particularly in the mechanical automobile and aerospace industries [7, 8, 9].

The selection of a suitable mould material is an important consideration in permanent mould casting. Steel have several advantages over other materials [10] and therefore, the present thesis used steel as mould. Steel is preferred due to their strength, durability, and ability to withstand high temperatures and pressures. They also have high thermal conductivity, which enables faster cooling and solidification of castings, improving their mechanical properties. Steel moulds can be machined to tight tolerances, producing precise castings suitable for aerospace or medical applications. Additionally, steel moulds can produce smooth surface finishes, reducing the need for further finishing operations, which is important for automotive or consumer products.

Once the solidification process is complete, the product is removed from the mould. Solidification is an important step in metal casting, whereby the liquid metal cools and solidifies inside the mould cavity, transforming into a solid material. Seetharamu et al. [11] pointed out that the solidification process in metal casting is a complex phenomenon. The quality and characteristics of the final product in metal casting are influenced by the process of solidification as stated by Galantucci and Tricarico [12]. The grain structure and associated properties of a casting are influenced by the solidification rate or cooling rate [13].

According to Mohapatra et al. [13], the pouring velocity, pouring temperature, mould temperature, and mould material can be individually or collectively chosen to create a desired thermal gradient in the melt, which determines the solidification rate. The mould material impact the solidification process, as certain materials may have a greater or lesser thermal conductivity than others, affecting the cooling rate of the metal.

The solidification rate is determined by the rate at which heat is dissipated from the molten metal and the solidification time depends on cooling rate. Solidification time is the time taken for the molten metal to transform from liquid state into a solid state during the casting process.

Solidification time is a critical parameter in metal casting that determines the final product's quality, strength, and characteristics such as ultimate tensile strength, ductility and fatigue properties [14, 15]. During the casting solidification process, the air can become trapped in the metal and result in air porosity (porosity) defect. The choice of mould material affects the formation of porosity. Some mould materials, such as green sand moulds, have a higher potential for porosity formation than other materials, such as ceramic or metallic moulds [16].

The pouring temperature of the molten metal can also impact the formation of air porosity. If the temperature is too low, the molten metal will solidify too quickly, and porosity can occur. On the other hand, if the temperature is too high, it can lead to the formation of entrained gas porosity [17]**.** One of the main causes of porosity in aluminium casting is pouring velocity. When the pouring velocity of the molten metal is too slow, the metal can begin to solidify prematurely before it has completely filled the mould cavity. This can result in the formation of gas pockets or voids in the casting [18]**.** The pouring temperature, pouring velocity, and mould temperature influence the solidification time and the porosity in the casting. The selection and control of these parameters are essential for avoiding porosity.

1.2 Literature Survey

1.2.1 Permanent Mould Casting

There are many casting processes with varying capabilities. Selecting the appropriate casting process for producing a component is necessary as stated by Daws et al. [19]**.** Choosing an unsuitable process can result in financial loss and a decrease in market share. A outline of advisory casting process selection system has been presented by Daws et al. [19]**.** It was stated that sand casting take long time to produce a part than permanent mould casting. Permanent mould casting is preferable to sand casting for mass production. Fatigue testing was carried out on sand cast and permanent mould cast specimens by Linder et al. [20]**.** The fatigue properties could be improved in the product if permanent mould casting is used**.**

Suthar et al. [15] and Vignesh [21] stated the permanent mould casting allows for the production of high-quality parts with excellent dimensional accuracy, surface finish, and mechanical properties. This is because the moulds are made of durable materials that can withstand repeated use and maintain their shape and integrity over time. Jorstad [22] stated the permanent mould casting process is faster than other casting methods, such as sand casting or investment casting. This is because the moulds are preheated and can be used immediately after the previous casting has been removed.

Otarawanna and Dahle [23] stated permanent mould casting allows for the production of complex-shaped parts with intricate details, such as thin walls and internal cavities. This makes it ideal for producing parts with complex geometries, such as engine blocks, transmission cases, and turbine blades.

Peters [24] stated permanent mould casting can be used to produce parts from a wide range of metals and alloys, including aluminium, brass, bronze, and magnesium. This allows for the production of parts with different mechanical properties and corrosion resistance.

1.2.2 Modelling of Metal Casting Process

Over the years, there has been significant progress in the modelling of metal casting processes. Initially, the focus was on ideal metals and alloys under controlled laboratory conditions. However, with advancements, the scope of modelling has expanded to include the complexity of industrial processing of commercial metals and alloys. Initially, solidification modelling was limited to closed-form solutions using the Bernoulli equation. This was later utilized by Ruddle [25] to design gating systems, and the calculations were integrated with empirical knowledge and engineering principles commonly employed by foundry engineers. With the development of digital computers, these calculations were incorporated into computer-aided design programs. Szekely et al. [26] used continuum mechanisms in continuous casting, and these models were useful for turbulent flow in continuous casting designs and gas-stirred ladles. Metal casting is a complex process that involves several stages, including mould filling, solidification, and cooling. Modelling the casting process is important to optimize the process, minimize defects

and improve quality. Modelling of metal casting processes involves the use of mathematical equations to predict the behaviour of molten metal during the casting process. There are several types of models used in metal casting, including empirical, analytical, and numerical models.

Empirical models are based on the experimental data obtained from the casting process [27]. These models are useful in predicting the behaviour of molten metal during the casting process, but they lack the accuracy and precision of analytical and numerical models. Analytical models [28, 29] use mathematical equations to predict the behaviour of molten metal during the casting process. These models are useful in understanding the physics of the process, but they are limited by the complexity of the process and the assumptions made during model development. Numerical models use computational fluid dynamics (CFD) techniques [30] to simulate the behaviour of molten metal during the casting process. These models are the most accurate and precise, but they are also the most complex and time-consuming.

In terms of modelling complexity, a casting process can be divided into two stages: mould filling and phase change (from liquid to solid). Computational fluid dynamics (CFD) principles can be used for modelling the flow of molten metal during mould filling [31]. CFD models can be used [32, 33] to simulate the flow of molten metal, heat transfer, and solidification processes in a casting to predict the formation of defects such as shrinkage, porosity, and hot tears. Recent research has focused on developing more accurate and efficient models for predicting solidification behaviour in metal castings. The modelling may be done either using mesh or without a mesh.

The mesh-based models utilize a mathematical approach that involves dividing the entire problem domain into small sections, known as control volumes or elements. This technique is used to solve complex problems by applying equations to each of these sections individually. Finite difference or volume (FVM) and finite element (FEM) methods are commonly used for numerical modelling of casting processes. The conservation equations of heat, mass, and momentum govern the casting process, and these equations are well-established in the literature [34]. Dedicated or general-purpose software can be employed to acquire computed outcomes

from a casting model. Various software such as Magma-Soft [4, 35], Pro-Cast [36], Nova-Flow [4, 37] Any-Casting [38], Solid/Flow/Opti-Cast [4], Flow-3D [4], ANSYS-CFX [39], ANSYS-FLUENT [40], etc. are available to model different aspects of casting processes.

Meshless methods [41, 42], also known as mesh-free methods, are a type of numerical method that utilizes a set of nodes that are arbitrarily distributed without the extra topological relationships between them. This approach provides an alternative to finite element or finite volume methods and solely necessitates a collection of uniformly (consistently) or non-uniformly distributed computational nodes within the domain of computation. Meshless methods are a promising technique for avoiding problems associated with polygonisation, and there are several available methods that are described in the literature [41, 42, 43]. Cleary et al. [44] pointed out that Smooth Particle Hydrodynamics (SPH) is an example of a meshless method that has been successfully employed by researchers to model various casting processes. Smooth Particle Hydrodynamics has been successfully applied in primary casting of foundry ingots and high-pressure die casting scenarios. It accurately captures phenomena such as the fragmentation of metal streams into droplets and the possibility of oxide entrainment, which can be challenging for meshed methods when it comes to resolving droplet sizes [45].

According to Jolly and Katgerman [46], with the ongoing improvement in computer and processor capabilities, it is now possible to model various phenomena involving multiple physics, such as free surface flow, heat and fluid flow, and thermal stress, at a macroscopic level. However, effectively integrating these computed results into real casting processes and accurately predicting performance still presents a significant challenge. This obstacle needs to be overcome in order to achieve widespread success and applicability of casting modelling as a valuable tool for manufacturing firms. At present, a significant portion of current casting modelling efforts are focused on defect prevention, such as mitigating porosity, thermal cracks, and macro-segregation [47, 48].

Khan and Sheikh [4] emphasized that simulation models play a crucial role in minimizing casting defects by offering a virtual environment for testing various casting designs and

parameters prior to actual production. These models use computational fluid dynamics (CFD) software to simulate the flow of molten metal in the mould and the subsequent solidification process [49]. By adjusting parameters such as pouring temperature, filling rate, and mould design, engineers can identify potential defects such as air porosity, shrinkage, and hot spots and make the necessary adjustments to prevent or minimize them [50]. Additionally, simulation models can help optimize casting production by reducing the need for physical prototypes and experimental testing. This saves time and resources while also improving the quality of the final product.

Ge et al. [51] highlighted that Ansys Fluent is an example of a simulation model utilized in casting for detailed modelling of the fluid dynamics and heat transfer processes involved in casting. The software can simulate different types of casting processes, such as gravity casting, low-pressure casting, and high-pressure die casting. By using Ansys Fluent, engineers can predict and prevent defects such as porosity, misruns, resulting in higher-quality castings and increased production efficiency. ANSYS Fluent is widely used computational fluid dynamics (CFD) software that can be utilized in casting simulations to predict the flow of molten metal and the formation of defects during the casting process [52]. By inputting the physical properties of the molten metal and the mould material, as well as the boundary conditions and initial conditions of the system, Ansys Fluent can simulate the flow of the metal as it fills the mould cavity, including the formation of hot spots, porosity, and other types of defects. The Ansys Fluent software can also be used to study the effects of various casting process parameters on the formation of defects, such as the pouring temperature, filling rate, and average cooling rate [53]. This allows engineers to optimize the casting process to minimize defects and improve the quality of the final product.

1.2.3 Solidification in Casting

Solidification is a fundamental and critical stage in the metal casting process, which determines the final microstructure and properties of the casting. It is a complex phenomenon that occurs when the temperature of the molten metal drops below its melting point, causing it to transform

from a liquid to a solid state. The solidification process is accompanied by a phase change from liquid to solid, which results in the formation of a crystalline structure [54]. The solidification process in metal casting involves several stages. Initially, the molten metal is poured into a mould, and as it cools, it begins to solidify from the surface of the mould towards the centre. During the solidification process, the atoms in the molten metal arrange themselves in an ordered, crystalline structure [55]. As more atoms join the crystal lattice, the solidification front advances further into the liquid metal. The rate of solidification depends on several factors, such as the cooling rate, the shape and size of the casting, casting material, and different pouring parameters.

During the solidification process, the temperature of the molten metal begins to decrease, and the liquid metal starts to transform into a solid state. This transformation occurs through a series of stages, the first of which is the nucleation stage. During the nucleation stage, the first solid particles begin to form as the temperature of the molten metal decreases. These solid particles, called nuclei, serve as the starting point for the growth of the solid phase. The formation of nuclei is influenced by several factors, including the composition of the metal, the cooling rate, and the presence of impurities. The process of nucleation can be further classified into two types: heterogeneous and homogeneous nucleation [56]. In heterogeneous nucleation, the formation of solid particles is initiated at the surface of impurities or foreign particles present in the molten metal. In contrast, homogeneous nucleation occurs when the formation of solid particles is initiated in the bulk of the molten metal.

After the formation of nuclei, the growth stage follows, during which the solid particles begin to grow. The growth of the solid phase occurs by the addition of atoms or molecules from the liquid phase onto the surface of the solid particles. The rate of growth is influenced by several factors, including the temperature difference between the solid and liquid phases, the concentration of solute atoms in the liquid phase, and the crystallographic orientation of the solid particles. The final stage of the solidification process is the solid-state transformation stage. During this stage, the solid phase undergoes changes in its microstructure, such as grain

growth, dendrite coarsening, and phase transformations [57]. The changes in microstructure during solid-state transformation can significantly affect the final properties of the casting, such as mechanical strength, corrosion resistance, and ductility.

During casting, the solidification process typically starts at the walls of the mould, where the heat is rapidly transferred from the molten metal to the colder mould material. The solidification then progresses towards the centre of the casting, as the heat is gradually transferred from the outer surface towards the inner regions. Therefore, the point at which the solidification process starts depends on various factors such as the temperature of the metal, the thermal properties of the mould material, and the cooling rate of the metal [58].

As the molten metal cools and solidifies, the temperature of the mould also decreases. The mould design must also take into consideration the properties of the casting metal and the solidification process. The mould must be designed to withstand the thermal shock and stress caused by the solidification process. The solidification process generates heat, and the mould must be able to conduct this heat away efficiently to prevent overheating and thermal damage. Steel is a good choice as a mould for aluminium castings because of its excellent thermal conductivity and strength at high temperatures. When molten aluminium is poured into a steel mould, the steel rapidly absorbs the heat from the molten metal, causing it to solidify quickly and uniformly. This results in a more controlled and predictable solidification process, which can lead to higher quality castings with fewer defects. Additionally, steel moulds are durable and can withstand the repeated thermal cycling and mechanical stresses that occur during the casting process [59]. Steel moulds also have good dimensional stability, which means they can maintain their shape and size even under high temperatures and pressures, resulting in consistent casting dimensions. Steel typically has a higher thermal conductivity than many other materials, including aluminium. This means that steel has a higher rate of heat transfer, which can result in a higher cooling rate when used as a mould for aluminium castings. The use of moulds with higher cooling rates can accelerate the solidification process.

The temperature of the molten metal can also influence the solidification process [60]. If the temperature is too low, the solidification process may be incomplete or may result in the formation of defects such as shrinkage. On the other hand, if the temperature is too high, the solidification process may be too fast, which can also lead to the formation of defects. Therefore, in the case of molten aluminium being cast in a steel mould, the preheating of the mould to a temperature above the melting point of aluminium is essential to ensure that the molten aluminium does not solidify too quickly upon contact with the mould [61]. This allows for a more controlled solidification process, which can result in a higher quality casting with fewer defects. Defects are a common occurrence in the metal casting process and can significantly impact the quality and reliability of the final product. Fortunately, there are several techniques that can be employed to minimize defects and improve the quality of the casting.

Proper design of gating and risering is one such method. The gating system is responsible for controlling the molten metal's flow into the mould, while the riser system provides a reservoir of molten metal to compensate for any shrinkage during the solidification process [62]. Improper gating and risering can result in various casting defects, including porosity, shrinkage, and misruns. Proper gating and risering design are essential for achieving a high-quality casting with minimal defects [63]. The riser system is equally important and should be designed to provide a sufficient volume of molten metal to compensate for the shrinkage that occurs during solidification. Shrinkage can occur as the molten metal cools and solidifies, causing a decrease in volume. If the riser system is insufficient, the casting may have shrinkage defects or cracks. The pouring temperature of the molten metal is another important parameter that needs to be carefully controlled during the casting process [53]. Iqbal et al. [64] indicated that the pouring temperature can affect the solidification behaviour of the molten metal, and if not controlled properly, it can lead to the formation of porosity defects and hot spots. Porosity defects occur when air is trapped in the solidifying metal, resulting in voids filled with air in the casting. Brimacombe and Sorimachi [65] stated that hot spot is another type of defect that can occur due to improper cooling. Hot spots are regions in the casting where the cooling rate is slower,

causing the metal to solidify more slowly and resulting in a coarser microstructure. This can lead to reduced mechanical properties and casting failure. Therefore, proper control of the pouring temperature is critical for minimizing porosity defects and hot spots [66]. The pouring temperature should be optimized for the specific metal being cast and the mould type. Additionally, advancements in simulation software have allowed for more accurate predictions of casting defects, allowing for adjustments to be made before production.

1.2.4 Turbulence Model in Casting

Turbulence is a chaotic and complex flow pattern that occurs in fluids, when there is a high rate of flow or when the fluid encounters an obstacle or boundary. It is characterized by random fluctuations in velocity, pressure, and other flow parameters that lead to the formation of eddies and vortices [67]. Turbulence is a significant factor in many areas of fluid dynamics, including aircraft design, weather prediction, oceanography, and industrial processes. It affects the efficiency of fluid transport, mixing, and heat transfer, and can also cause structural damage in pipes and other components. The study of turbulence involves the development of mathematical models and experimental techniques to better understand and predict its behaviour. According to Rodi [68], turbulence models are employed to simulate the intricate flows in engineering applications and to describe the turbulent behaviour of the fluid.

Turbulence models are mathematical models that aim to predict the turbulent behaviour of a fluid flow by providing an approximation of the turbulent flow variables. These models are based on the Navier-Stokes equations, which describe the motion of fluids in terms of velocity, pressure, and viscosity [69]**.** However, since the Navier-Stokes equations cannot be solved analytically [70] for most practical engineering problems, turbulence models are used to provide a numerical solution. These models use a combination of empirical relations, statistical methods, and numerical simulations to represent the complex interactions between the fluid particles and the flow boundaries. Menter [71] stated that turbulence models have found wide applications in various engineering fields, including aerospace, automotive, and energy industries. They have

been applied to simulate flows around casting, aircraft wings, turbomachinery components, internal combustion engines, and heat exchangers, among others. The accuracy of turbulence models depends on the flow conditions and the complexity of the geometry. Therefore, choosing an appropriate turbulence model is crucial for obtaining reliable predictions of the flow behaviour [72].

Turbulence models can be classified into two broad categories: Reynolds-averaged Navier-Stokes models (RANS) and Large Eddy Simulation models (LES). RANS models are based on the Reynolds decomposition, which separates the flow variables into mean and fluctuating components. These models solve the time-averaged equations of motion and require additional closure models to represent the turbulent stresses and dissipation rates [73]. On the other hand, LES models simulate the large-scale turbulent structures explicitly, while the small-scale structures are modeled using subgrid-scale models. LES models require a fine computational grid resolution to capture the small-scale turbulent structures, which makes them computationally expensive compared to RANS models [74]. Detached Eddy Simulation (DES) is another hybrid turbulence model that combines RANS and LES methods. It uses RANS near the wall and LES in the outer flow regions to simulate the turbulent flow over a wide range of scales. DES is particularly useful for simulating flows with separated regions, such as those encountered in aerodynamic applications [75]. However, for most practical tasks, RANS models are widely used in industry due to their relatively low computational cost and ability to provide useful engineering insights into turbulent flows [76].

Lew et al. [77] reported k-epsilon models are one of the most widely used turbulence models in RANS simulations. These models use two transport equations to solve for the turbulent kinetic energy (k) and the turbulent kinetic energy dissipation rate (ε). The k equation is derived by assuming that the turbulent fluctuations of the velocity can be approximated as a Gaussian distribution, and that the turbulent kinetic energy is proportional to the velocity fluctuations squared [78]. The k equation includes terms for the production, transport, and dissipation of turbulent kinetic energy.

The ε equation is derived based on the assumption that the dissipation rate of turbulent kinetic energy is proportional to the product of the turbulent kinetic energy and a characteristic length scale, as reported by Alvarez et al. [79]**.**The ε equation includes terms for the dissipation of turbulent kinetic energy, as well as for the production of turbulence due to the mean velocity gradients. Ansys Fluent avails many such models like the standard k-ε model, RNG k-ε model, realizable k-ε model, etc. [80].

The standard k-epsilon model [81] is based on two transport equations: one for the turbulent kinetic energy (k) and the other for the dissipation rate of turbulence (epsilon). The kinetic energy equation describes the rate at which energy is transferred from the mean flow to the turbulence, while the dissipation rate equation describes the rate at which turbulent energy is converted into heat through molecular viscosity [82]. The standard k-epsilon model assumes that the turbulence in a flow field is isotropic and homogeneous, meaning that turbulence characteristics are independent of the direction and location in the flow field. It also assumes that the turbulent viscosity is proportional to the turbulence kinetic energy and the dissipation rate of turbulence. This assumption allows the model to simulate the mixing of momentum and energy in the turbulent flow, as stipulated by Schumann and Gerz [83].

The derivation of the standard k-ε model assumes that the flow is completely turbulent and that the influence of molecular viscosity is insignificant [78]**.** As a result, the standard k-ε model is applicable solely to fully turbulent flows. The standard k-epsilon model has been widely used in CFD simulations of turbulent flows because of its simplicity and computational efficiency. However, it has limitations in accurately predicting complex turbulent flows with strong shear, rotation, and curvature. To overcome these limitations, several modifications and enhancements to the standard k-epsilon model have been proposed, such as the RNG k-epsilon model [84] and the realizable k-epsilon model [85].

The Renormalization Group (RNG) k-epsilon model is an extension of the standard k-epsilon model that was developed to address some of these limitations. The RNG k-epsilon model was introduced by Yakhot and Orszag in 1986 [84], and it has since become a popular turbulence

model in CFD simulations. The RNG k-ε turbulence model is derived by applying a mathematical technique called renormalization group theory to the instantaneous Navier-Stokes equations. This makes a model with new terms and functions that make it different from the standard k-ε model. The RNG k-ε model is considered more accurate and reliable for a wider range of flow conditions compared to the standard k-ε model [86]. The RNG model is similar to the standard k-ε model but has some improvements: It includes an additional term in its equation that enhances accuracy for rapidly strained flows. According to Escue and Cui [87], the RNG (Re-Normalization Group) model incorporates the influence of swirl on turbulence, making it more accurate for swirling flows. The RNG theory gives an analytical formula for turbulence Prandtl numbers, whereas the standard k-ε model uses constant values specified by the user. While the standard k-ε model is suitable for high Reynolds number flows, the RNG theory incorporates a differential formula for effective viscosity that considers low Reynolds number effects.

The Realizable k-epsilon model is a variant of the standard k-epsilon model used in turbulence modelling. Shih et al. [85] proposed the RNG k-ε turbulence model as an improvement to enhance the accuracy of predictions for complex turbulent flow. The standard k-epsilon model assumes that the rate of turbulence dissipation is proportional to the square of the turbulent kinetic energy and a constant called the turbulent viscosity. However, this assumption is not always accurate, especially for flows with high strain rates or swirling motion. The Realizable k-epsilon model addresses this limitation by using a more complex equation for the turbulent viscosity that considers the flow geometry and the local turbulence intensity. The Realizable k-epsilon model also uses a more accurate equation for the turbulent dissipation rate. Both the RNG k-epsilon model and the realizable k-epsilon model are improvements over the standard k-epsilon model [88]. However, the RNG k-epsilon model is widely used in casting due to its higher accuracy, reliability, applicability to a wider range of Reynolds numbers, and computational efficiency [88, 89]. The RNG k-ε turbulence model has been used in this thesis.

1.2.5 Porosity Defects

To simulate the solidification of a casting, the main concerns are the volume concentration, and fluid velocity within the solidifying casting. However, this stage is often accompanied by various defects. Porosity is one of the most common types of defects that can occur during the solidification of a casting. It is characterized by the presence of voids or pores within the casting material, which can reduce its strength and cause other issues during operation. The mechanical properties of a cast metal matrix composite are significantly influenced by the volume fraction of porosity, as well as the size and distribution of pores within the material [90]**.** Rappaz [34]conducted a review of studies that incorporated micro models of solidification.

Porosity can occur for a variety of reasons, including air or gas entrapment, shrinkage, and other factors related to the casting process [91, 92]. Christian et al. [93] demonstrated that porosity formation in castings is primarily caused by the casting parameters. These parameters include the casting route used, the speed and position of the impeller used for stirring, the volume fraction of reinforcement material, and the holding time during the process.

Porosity can occur in both metal [94] and non-metal [95] casting processes. In metal casting, porosity is typically caused by the entrapment of air within the molten metal as it solidifies [96] or due to shrinkage during solidification [97]. Researcher [98] have argued that small changes in the quality or composition of a metal can lead to the formation of casting defects, even when standard process conditions are followed.

The presence of porosity in a casting can have a significant impact on its mechanical properties [99]. Porosity defect can cause the casting to be weak and brittle, leading to cracking, fracture, or failure under stress. The presence of voids can also create stress concentrations, reducing the load-bearing capacity of the casting. Additionally, porosity can negatively affect the fatigue life of the casting, reducing its ability to withstand repeated loading cycles [100]. Porosity can also compromise the corrosion resistance of the casting, leading to accelerated corrosion and rust formation. Apart from mechanical properties, porosity defects can also affect the surface finish

and overall appearance of the casting. Voids can create irregularities on the surface of the casting, making it difficult to achieve the desired finish. Porosity can also lead to discoloration or staining of the casting, making it unsuitable for aesthetic or decorative applications.

Porosity leads to an increase in surface roughness, resulting in elevated wear and friction on the surface and a decrease in material strength [101]. Researchers [101] observed that the frictional and wear behaviour of pure aluminium is influenced by the pouring temperature and pouring velocity. Specifically, an increase in the temperature of pouring leads to an increase in frictional and wear behaviour, while an increase in pouring velocity results in a reduction in frictional and wear behaviour.

Some of the most common types of porosity defects are gas or air porosity and shrinkage. Samuel et al. [102] conducted several experiments using Al-Si Cast Alloys and revealed that pore size has a greater impact than the presence of numerous small pores from a mechanical perspective. Porosity located at the centre of the testing bar influences tensile testing, whereas edge porosity causes crack initiation during fatigue testing. Ridgeway et al. [103] developed a new model, called the Oxide Entrainment Number, to predict the location-specific volumes of entrained and oxide-induced defects in aluminium castings. This model can accurately determine the number of gaseous pores in a selected position in the casting.

Since the porosity is an inevitable but preventable issue persistent with the casting process, researchers have also explored the various ways to reduce it. They have established that with proper care and attention, it is possible to reduce porosity defects and improve the quality of the castings [104].

Hodbe and Shinde [105] suggested that proper mould design is one of the key steps in minimizing porosity defects. The mould should be designed with adequate venting (riser) to allow gases to escape from the mould cavity The gating system should also be designed to promote even filling of the mould [106]. In addition, the use of high-quality refractory materials can help to reduce gas permeability and improve the surface finish of the casting, as reported by

Hardy et al. [107]. Another important factor to consider is metal chemistry. According to Sola and Nouri [108], the composition of the metal plays a crucial role in the formation of porosity defects. In particular, the presence of dissolved gases such as hydrogen and oxygen can lead to the formation of gas pores in the casting [109]. To reduce the risk of porosity defects, it is important to carefully control the metal chemistry, using degassing agents if necessary, and minimizing exposure to air and moisture during the melting and pouring process [110].

The casting process parameters play a critical role in reducing porosity defects. For example, the pouring temperature and filling rate should be carefully controlled to ensure that the metal flows smoothly into the mould cavity [94]. The use of vacuum or pressure casting techniques can also help to reduce the formation of porosity defects by removing trapped air and gases from the mould cavity [111]. Pilani [112] claimed that Post-casting treatments can also help to reduce porosity defects. Heat treatment, for example, can be used to refine the microstructure of the casting and reduce the size and number of gas pores. Although, reducing porosity defects is an important goal in casting, it is also important to understand the major types of porosity defects that can occur in castings.

When the molten metal begins to solidify, it will naturally shrink as it cools. If this shrinkage is not compensated for, it can create voids or pores within the casting [97]. Shrinkage can be caused by a variety of factors, including the design of the casting itself, the temperature of the mould material, and the rate at which the metal cools. The simulation of casting was first focused on predicting solidification shrinkage as it was thought to be the most common issue in casting. Nowadays, primary shrinkage is well comprehended and is possibly one of the most precisely forecasted defects by considering the local temperature and cooling rate conditions. The Niyama criterion is an example of such a function and is employed for alloys with a short freezing range particularly steels. Taylor et al. [113] has conducted a review of several Niyama criteria functions.

Porosity resulting from solidification shrinkage is a problematic defect that affects the performance of all kinds of metal castings by reducing their strength, fatigue, and creep

properties. Accurately predicting porosity in the casting process simulation can help minimize or even eliminate this defect**.** Esser et al. [114] presented a new model for predicting porosity based on recent research that has shown all shrinkage porosity grows in regions of a casting with the lowest solid fraction. The model accounts for the liquid density variation during cooling and solidification and calculates feeding flows and pressure distribution in the liquid. It predicts the location, extent, and amount of all types of shrinkage porosity in a casting. Li et al. [115] predicted the size of shrinkage porosities in an aluminium suspension part using quantitate simulations.

Porosity during commonly caused by a mixture of shrinkage and trapped air, and various models have been suggested for the prediction of the porosity [116, 117]. When the metal begins to solidify, gases can become trapped in the solidifying material, creating voids or pores. The type and amount of gases that are present in the molten metal will depend on a variety of factors, including the type of metal being used, the temperature of the metal, and the presence of other materials or impurities in the molten metal [118]. Li et al. [119] extended their research to propose a simulation method for quantitatively predicting shrinkage porosity during molten metal replenishment in squeeze casting process.

Gu and Luo [120] proposed a model that considers both shrinkage pressure and initial hydrogen content to predict porosity evolution and the final percentage of porosity, which is then linked to microstructure location in cast aluminium. Additionally, a multiphase-field model was created to simulate the progression of the hydrogen pore and solid phase during the solidification of a binary Al-Cu alloy [121]. The present thesis deals with permanent mould casting. In such a process, molten metal is poured into a mould made of a reusable metal (typically steel). The presence of air in the mould can lead to voids or holes in the final casting, reducing its quality and strength. To prevent air porosity, the mould is often designed with vents or risers that allow air to escape from the mould cavity as the molten metal fills it [122]. Additionally, the pouring process must be carefully controlled to prevent air from being drawn into the mould.

Homayonifar et al. [111] utilized a solution algorithm volume of fluid (SOLA-VOF) algorithm-based 3D single-phase code to simulate mould filling. They employed a concentration transport equation-based computational model to compute the distribution of air porosity, and created a mixed VOF-Lagrange algorithm to model splashing in high-pressure die casting (HPDC). Researcher [123] have classified the types of air porosity into multiple categories which include air-entrapment, lubricant and/or die release agent entrapment porosity, hydrogen porosity, vapour entrapment porosity, and superficial gas-related defects are commonly known as blisters and pinholes.

Focusing on the gravity die casting, this type of permanent mould casting offers inferior surface finishing compared to high pressure die casting and does not support the production of intricate geometries, which can be readily achieved through pressure die casting. Gravity die casting generally has a higher tendency for air porosity compared to high pressure die casting due to the slower rate of metal flow and lower pressure involved in the process. Researcher [124] established that during gravity castings of aluminium alloys, 45% of the defects are caused due to air porosity. It was seen that the detection of shrinkage and oxide layers occurs due to surface turbulence during the mould filling process [125].

Numerous studies and experiments have been undertaken to study air porosity. According to research conducted by Nanda et al [126], specimens taken closer to the ingate exhibited higher tensile strength and yield strength, and lower porosity percentage. In another study [127], simulation was used to identify porosity zones at risk in both gravity and high-pressure die castings. Thanabumrungkul et al. [128] observed that casting parts achieved complete filling at low solid fractions. Dispinar et al. [129] concluded that metal quality has a greater impact on mechanical properties than porosity content. Additionally, Anderson et al. [130] found that air gaps are likely to form between the casting and die, which significantly affects heat removal.

Air porosity is detrimental to the quality of casting and can lead to increased production costs. Fortunately, there are several methods available to reduce the formation of air porosity in gravity die casting. Firstly, proper gating and riser design can help reduce the amount of air that enters

the molten metal during casting [131]. Gating and riser design should aim to minimize turbulence and promote a smooth flow of metal, which can help reduce the amount of entrapped air. The use of tapered gating and risers can also help to reduce air entrainment. Secondly, controlling the temperature reduce air porosity [132]. This can be achieved through proper furnace and ladle design, as well as the use of insulating materials to minimize heat loss during casting [110]. Thirdly, the use of effective degassing agents can help to reduce the amount of dissolved gas in the molten metal [133]. This can help prevent the formation of gas porosity during casting. Common degassing agents include nitrogen, argon, and chlorine, which are added to the molten metal before casting to promote the removal of dissolved gas. Finally, proper mould design and maintenance can also help reduce air porosity in gravity die casting. The mould should be designed to promote a smooth flow of metal and minimize turbulence, which can help reduce air entrapment [125]. Regular maintenance and cleaning of the mould can also help prevent the accumulation of debris or other contaminants, which can lead to the formation of air pockets during casting.

1.2.6 Hot Spot

Apart from porosity defects, there may be presence of hotspots too. Hotspots are localized regions in the casting where the temperature is significantly higher than the surrounding areas. These hotspots can cause defects such as shrinkage, air porosity, and other types of porosity [134]. The formation of hotspots is due to various factors, including the design of the casting, the metal flow rate, the temperature of the molten metal, and the cooling rate of the casting.

One of the main causes of hotspots in gravity die casting is the design of the casting. The design of the casting can affect the flow of the molten metal and the cooling of the casting. The design should be optimized to ensure that the molten metal flows evenly throughout the mould and that the cooling rate of the casting is uniform. Kurtulus et al. [135] stated that the occurrence of moulding defects such as hot spots and distortions in products can be attributed to non-conformal cooling during the casting process. Their study explored the impact of cooling channels on the casting process and the final properties of products produced using standard and

conformal cooling gravity die casting moulds. It has been established [136] that feeding design is also an important aspect of gravity die casting as it directly affects the formation of hot spots. Grill et al. [137] discovered that hot spots can form on the slab's surface within a few centimetres of the corners.

A method for identifying hot spots in complex sections was discussed by Ravi and Srinivasan [138]. The study found that the results obtained from the method were in close agreement with those obtained from actual experimentation and the finite-element method. The time gradient method for calculating feed paths and hot spots was discussed in the research [139]. In the study conducted by Warriner and Monroe [140], the effects of modifying geometric parameters on the position of hot spots were investigated in idealized two-dimensional sections. The study also used a watershed image segmentation technique to analyse a three-dimensional solid model. Chakravarti and Sen [134] conducted a simulation study using Ansys to analyse the initiation of hot spots by varying pouring parameters, such as pouring velocity and pouring temperature. Their study enabled the prediction of hot spot positions and approximate sizes under different pouring conditions. It was observed that hot spots are typically located below the riser. Li and Cui [141] proposed a new method for quickly locating isolated hot spots in the numerical simulation of the solidification process of castings. The predicted results were compared with the measured ones, and good agreement was obtained. An improved geometric model for hot spot prediction was proposed by Xu et al. [142], based on the idea that the heat dissipation capacity of a location in a casting depends on its distance to the heat transfer surface. This model is faster and more convenient than other procedures based on heat transfer equations.

1.2.7 Thermal Analysis of Casting

Thermal analysis is an essential part of casting design and production, enabling manufacturers to understand and optimize the solidification process, which is critical to the final properties of the casting. Thermal analysis involves predicting and monitoring the temperature changes that occur during the casting process, providing valuable information about the solidification behaviour, shrinkage, and potential defects [143].

One of the most widely used techniques for thermal analysis is thermocouple measurements. This method involves inserting a thermocouple into the mould or the casting, allowing for the real-time monitoring of temperature changes during the casting process [144]. This information can then be used to calculate the cooling rate, which is a critical factor in determining the microstructure and properties of the casting. Thermocouple measurements can also be used to detect the onset of solidification and to monitor the cooling curve to identify potential defects such as porosity.

Another popular method for thermal analysis is computer simulation. Computational fluid dynamics (CFD) is used to simulate the thermal behaviour of the casting process [32, 33]. CFD models can predict temperature distributions, solidification rates, and the formation of defects such as hot spots, porosity, and cracks. Advanced simulations using complex algorithms and machine learning techniques can also be used to optimize the casting process and design.

In recent years, infrared thermography has gained popularity in thermal analysis. This technique uses infrared cameras to capture the surface temperature of the casting, providing a non-invasive method of monitoring the solidification process [145]. Infrared thermography is useful in detecting the formation of hot spots and the onset of solidification, which can aid in optimizing the casting process to minimize defects.

Thermal analysis has revolutionized the casting industry, enabling manufacturers to predict and optimize the solidification process, leading to improvements in casting quality and production efficiency. However, challenges still exist, such as accurately predicting the onset of solidification and detecting potential defects in complex geometries. Nonetheless, advances in technology and simulation methods are continuously improving the accuracy and capabilities of thermal analysis in casting [104, 144].

Simulation of casting is better because it provides several advantages compared to traditional methods [146]. One of the primary benefits is that it allows for the optimization of the casting process by predicting the behaviour of molten metal during solidification. Simulation software

can model the entire casting process, from mould filling to solidification and cooling, and can provide insights into potential defects and how to avoid them. This allows for a more efficient and cost-effective casting process, as it minimizes the need for physical trial-and-error testing.

The use of casting modelling software is rapidly increasing in the metal casting industry to simulate the casting process in a virtual field, providing insight into the mould filling, cooling and solidification, and defects in casting. Rajkumar and Rajini [147] presented a literature review discussing modelling and simulation techniques for metal casting processes with reference to several relevant case studies. The review includes a discussion of the most popular casting simulation programs and the mathematical models used, as well as recent attempts to incorporate casting simulations into mechanical simulations to predict the service life of cast products. The review concluded that casting simulations are vital in the production of high-quality cast products without defects, and further advancements in simulation techniques are needed to accurately assess the durability of castings. Li et al. [148] utilized ANSYS to analyse both the temperature distribution and stress distribution of a heat-exchange pipe. By examining these distributions, the researchers aimed to determine the most reasonable and cost-effective measures for the heat-exchange pipe. The analysis results provided a foundation for the design and optimization of the heat-exchange pipe, and could be used to inform future improvements to the pipe's performance. Overall, the study's use of ANSYS to model the heat-exchange pipe's behaviour represented a valuable contribution to the field of thermal engineering, and could help to improve the efficiency and effectiveness of heat-exchange systems in a range of industrial applications. The use of ANSYS for casting has been a topic of interest in recent research.

Soni et al. [149] presented the design and analysis of a piston for a specific engine. The design and modelling of the piston were carried out using Fusion 360, while the analysis was performed using ANSYS software. The design file from Fusion 360 was imported into the ANSYS software, and the results were discussed. Since the piston of an internal combustion engine is subject to thermal and thrust loads, an Aluminium alloy was chosen as the material for

analysis. The ANSYS software was used to perform both structural and thermal analysis, eliminating the complexities of thermal load variations and analysing critical values.

In their study, Nişanci and Yurddaş [150] compared the results of casting simulation with experimental production to determine whether they are consistent. The study found that the interface heat transfer coefficient of the casting-mould showed good agreement between the simulation results and experimental findings. However, the calculated coefficient from the simulation was found to be higher than the measured value from the experiment. The study concludes that accurately estimating the interface heat transfer coefficient is crucial for successful production of high-quality castings, and using a higher value of this coefficient in simulations can improve the prediction of casting defects.

1.3 Objectives

Due to the complexity of the casting process, some researchers have assumed that solidification begins only after the complete filling of the mould cavity. Some researchers assumed that the mould cavity is already filled with molten metal at the beginning of the simulation and neglected to analyse the casting process during the time when the cavity is filled with liquid metal. The research gap identified in this thesis is the lack of practical ideas into the starting time of solidification in the casting process. Further research is needed to address this gap and provide a more accurate understanding of the solidification process in aluminium casting**.** There is also a lack of well-documented research on porosity measurement in metal mould aluminium casting. Furthermore, there is a need for comprehensive studies that consider the combined impact of various parameters, such as pouring temperature, pouring velocity, and mould initial temperature, on porosity formation in aluminium casting. Additionally, there is insufficient information and data available regarding the solidification time and the length of solidified metal for different casting parameters. Lastly, further research is required to optimize casting parameters in order to minimize porosity defects in aluminium casting and improve the overall quality of casting products.

The objective of this thesis is to develop a computational model for solidification of aluminium casting using Ansys Fluent. This includes studying the filling, solidification of casting and analysing the characteristics of the solidification front using two-phase system (air and aluminium) and a mixture of liquid and solid phases of aluminium. The aim is to enhance casting quality by optimizing casting parameters, minimizing porosity, and predicting porosity location and areas with high porosity. The analysis provides insights into the variation of solid aluminium filling and solidification time under different casting parameters.

The objectives can be briefly summarised as,

- Develop a computational model for the solidification of aluminium casting and study the filling and solidification processes in casting. That has been discussed in chapter 2.
- Analyse the characteristics of the solidification front and solidification time in aluminium casting using one dimensional model. That has been discussed in chapter 2.
- Create a three dimensional computational model with Ansys Fluent to understand how casting solidifies, and explore the processes of filling and solidification in casting. That has been discussed in chapter 3.
- Analyse the characteristics of the solidification front in a two-phase system (air and aluminium) and a mixture of liquid and solid aluminium phases. That has been discussed in chapter 3.
- Enhance casting quality by optimizing casting parameters. Minimize porosity in the castings. Predict porosity locations and areas with high porosity. That has been discussed in chapter 3.
- Provide insights into the variation of solid aluminium filling and solidification time under different casting parameters. That has been discussed in chapter 3.

1.4 Scope of the Study

This thesis involves the permanent mould casting of pure aluminium (99.9% pure aluminium) with a mould made of steel (1.5% carbon steel). Two simple phase change models have been developed to estimate the solidification time and solidification front. The first model allows for the variation of pouring temperature, while the second model, an improvement on the first, allows for the variation of both pouring temperature and mould temperature. A computational fluid dynamics (CFD) model has then been created, which includes a two-phase system consisting of air and aluminium in the mould cavity. The flow in the mould cavity is found to be turbulent based on the pouring velocity. The pouring temperature, pouring velocity, and mould temperature are varied in this CFD model. The model is used to determine the air porosity, solidification time, solidification front, and length of aluminium metal solidified from the base of the mould cavity with varying casting parameters. In addition, the riser design has been performed as part of this thesis. The solidification behaviour has also been determined to characterize the hotspot in the casting.

1.5 Organization of the Thesis

The thesis is divided into four chapters, each focusing on different aspects of casting. The chapters are structured to provide a comprehensive understanding of the casting process, solidification, porosity formation, and optimization techniques.

Chapter 1 introduces metal casting, emphasizing the importance of permanent mould casting and its advantages. The significance of aluminium casting in permanent moulds is highlighted. The chapter also discusses the solidification process in metal casting and addresses the issue of porosity defects. Additionally, the use of simulation software like Ansys Fluent is introduced. The chapter concludes by outlining the objectives and scope of the study, identifying research gaps, and setting the stage for the subsequent chapters.

Chapter 2 provides an overview of one-dimensional casting solidification models. Two models are presented, allowing for variations in mould temperature and pouring temperature. The first

model utilizes an error function method to calculate the solidification front and time. The second model incorporates an error function and complementary error function to simulate the solidification process and calculate solidification times for different pouring temperatures and mould initial temperatures. However, these models do not consider pouring velocity or porosity calculation, which are addressed in later chapter.

Chapter 3 introduces a comprehensive three-dimensional simulation model developed using Ansys Fluent. The model captures the complexities of the casting solidification process, including the two-phase system of air and aluminium, turbulent flow, and natural convection effects. It allows for variations in pouring velocity, pouring temperature, and mould initial temperature. The model provides insights into porosity formation and offers a comprehensive analysis of the solidification process.

Chapter 4 concludes the study and discusses its overall contribution. The key findings and achievements in developing computational fluid dynamics (CFD) models for permanent mould casting of aluminium are summarized. The chapter acknowledges the limitations and challenges encountered during the research and identifies areas for further investigation. The importance of ongoing research to improve casting techniques, optimize parameters, and enhance production processes in the field of aluminium casting is emphasized.

CHAPTER 2: ONE DIMENSIONAL SOLIDIFICATION MODEL OF CASTING

2.1 Introduction

When molten material is poured into a mould, it starts to cool down and reaches a temperature below its freezing point, at which the material solidifies and changes its state from liquid to solid. Solidification time is the time required for a material to change its state from liquid to solid. The solidification time is an essential parameter in the casting industry, and it affects the production rate [151]. By knowing the solidification time, the industry can estimate the production rate per day and plan the production process accordingly. Based on solidification time, the industry can estimate the time required to produce each casting and determine the total number of castings that can be produced in a day.

This chapter focuses on the solidification process in casting using a one-dimensional casting solidification model. Specifically, a one-dimensional casting model is used in thin sections castings such as long thin metal plate. In the case of a long thin plate, the heat transfer occurs primarily in the long axis direction, and the others dimension are much smaller than the length of the plate. This means that the solidification process can be approximated as one-dimensional. When thin sections are required for casting, the one-dimensional model can be employed to simulate the process because they are relatively simple and computationally efficient [152] and can be useful for the optimization of casting parameters [153].

In this chapter, two one-dimensional casting solidification models have been simulated. In the first one-dimensional solidification model, only mould temperature can be varied. The pouring temperature cannot vary because pouring temperature of the material is fixed as the freezing temperature of the material. An error function has been used to simulate the model. The error function method is a useful and widely used mathematical model in the field of casting simulation [154]. In the second model, the mould temperature and pouring temperature both can

be vary. An error function and complementary error function have been used to simulate the model. As the molten metal cools and solidifies, the solidification front moves from the mould wall towards the centreline of the casing. Both models can calculate the position of the solidification front and the solidification time. However, the calculation of error function is complex and time-consuming. The error function, complementary error function and all the calculations are performed accurately using FORTRAN 95 programming software.

2.2 First Solidification Model

In this thesis aluminium metal casting of 60 mm length, 60 mm breadth, and 10 mm thickness has been done by steel mould. In the first one-dimensional model, the mathematical formulation using error function has been presented and a programming model has been developed using FORTRAN 95 software to calculate the solidification time and solidification front. Then this programming model is applied to the previously performed casting to validate this programming model. It is seen that a same one-dimensional analysis was studied by reference [155]. In that [155], they examined the solidification time of iron casting in a copper mould with a casting length of 100 mm. The present model used the same material of casting, mould, and casting length for only validation purposes of the model. They calculated the solidification time only. After validation of solidification time, the solidification front has been studied by this model. Therefore, in this section iron casing in a copper mould with a casting length of 100 mm is employed to study solidification time and solidification front. It will help to understand the behaviour of solidification front with time of metal casting.

2.2.1 Mathematical Modelling

Figure 2.1 shows a schematic representation of the model. The mould-casting model is one-dimensional (1-D), with the dimension perpendicular to the mould-casting face.

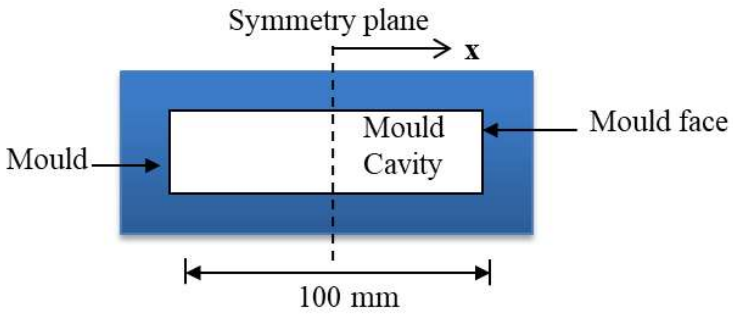

Figure 2.1: Schematic diagram of the model.

The heat flow in the other direction is ignored. Other assumptions in the model are that (a) the casting has been made semi-infinite; (b) The properties of metal and mould material are uniform and constant over a temperature range; (c) The freezing temperature of the molten material is also used as the pouring temperature; (c) Initially the mould is completely filled up with molten material at its freezing temperature; and (d) the temperature at the metal-mould interface remains constant from the beginning to the end of solidification.

The mould is initially at a temperature T_0. At time t=0, the liquid metal is poured at temperature T_p into the mould cavity. The temperature of interface between mould and metal is assumed to remain constant throughout the solidification process at its initial value of T_0. The freezing temperature of the material is T_f, which is also considered as the pouring temperature. The temperature distribution at any moment is shown in figure 2.2.

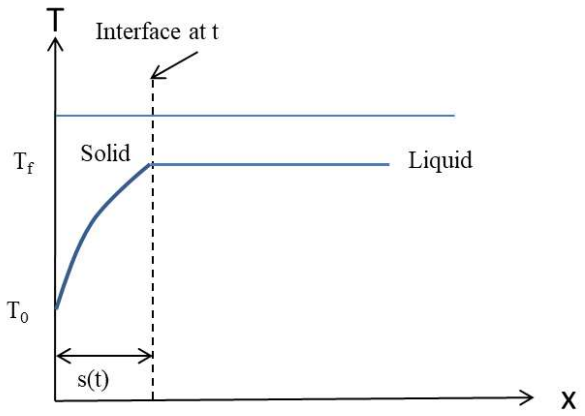

Figure 2.2: Temperature distribution in the casting.

s(t) indicates the depth of solidification at any moment in time t. The distribution of temperatures within the range 0<x< s(t) is given by [156],

$$\frac{T - T_0}{T_\infty - T_0} = \text{erf}\left(\frac{x}{2\sqrt{\propto_c t}}\right) \tag{2.1}$$

Where α_c is the thermal diffusivity of the casting, T_∞ is a constant of integration; T_0 is the mould-casting interface temperature; and $\text{erf}\left(\frac{x}{2\sqrt{\propto_c t}}\right)$ is called error function. The physical significance of the error function is to describe how heat spreads or diffuses over time in a material. It quantifies how temperature at a specific location changes as time progresses

The error function erf(ζ) is given by [156],

$$\text{erf}(\zeta) = \frac{2}{\sqrt{\pi}}\left(\zeta - \frac{\zeta^3}{3.1!} + \frac{\zeta^5}{5.2!} - \frac{\zeta^7}{7.3!} + \cdots\right)$$

Up to (n+1) terms the error function is represented by

$$\text{erf}(\zeta) = \frac{2}{\sqrt{\pi}}\zeta + \sum_{n=1}^{n} \frac{2}{\sqrt{\pi}}(-1)^n \frac{\zeta^{(2n+1)}}{(2n+1)n!} \tag{2.2}$$

At $x = s(t)$, $T = T_f$, where T_f is the freezing temperature of the casting material.

Applying this condition, equation (2.1) becomes

$$\text{erf}\left(\frac{x}{2\sqrt{\propto_c t}}\right) = \frac{T_f - T_0}{T_\infty - T_0} = \text{Constant} \tag{2.3}$$

Let, $\zeta = \left(\frac{x}{2\sqrt{\propto_c t}}\right)$ (2.4)

We get,

$$s(t) = 2\zeta\sqrt{\propto_c t}. \tag{2.5}$$

The energy balance equation at the solid-liquid interface [at $x = s(t)$] is,

$$\lambda_c \frac{\partial T}{\partial x}\Big|_{x=s(t)} = \rho_c L \frac{ds(t)}{dt} \tag{2.6}$$

Where λ_c, ρ_c, and L are the conductivity, density and latent heat of solidification of the casting material respectively.

Using the relation of the error function $\frac{d}{dz} erf(z) = \frac{2}{\sqrt{\pi}} e^{-z^2}$

From equation (2.1),

$$\frac{\delta T}{\delta x} = (T_\infty - T_0) \frac{d}{dx}\left[erf\left(\frac{x}{2\sqrt{\propto_c t}}\right)\right]$$

$$= (T_\infty - T_0) \frac{1}{\sqrt{\pi \propto_c t}} exp\left[-\left(\frac{x}{2\sqrt{\propto_c t}}\right)^2\right] \tag{2.7}$$

Substituting equation (2.7) into equation (2.6),

$$\frac{\lambda_c}{\sqrt{\alpha_c}} \frac{1}{\sqrt{\pi t}} (T_\infty - T_0) exp\left[-\left(\frac{s(t)}{2\sqrt{\propto_c t}}\right)^2\right] = \rho_c L \frac{ds(t)}{dt} \tag{2.8}$$

Substituting (T_∞ - T_0), ζ, and s(t) from equations (2.3), (2.4), and (2.5) into equation (2.8),

$$\frac{\lambda_c}{\sqrt{\propto_c}} \frac{1}{\sqrt{\pi t}} \frac{(T_f - T_0)}{\text{erf}(\zeta)} e^{-\zeta^2} = \rho_c L \zeta \frac{\sqrt{\propto_c}}{\sqrt{t}}$$

$$\zeta e^{\zeta^2} \text{erf}(\zeta) = \frac{k_c}{\sqrt{\alpha_c}} \frac{1}{\sqrt{\pi t}} (T_f - T_0) \frac{1}{\rho_c L} \frac{\sqrt{t}}{\sqrt{\propto_c}} \tag{2.9}$$

Putting $\alpha_c = \lambda_c / \rho_c c_c$ into equation (2.9),

$$\zeta e^{\zeta^2} \text{erf}(\zeta) = \frac{(T_f - T_0)}{\sqrt{\pi}} \frac{c_c}{L} \tag{2.10}$$

The value of ζ from equation (2.10) can be solved by trial and error.

The solidification time (t_s) can be determined by applying the following condition.

At $t = t_{s,} x = \ell/2$

Where ℓ is the length of the casting.

From Eq. (2.4),

$$t_s = \frac{\ell^2}{16\zeta^2 \propto_c} \tag{2.11}$$

The temperature profile inside the casting at a time t is given in [2.12].

$$T(t) = T_0 + (T_f - T_0)\left[1 - \text{erf}\left(\frac{x}{2\sqrt{\propto_c t}}\right)\right] \tag{2.12}$$

2.2.2 Validation

The numerical equations have been solved using FORTRAN 95 software. The solidification time was determined to be 42.1 s from the present model. The aforementioned procedure has been studied by Ghosh and Mallik [155]. The solidification time determined by them [155] is 42.1 s. The calculated value of the solidification time, 42.1 s, is in excellent agreement with the result of previous study [155]. This finding is consistent with the result obtained in another study as well [156].

Table 2.1: Thermophysical properties of iron and copper.

Properties	**Iron**	**Copper**
Specific heat (KJ/Kg-K)	670	0.376
Density (Kg/m^3)	7850	8960
Thermal conductivity (W/m-K)	83	398
Freezing temperature (^{0}C)	1540	1085

2.2.3 Solution Methodology

The simulation begins by setting the mould initial temperature to 30^0C. The temperature at the metal-mould interface is taken as the mould initial temperature. The thickness of casting has been taken as 100 mm. The thermophysical properties of iron are represented in table 2.1 [155, 156]. The calculation was performed by selecting any small random value of ζ. The value of ζ has been entered into equation (2.2). The corresponding value of erf (ζ) is observed for this specific chosen value of ζ. In equation (2.10), take the left hand side as LHS and the right hand side as RHS. If the difference between the value of LHS and RHS is insignificant (ε), then that specific value of ζ is allowable.

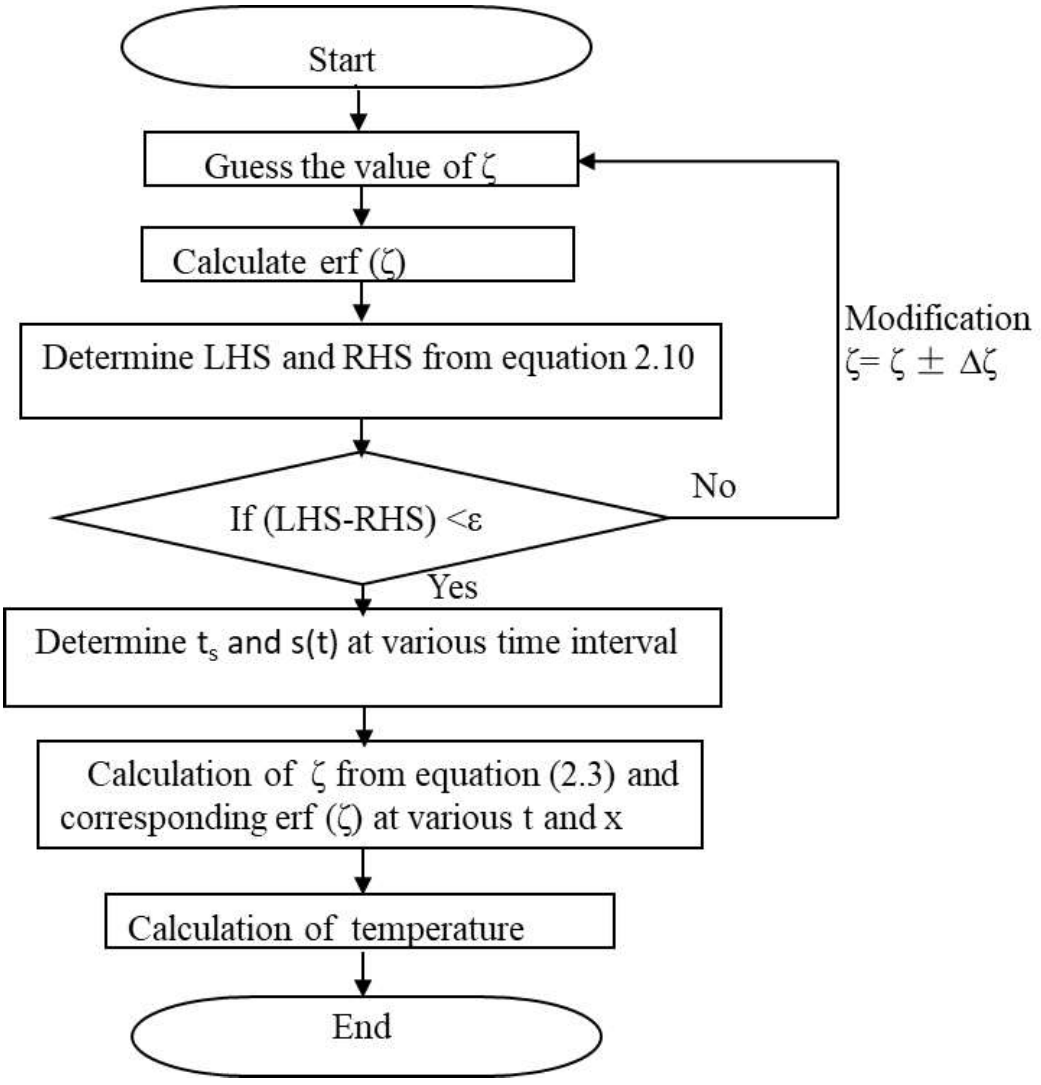

Figure 2.3: Flow chart of the calculation.

The total solidification time of casting at each time interval is computed by using the equation 2.11. Subsequently, the length of the solidified metal has been determined for a specific time interval. Equation 2.5 is used to calculate the length of metal solidified at a time. The temperature distribution has been determined at various time points. This required calculating the value of ζ (as per equation 2.4) at a specific time, which has been obtained using the length of metal that has solidified at that moment. The length of the solidified metal has already been determined for specific time intervals through equation 2.5. This value of ζ is used to determine the temperature distribution (equation 2.12) of the metal's solidified portion. Figure 2.3 shows the flowchart for the total process. All the calculations are performed in FORTRAN 95 programming language.

2.2.4 Results and Discussion

2.2.4.1 Solidification Time

Based on the calculations, the value of ζ was found to be 0.98, and it was determined that the solidification time is 42.1 s.

2.2.4.2 Solidification Front

The solidification front is the boundary or interface that separates the molten (liquid) metal from the solidified (solid) metal during the process of solidification. To investigate the effect on the solidification profile, simulations with varying time have been performed. The temperature distribution within the casting at different time has been calculated to discuss the solidification front. The temperature distribution within the casting has been determined using the above method and is depicted graphically in figure 2.4. Consider a point 10 mm from the face of the mould-casting. After 10 s, 20 s, 30 s, and 42.1 s the temperature of the point is 673°C, 495.9°C, 413.4°C, and 355°C respectively. Consider a point 20 mm from the face of the mould-casting. The temperature of the point after 10 s, 20 s, 30 s, and 42.1 s is 1146.8°C, 896.1°C, 760.4°C, and 658.4°C, respectively. According to the temperature distribution (figure2.4), a big

temperature drop happens initially because of the high heat content at initially. The temperature drop is observed to decrease with increasing time.

The solidification front (length of casting metal solidified) from mould-metal interface has been calculated. Figure 2.5 shows the length of casting metal solidified at various time intervals after pouring. The lengths of casting metal solidified from the mould-metal interface after 0 s, 5 s, 10 s, 15 s, 20 s, 25 s, 30 s, 35 s, 40 s and 42.1 s are 0 mm, 17.24 mm, 24.4 mm, 29.85 mm, 34.5 mm, 38.53 mm, 42.2 mm, 45.59 mm, 48.74 mm, and 50 mm. At 42.1 s, the entire casting material has solidified.

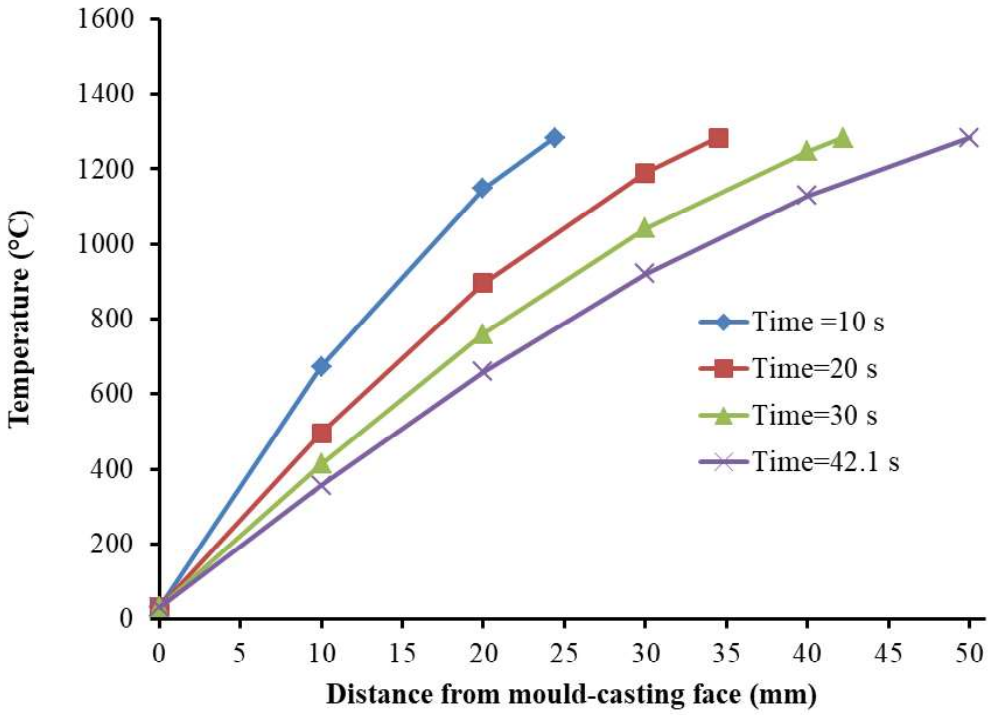

Figure 2.4: Temperature distribution in casting at different time intervals from pouring.

The length of solidified casting metal is 17.24 mm in the first 5 s, 7.16 mm in the next 5 s, and decreases as time progresses. A rapid solidification occurs first, followed by a relatively slow cooling because of the high heat content at initially. The solidification rate can be determined by dividing the length of solidified metal by the solidification time [156]. The solidification rate during the first 5 s of pouring is 3.448 mm/s, which decreases to 1.432 mm/s for the subsequent

5 s. Following that, the solidification rate further decreases to 1.09 mm/s for the next 5 s, and so on. The average casting solidification rate is defined as the ratio of total length of casting metal solidified to total casting solidification time [156]. The average solidification rate for this study is 1.49 mm/s.

The metal is in a molten state after exiting the solidified zone, and its temperature remains constant to pouring temperature, as displayed in figure 2.4. For instance, the length of solidified casting metal from the mould-metal interface after 10 s is 24.4 mm, and the temperature of molten metal after 24.4 mm to 50 mm is 1540°C (i.e. pouring temperature).

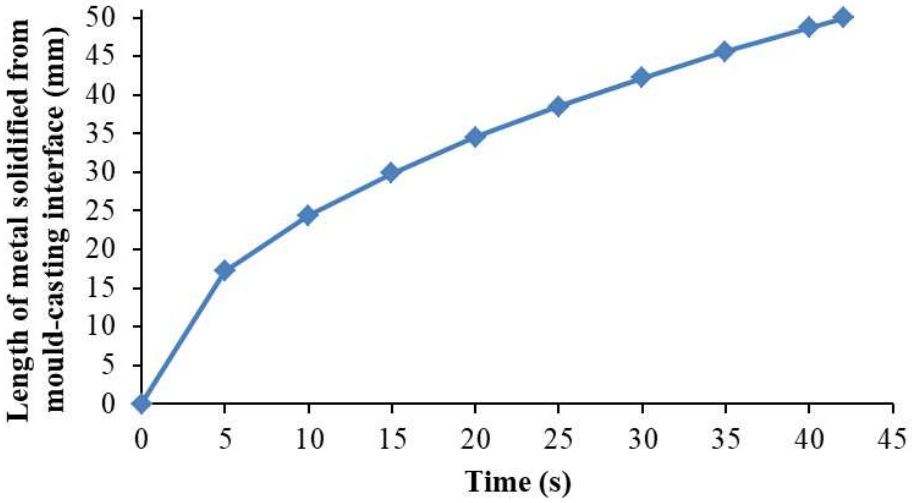

Figure 2.5: Length of metal solidified at different intervals of time.

As time passes, the solidification front moves through the mould cavity, indicating the amount of liquid that solidifies at a given time. When the casting cools, it forms two zones: the solid zone and the liquid zone, with an interface present between them. The temperature in the liquid zone remains constant throughout the liquid zone from interface.

2.3 Modified One Dimensional Solidification Model of Casting

The previous model provided valuable information regarding the solidification time and the location of the solidification front. It revealed that metal casting undergoes a rapid solidification phase initially, followed by a slower cooling process. Although the pouring temperature could not be varied in the previous model, in this new model, the pouring temperature can be varied to investigate its impact on the solidification process. In this section, the mathematical formulation using error function and complementary error function has been presented and a programming model has been developed using FORTRAN 95 software. In this thesis aluminium metal casting of 60 mm length, 60 mm breadth, and 10 mm thickness has been done by steel mould. Therefore, this model has been performed specifically for an aluminium casting with a steel mould for a length of 60 mm.

2.3.1 Mathematical Model

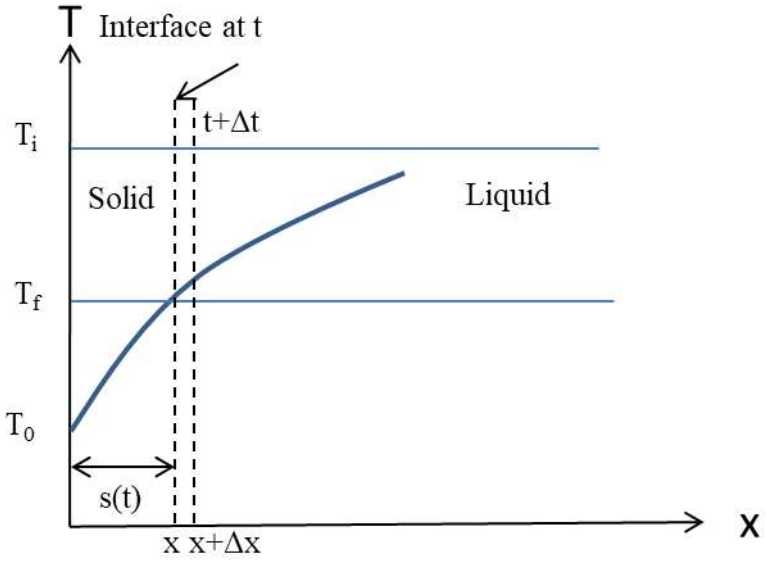

Figure 2.6: Temperature distribution using the modified one-dimensional model.

A liquid (molten aluminium metal) is confined to a half shell (x>0) at uniform temperature T_i which is higher than the freezing temperature T_f of the material as shown in figure 2.6. At t=0, the boundary surface temperature at x=0 is lowered to T_0 and maintained at that temperature for t>0. The boundary surface temperature at x=0 (T_0) is less than freezing temperature (T_f) of the

material. As a result, the solidification begins at x=0, and the interface moves in the positive *x*-direction with time. At time t, the solidified length is s(t) from *x*=0.

For the solid (s) phase,

$$\frac{\partial^2 T_s}{\partial x^2} = \frac{1}{\alpha_s}\frac{\partial T_s}{\partial t} \quad for\ t > 0 \tag{2.13}$$

$$T_s = T_0 \quad at\ x = 0\ \ for\ t > 0$$

For the liquid (l) phase,

$$\frac{\partial^2 T_l}{\partial x^2} = \frac{1}{\alpha_l}\frac{\partial T_l}{\partial t} \quad for\ t > 0 \tag{2.14}$$

$$T_l = T_i \quad at\ x = \infty\ \ for\ t > 0$$

At interface,

$$T_s = T_l = T_f$$

$$T_s = T_s(x, t)$$

$$T_l = T_l(x, t)$$

Where T_s and T_l are temperature of solid and liquid phases respectively.

Energy balance equation at interface:

Let the interface is moved from *x* to *x*+*Δx* within the time *Δt*. Amount of material that has solidified over the time $\Delta t = \rho_c A\ \Delta x$.

Heat rejected at the interface= $\rho_c A\ \Delta x L$.

L= latent heat of the material, A = area of the interface, and ρ_c is the density of the casting material.

Rate of heat rejection at the interface = $\rho_c A L \frac{dx}{dt}$ (taking Δt→ 0)

The energy balance equation is in the following form:

$$q_l - q_s = \rho_c AL\frac{dx}{dt}$$

$$-\lambda_l\frac{\partial T_l}{\partial x} + \lambda_s\frac{\partial T_s}{\partial x} = \rho_c L\frac{dx}{dt}$$

$$\lambda_s\frac{\partial T_s}{\partial x} - \lambda_l\frac{\partial T_l}{\partial x} = \rho_c L\frac{dx}{dt} \tag{2.15}$$

Where q is the heat transfer rate and λ is the thermal conductivity of molten metal. At *x=s(t)*,the equation (2.15) can be written as,

$$\lambda_s\frac{\partial T_s}{\partial x} - \lambda_l\frac{\partial T_l}{\partial x} = \rho_c L\frac{ds(t)}{dt} \tag{2.16}$$

The assumed solution for the solid phase,

$$T = T_0 + B\,erf\left(\frac{x}{2\sqrt{\propto_s t}}\right) \tag{2.17}$$

Where B is a constant.

$$At\ x = s(t),\ \ T = T_f = T_0 + B\,erf\left[\frac{s(t)}{2\sqrt{\propto_s t}}\right] \tag{2.18}$$

$$\text{Let} \qquad \zeta = \left(\frac{s(t)}{2\sqrt{\propto_s t}}\right) = constant \tag{2.19}$$

Erf (ζ) is called error function. The error function is given by,

$$erf(x) = \frac{2}{\sqrt{\pi}}\int_0^x e^{-\eta^2}d\eta \tag{2.20}$$

$$\text{erf(x)} = \frac{2}{\sqrt{\pi}}\left(x - \frac{x^3}{3.1!} + \frac{x^5}{5.2!} - \frac{x^7}{7.3!} + \cdots\right)$$

Up to (n+1) terms the error function is expressed by,

$$\text{erf(x)} = \frac{2}{\sqrt{\pi}}x + \sum_{n=1}^{n}\frac{2}{\sqrt{\pi}}(-1)^n\frac{\zeta^{(2n+1)}}{(2n+1)n!}$$

From equation (2.18),

$$B = \frac{T_f - T_0}{\text{erf}(\zeta)} \tag{2.21}$$

Substitute the value of *B* into equation 2.17, so the solution of the equation 2.17 is,

$$\frac{T - T_0}{T_f - T_0} = \frac{erf\left[\frac{x}{2\sqrt{\propto_s t}}\right]}{erf(\zeta)} \tag{2.22}$$

Assume a solution for the liquid phase,

$$T = T_i + C\ erfc\left(\frac{x}{2\sqrt{\propto_l t}}\right) \tag{2.23}$$

Where C is a constant.

The error function has been represented in equation 2.20, which is given by,

$$erf(\text{x}) = \frac{2}{\sqrt{\pi}} \int_0^{\text{x}} e^{-\eta^2} d\eta$$

Where η is the variable of integration. The complementary error function denoted by "*erfc*". The complementary error function can be represented as,

$$erfc(\text{x}) = \frac{2}{\sqrt{\pi}} \int_x^{\infty} e^{-\eta^2} d\eta \tag{2.24}$$

At *x=s(t)*, the equation (2.23) can be written as,

$$T = T_f = T_i + C\ erfc\left[\frac{s(t)}{2\sqrt{\propto_l t}}\right] \tag{2.25}$$

$$C = \frac{T_f - T_i}{erfc\left[\frac{s(t)}{2\sqrt{\propto_s t}}\sqrt{\frac{\alpha_s}{\alpha_l}}\right]}$$

$$C = \frac{T_f - T_i}{erfc\left(\zeta\sqrt{\frac{\alpha_s}{\alpha_l}}\right)}$$

Substitute the value of C into equation 2.23, so the solution of the equation 2.23 is,

$$\frac{T - T_i}{T_f - T_i} = \frac{erfc\left[\frac{x}{2\sqrt{\propto_l t}}\right]}{erfc\left(\zeta\sqrt{\frac{\alpha_s}{\alpha_l}}\right)} \tag{2.26}$$

Using the relation of the error function $\frac{d}{dx}erf(x) = \frac{2}{\sqrt{\pi}}e^{-x^2}$, from equation (2.17),

$$\frac{\partial T_s}{\partial x} = B\frac{2}{\sqrt{\pi}}\left(e^{\frac{x^2}{4\propto_s t}}\right)\frac{1}{2\sqrt{\propto_s t}}$$

$$\left.\frac{\partial T_s}{\partial x}\right|_{x=s(t)} = B\frac{e^{-\zeta^2}}{\sqrt{\pi \propto_s t}}$$

The relation between error function and complementary error function is,

erfc(x)=1-erf(x)

Now, from equation (2.23),

$$\frac{\partial T_l}{\partial x} = C\frac{\partial}{\partial x}\left[1 - erf\left(\frac{x}{2\sqrt{\propto_l t}}\right)\right]$$

$$\frac{\partial T_l}{\partial x} = -C\frac{2}{\sqrt{\pi}}\left(e^{-\frac{x^2}{4\propto_l t}}\right)\frac{1}{2\sqrt{\propto_l t}}$$

$$\left.\frac{\partial T_l}{\partial x}\right|_{x=s(t)} = -C\frac{e^{-\zeta^2\frac{\alpha_s}{\alpha_l}}}{\sqrt{\pi \propto_s t}}$$

And, from equation (2.19),

$$s(t) = 2\zeta\sqrt{\propto_s t} \tag{2.27}$$

$$\frac{ds(t)}{dx} = \zeta\frac{\propto_s}{t}$$

Substitute the value of $\frac{\partial T_s}{\partial x}$, $\frac{\partial T_l}{\partial x}$ and $\frac{ds(t)}{dx}$ into equation 2.16,

$$\lambda_s\left[B\frac{e^{-\zeta^2}}{\sqrt{\pi \propto_s t}}\right] + \lambda_l\left[C\frac{e^{-\zeta^2\frac{\alpha_s}{\alpha_l}}}{\sqrt{\pi \propto_s t}}\right] = \rho_c L\zeta\sqrt{\frac{\alpha_s}{t}}$$

$$\lambda_s\left[\frac{T_f - T_0}{erf(\zeta)}\frac{e^{-\zeta^2}}{\sqrt{\pi \propto_s}}\right] + \lambda_l\left[\frac{T_f - T_i}{erfc\left(\zeta\sqrt{\frac{\alpha_s}{\alpha_l}}\right)}\frac{e^{-\zeta^2\frac{\alpha_s}{\alpha_l}}}{\sqrt{\pi \propto_s}}\right] = \rho_c L\theta\zeta\sqrt{\propto_s} \quad (2.28)$$

The values of ζ and *erf (ζ)* can be found out by trial and error method from equation (2.28).

2.3.2 Solution Methodology

This simulation focused on an aluminium casting with a steel mould. The metal was poured at a temperature higher than the freezing point of the material. The temperature of the metal-mould interface was taken as the initial mould temperature. The thickness of the casting was set to be 60 mm. The thermophysical properties of aluminium and steel are represented in table 2.2 [157].

Table 2.2: Thermophysical properties of aluminium and steel.

Name	Property	Value	Unit
Aluminium	Thermal conductivity (liquid)	100	W/m K
	Thermal conductivity (solid)	200	W/m K
	Specific heat (liquid)	1200	J/kg K
	Specific heat (solid)	1060	J/kg K
	Density	2690	kg/m^3
	Freezing Temperature	933	K
	Latent heat	391	kJ/kg
Steel	Thermal conductivity	33	W/m K
	Specific heat	486	J/kg K
	Density	7753	kg/m^3

The calculations begin by selecting a small, random value for ζ. This value is used to determine the corresponding values of erf(ζ), $\zeta\sqrt{(\alpha_s/\alpha_l)}$, and erfc($\zeta\sqrt{\alpha_s/\alpha_l}$). The values of erf(ζ), $\zeta\sqrt{(\alpha_s/\alpha_l)}$, and erfc($\zeta\sqrt{\alpha_s/\alpha_l}$) have been inserted into equation 2.28. The left-hand side (LHS) and right-hand side (RHS) of equation (2.28) are being calculated. If the difference between the value of LHS

and RHS is insignificant, then that specific value of ζ is allowable. Once the value of ζ is obtained, the calculation of the total solidification time is performed. The total solidification time of casting is computed by using the equation 2.19. In that equation t is the total solidification time. Subsequently, the length of the solidified metal has been determined for a specific time interval. Equation 2.27 is used to calculate the length of metal solidified at each time. In that equation, the length of solidified metal at a given time is denoted by s(t). All the calculations are performed using FORTRAN 95 programming software.

2.3.3 Validation

This model has been validated by comparing it to the casting process presented in existing work [155]. They [155] utilized a copper mould for iron casting with a thickness of 100 mm. Their model was one-dimensional (1-D), with the dimension perpendicular to the mould-casting face. They calculated the solidification time to be 42.1 s. The solidification time was also determined using the current model, resulting in a value of 42 s. The calculated value (42 s) shows good agreement with the previous work [155].

2.3.4 Results and Discussion

In this simulation, three different initial temperatures of the mould were considered: 303 K (30°C), 403 K (130°C) and 503 K (230°C). The model has then been applied to each of these cases with three different pouring temperatures: 983 K (superheat = 50), 1003 K (superheat = 70), and 1033 K (superheat = 100). As a result, nine simulations have been carried out, where each pouring temperature has been varied with different mould initial temperature. The aim of this study is to investigate how the mould initial temperature and pouring temperature affect the solidification process of the casting.

Table 2.3, table 2.4, and table 2.5 show the solidification times for different pouring temperatures and mould initial temperatures, while figure 2.7 illustrates the variation of solidification time with these parameters.

2.3.4.1 Solidification Time

Table 2.3: Variation in solidification time with different pouring temperatures at a mould initial temperature of 303 K.

Mould initial temperature= 303 K (30^{0}C)					
Pouring Temperature	**ζ**	**erf(ζ)**	**$\zeta\sqrt{(\alpha_s/\alpha_l)}$**	**erfc($\zeta\sqrt{\alpha_s/\alpha_l}$)**	**Solidification Time (s)**
983 K	0.7250	0.6949	1.0910	0.1226	6.10
1003 K	0.7129	0.6868	1.0727	0.1290	6.31
1033 K	0.6956	0.6749	1.0467	0.1386	6.63

Table 2.4: Variation in solidification time with different pouring temperatures at a mould initial temperature of 403 K.

Mould initial temperature=403 K (130^{0}C)					
Pouring Temperature	**ζ**	**erf(ζ)**	**$\zeta\sqrt{(\alpha_s/\alpha_l)}$**	**erfc($\zeta\sqrt{\alpha_s/\alpha_l}$)**	**Solidification Time (s)**
983 K	0.6794	0.6635	1.0223	0.1480	6.95
1003 K	0.6674	0.6549	1.0042	0.1553	7.20
1033 K	0.6503	0.6424	0.9785	0.1662	7.59

Table 2.5: Variation in solidification time with different pouring temperatures at a mould initial temperature of 503 K.

Mould initial temperature= 503 K (230^{0}C)					
Pouring Temperature	**ζ**	**erf(ζ)**	**$\zeta\sqrt{(\alpha_s/\alpha_l)}$**	**erfc($\zeta\sqrt{\alpha_s/\alpha_l}$)**	**Solidification Time (s)**
983 K	0.6260	0.6241	0.9420	0.1826	8.19
1003 K	0.6142	0.6151	0.9241	0.1910	8.50
1033 K	0.5974	0.6019	0.8988	0.2035	8.99

The corresponding values of ζ, erf (ζ), $\zeta\sqrt{(\alpha_s/\alpha_l)}$, and $\text{erfc}(\zeta\sqrt{\alpha_s/\alpha_l})$ are shown in these tables, which are determined by solving numerical equations and are necessary for solidification time calculations.

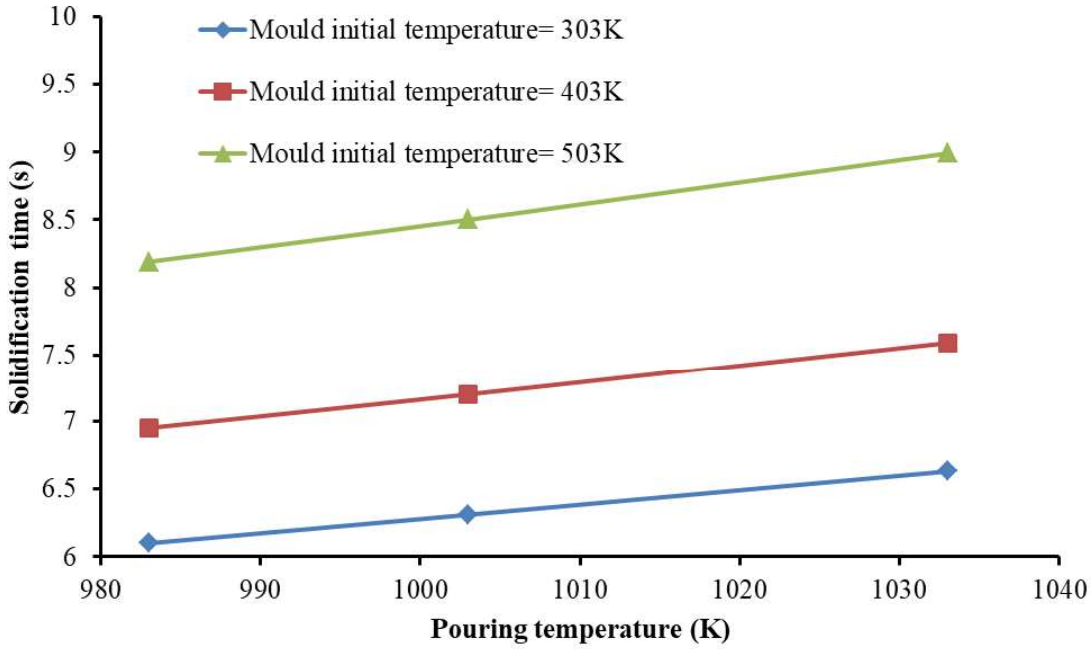

Figure 2.7: Variation of solidification time with pouring and mould initial temperatures.

As the pouring temperature or mould initial temperature increases, the solidification time also increases. This is because higher temperatures casting require more time to cool, resulting in longer solidification times [156]. Furthermore, the solidification time is found to increase almost linearly with pouring temperature.

2.3.4.2 Solidification Front

Table 2.6 illustrate the length of metal that solidified at various intervals of time, pouring temperature, and initial mould temperature. The variation of solidified metal length from the mould casting interface over time is shown in figure 2.8, figure 2.9, and figure 2.10.

For a pouring temperature of 983 K and mould initial temperature of 303 K, the solidified lengths of casting metal after 1 s, 2 s, 3 s, 4 s, 5 s, and 6.10 s from the mould-metal interface are 12.14 mm, 17.17 mm, 21.03 mm, 24.29 mm, 27.16 mm, and 30 mm, respectively. The entire casting material solidifies after 6.10 s. The solidification initially occurs rapidly and then

gradually slows down due to a big temperature drop happens initially because of the high heat content at initially [156]. The length of solidified casting metal is 12.14 mm in the first 1 s, 5.03 mm in the next 1 s, and decreases as time progresses. The average casting solidification rate is calculated as the ratio of the total length of casting metal solidified to the total casting solidification time, which is 6.25 mm/s for this case.

Table 2.6: Variations in metal solidification length at different time intervals, mould initial temperatures, and pouring temperatures.

Time (s)	**Length of metal solidified from mould-casting interface (mm)**								
	Mould initial temperature = 303 K (30^0C)			**Mould initial temperature = 403 K(130^0C)**			**Mould initial temperature = 503 K(230^0C)**		
	T_P = 983K	**T_P =1003K**	**T_P =1033K**	**T_P =983K**	**T_P =1003K**	**T_P =1033K**	**T_P = 983K**	**T_P =1003K**	**T_P =1033K**
0	0	0	0	0	0	0	0	0	0
1	12.14	11.94	11.65	11.38	11.18	10.89	10.49	10.29	10.01
2	17.17	16.89	16.48	16.09	15.81	15.40	14.83	14.55	14.15
3	21.03	20.68	20.18	19.71	19.36	18.87	18.16	17.82	17.33
4	24.29	23.88	23.30	22.76	22.36	21.79	20.97	20.57	20.01
5	27.16	26.70	26.05	25.45	24.99	24.36	23.45	23	22.37
6	29.75	29.25	28.54	27.87	27.38	26.68	25.68	25.20	24.51
t_s	30	30	30	30	30	30	30	30	30

Similarly, for an initial mould temperature of 303 K and pouring temperature of 1003 K, the average solidification rate is 6.1 mm/s, and for 1033 K, it is 5.9 mm/s. The average solidification rate decreases with increasing pouring temperature at a constant mould initial temperature because a higher temperature body takes longer to cool down.

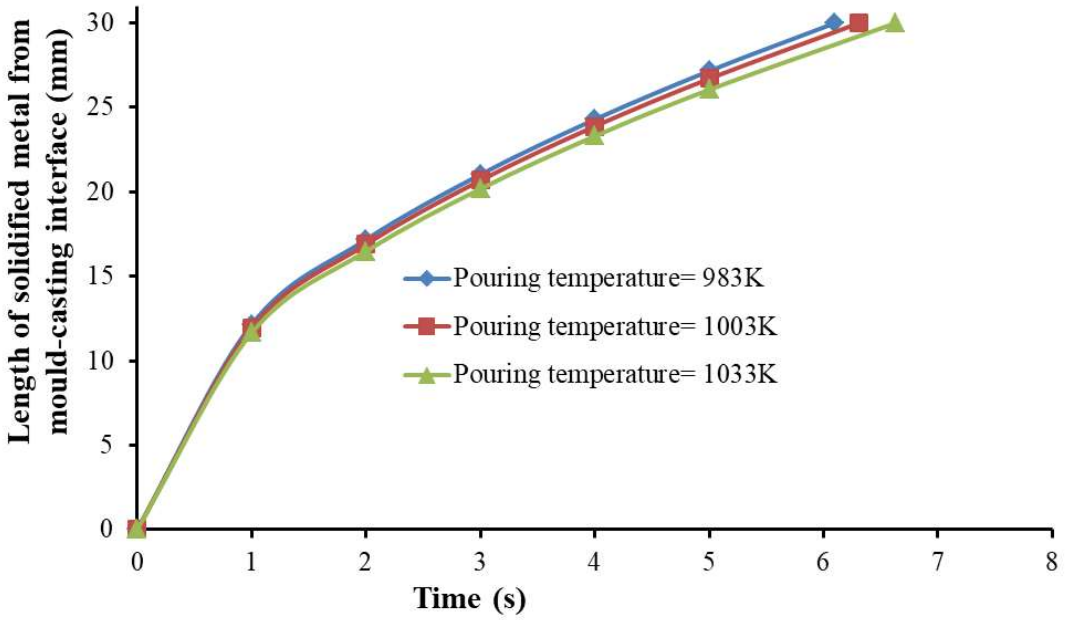

Figure 2.8: Length of metal solidified for different time intervals and pouring temperatures at T_0=303 K.

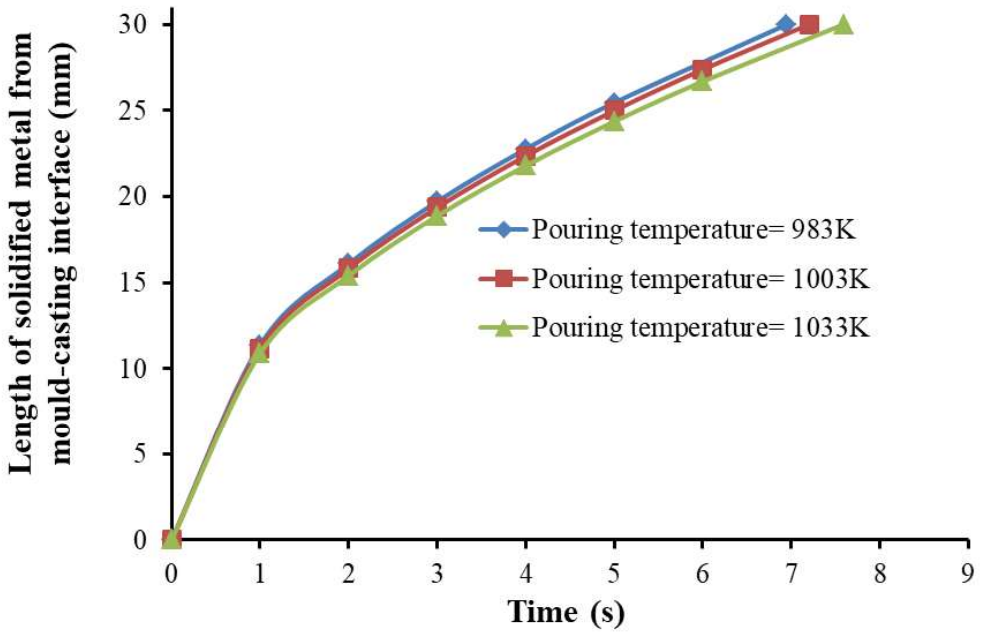

Figure 2.9: Length of metal solidified for different time intervals and pouring temperatures at T_0=403 K.

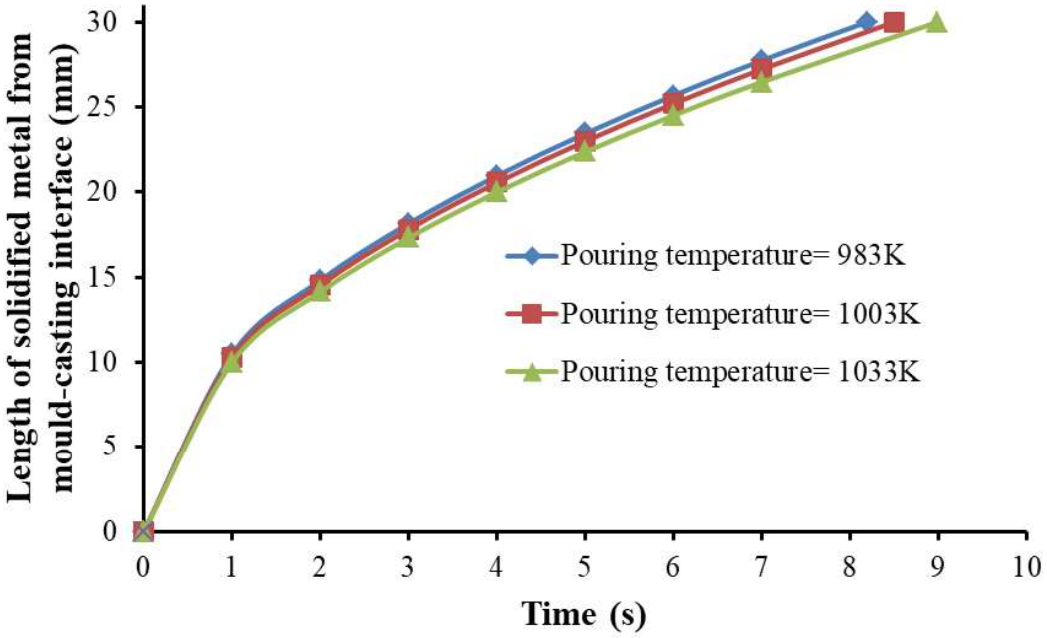

Figure 2.10: Length of metal solidified for different time intervals and pouring temperatures at T_0=503 K.

For an mould initial temperature of 403 K, the average solidification rates for pouring temperatures of 983 K, 1003 K, and 1033 K are 5.71 mm/s, 5.36 mm/s, and 5.18 mm/s, respectively. Similarly, for an initial mould temperature of 503 K, the average solidification rates for pouring temperatures of 983 K, 1003 K, and 1033 K are 4.73 mm/s, 4.62 mm/s, and 4.46 mm/s, respectively. At a constant pouring temperature, the average solidification rate decreases with increasing mould initial temperature.

Three different pouring temperatures were tested: 983 K, 1003 K, and 1033 K, resulting in solidification times of 6.1 s, 6.31 s, and 6.63 s, respectively. Since the solidification time values are close to each other, it can be observed that the average cooling rates (calculated as the thickness of the solidified metal divided by the solidification time, mm/s) are approximately the same for all three pouring temperatures. The length of metal solidified from the mould-casting interface at a given time and with an initial mould temperature of remains relatively consistent as shown in figure 2.8, figure 2.9, and figure 2.10.

2.4 Conclusions

In this chapter, two one-dimensional casting solidification models have been simulated. The FORTRAN 95 programming software was utilized to simulate the models. By using the first model, it was possible to calculate the solidification front, which is the length of the casting metal that has solidified from the interface with the mould. The simulation results indicated that the solidification time was 42.1 s, with an average solidification rate of 1.88 mm/s. During the first 10 seconds after pouring, the solidification rate was found to be 2.44 mm/s, followed by 1.01 mm/s during the subsequent 10 s, and finally 0.77 mm/s during the following 10 s. These results indicate that rapid solidification occurred initially.

In the first model, the pouring temperature of the material was fixed as the freezing temperature and could not be altered during the simulation. Pouring temperature is a crucial parameter in casting as it impacts both the solidification time and the position of the solidification front. Unfortunately, due to the limitations of the model, only the mould temperature can be varied to observe its effect on the solidification process.

The pouring temperature and mould initial temperature both can vary in the second solidification model. The second one-dimensional mathematical model used in this section is based on the error function and complementary error function. The model is used to simulate the solidification process of a casting and calculate the solidification times for different pouring temperatures and different mould initial temperatures. The simulation results showed that the solidification time increases with pouring temperature at constant mould initial temperature and solidification time also increases with mould initial temperature at constant pouring temperature. Furthermore, the solidification time is found to increase almost linearly with pouring temperature. The solidification front has also been calculated using this model. The model showed that rapid solidification occurs initially, followed by a relatively slow cooling process. The average solidification rate decreases with increasing pouring temperature at a constant mould initial temperature and it decreases with increasing mould initial temperature at a constant pouring temperature.

It is important to note that in both models, pouring velocity has not been varied. Therefore, the effect of pouring velocity on solidification could not be investigated. The porosity cannot be calculated using both models. Additional models would be needed to predict or measure porosity formation in the casting.

CHAPTER 3: CASTING BY THREE DIMENSIONAL MODEL

3.1 Introduction

The previous models were used to calculate the solidification time and length of solidified metal at different times in chapter 2. These models were one-dimensional and simple, meaning they only considered one direction and were easy to understand. The first model allowed for the variation of pouring temperature, which is the temperature of the liquid metal being poured into the mould cavity. The second model allowed for the variation of pouring temperature and the mould initial temperature. However, these models were not able to vary the pouring velocity; an important casting parameter that refers to the speed at which liquid metal is poured through the sprue into the mould cavity. They also couldn't calculate the air porosity. The air porosity in the solidified casting is measured by the ratio of the total volume of air present in the solidified casting to the total volume of the casting. Since the pouring velocity was not considered in these models, the solidification front, which is the boundary between the solid and liquid metal, could not be accurately determined.

In this chapter a three dimensional model has been created where the model is more accurate in practical idea. Because the casting process is complex, researchers made some assumptions to simplify the casting process. Some researchers assumed that solidification only starts after the mould cavity is completely filled with molten metal [158, 159, 160, 161]. Different researchers have different assumptions about the flow inside the mould cavity. Some researchers assumed that the flow is laminar, regardless of the pouring velocity [116, 162, 163, 164, 165]. Meanwhile, other researchers discussed casting without considering the presence of air in the mould cavity [156, 166, 167].

The aim of this chapter is to create a more practical simulation model that can accurately simulate the casting process. It is expect that solidification will begin at the beginning of the metal being poured. In this study, a two-phase system consisting of air and aluminium has been used to simulate the filling and solidification of aluminium in the mould cavity. The flow inside

the mould cavity is either laminar or turbulent, and this is determined by the Renolds number, which is calculated based on the pouring velocity. The natural convection that occurs between the mould outside surface walls and atmosphere has also been taken into account. This model allows for the variation of pouring velocity, pouring temperature, and mould initial temperature. Furthermore, this model can determine the air porosity and clear solidification analysis.

3.2 Computational Model for Solidification

To simulate the casting process, Ansys Fluent [168] is employed. The process of filling a casting is a time-dependent flow of a viscous, incompressible liquid with a free surface. The two phase volume of fluid model (VOF) is used to track the position of interface of the two fluids [49]. The mould was initially filled with air and molten aluminium is poured in the mould cavity. Therefore, the primary phase or fluid is air and secondary phase or fluid is aluminium. The RNG k-ε method has been used to model the turbulence inside the mould cavity. The RNG k-epsilon turbulence model is useful for predicting flow patterns in confined flow systems. Nzebuka et al. [169] and Waheed et al. [89] used the RNG k-epsilon turbulence model to investigate flow patterns and turbulent transport quantities in a horizontal direct-chill casting system. Solidification model and energy model has been taken for a more comprehensive understanding of the casting process. Solidification modelling involves simulating and predicting the solidification behaviour of the molten metal as it cools and solidifies inside the mould. Energy modelling focuses the heat transfer and thermal behaviour during the casting process. Conjugate heat transmission happens in the casting process. The numerical analysis of the casting solidification process taking into account the motions of the molten metal is dependent on the solution of the system of the following equations [49, 168, 169, 89, 170, 171]: Reynolds-averaged Navier-Stokes (RANS) equations, energy equation, volume fraction equation, and turbulent k-ε equation.

3.2.1 Reynolds-averaged Navier-Stokes (RANS) Equations

The instantaneous continuity equation describes the conservation of mass in a fluid, while the instantaneous momentum equations describe the conservation of momentum. However, these equations are difficult to solve for turbulent flows because the turbulence introduces fluctuations in the flow variables that are difficult to predict or model accurately [89, 170, 172]**.** Reynolds averaging separates the flow variables into mean or time average component and fluctuating component. In Reynolds averaging, the variables are divided into mean (ensemble or time-averaged) and fluctuating components [170, 173]. For the velocity component *u*,

$$u = \overline{u} + \acute{u} \tag{3.1}$$

Where $\overline{u}$ and ú are mean (ensemble-averaged or time-averaged) and fluctuating components of velocity.

Likewise, for pressure and other scalar quantities: $\psi = \overline{\psi} + \acute{\psi}$**.** Where ψ denotes a scalar such as pressure or energy. In Reynolds averaging, the flow variables, such as velocity, pressure, and density, are decomposed into their mean and fluctuating components. The mean component represents the time-averaged behaviour of the flow, while the fluctuating component captures the turbulent fluctuations around the mean. The Reynolds-averaged Navier-Stokes (RANS) equations are obtained by substituting the decomposed variables into the instantaneous continuity and momentum equations and then taking the time average component (and neglecting the overbar on time average component, like velocity is written as u instead of $\overline{u}$) [170]. The resulting equations provide a closure model for turbulent flows, where the effects of turbulence are modelled using additional terms such as the Reynolds stresses, which represent the effects of the fluctuating velocities on the mean flow.

The ensemble-averaged or time-averaged continuity and momentum equations can be written as:

The continuity equation,

$$\frac{\partial \rho}{\partial t} + \nabla.(\rho \vec{v}) = 0 \tag{3.2}$$

The momentum equation,

$$\frac{\partial(\rho \vec{v})}{\partial t} + \nabla.(\rho \vec{v}\vec{v}) = -\nabla p + \rho \vec{g} + \nabla.[\mu \nabla \vec{v}] + \frac{\partial(-\rho \overline{u_i' u_j'})}{\partial x_j} + \vec{F} \tag{3.3}$$

Where $\vec{v}$ represents velocity vector, μ denotes the dynamic viscosity coefficient, $\vec{g}$ represents the gravitational acceleration vector, and $\vec{F}$ is the source term used to modify the momentum equations in the mushy region. The Carman-Koseny model, suggested a formulation for the source term as follows [174],

$$\vec{\mathrm{F}} = -\frac{\mathrm{C_{mush}} \vec{\mathrm{v}} (1-\beta)^2}{\beta^3 + \epsilon}$$

Here, C_{mush} is the mushy zone constant which is equal to 10^4 [170], and to prevent division by zero, the constant ϵ is assigned a value of 0.001.

Equations 3.2 and 3.3 are known as Reynolds-averaged Navier-Stokes (RANS) equations, which have a similar structure to the instantaneous Navier-Stokes equations [170, 175]. However, in the RANS equations, the velocities and other solution variables represent ensemble-averaged or time-averaged values [175, 176]. The process of substituting expressions for the flow variables into the instantaneous momentum and continuity equations and taking a time (or ensemble) average is known as Reynolds averaging [175, 177, 178]**.** This is a mathematical technique used in fluid dynamics to separate the mean flow from the fluctuating or turbulent flow.

The additional term in the Reynolds-averaged momentum equation is the Reynolds stress tensor, which represents the effects of the fluctuating velocities on the mean flow. The Reynolds stress tensor is a symmetric, second-order tensor. It is defined as [179],

$$\mathrm{R}_{ij} = -\rho \overline{u_i' u_j'} \tag{3.4}$$

Where R_{ij} is the Reynolds stress tensor, u_i' is the fluctuating velocity in the *i*-th direction, and u_j' is the fluctuating velocity in the *j*-th direction. The negative sign arises because the Reynolds stress tensor represents the transfer of momentum from the fluctuating velocities to the mean flow. The overbar indicates the product of the two fluctuating components. Since the Reynolds stress tensor is a symmetric tensor, and its components can be expressed in terms of the Reynolds stresses in the x, y, and z directions,

$$\mathrm{R}_{xx} = -\rho\overline{u_x' u_x'}$$

$$\mathrm{R}_{yy} = -\rho\overline{u_y' u_y'}$$

$$\mathrm{R}_{zz} = -\rho\overline{u_z' u_z'}$$

$$\mathrm{R}_{xy} = \mathrm{R}_{yx} = -\rho\overline{u_x' u_y'}$$

$$\mathrm{R}_{xz} = \mathrm{R}_{zx} = -\rho\overline{u_x' u_z'}$$

$$\mathrm{R}_{yz} = \mathrm{R}_{zy} = -\rho\overline{u_y' u_z'}$$

Where the subscripts denote the directions in which the Reynolds stress is measured.

3.2.2 RNG k-ε Equations

The RNG k-ε model is a turbulence model used in computational fluid dynamics (CFD) simulations to predict turbulent flows [49, 89, 180]**.** The RNG model presents equations for turbulent kinetic energy (k) and dissipation rate (ε) that are used to calculate the Reynolds stresses and other turbulence parameters. Turbulent kinetic energy (k) represents the energy associated with the turbulent fluctuations in the velocity field. Dissipation rate (ε) represents the rate at which turbulent kinetic energy is dissipated due to viscous effects.

The equations for turbulent kinetic energy (k) and dissipation rate (ε) in the RNG model are as follows:

Equation for turbulent kinetic energy (k),

$$\frac{\partial(\rho k)}{\partial t} + \nabla.(\rho k\vec{v}) = \nabla.\left(\propto_k \mu_{eff}\nabla k\right) + G_k + G_b - \rho\varepsilon \tag{3.5}$$

Equation for dissipation rate (ε),

$$\frac{\partial(\rho\varepsilon)}{\partial t} + \nabla.(\rho\varepsilon\vec{v}) = \nabla.\left(\propto_{\varepsilon} \mu_{eff}\nabla\varepsilon\right) + C_{\varepsilon 1}\frac{\varepsilon}{k}(G_k + C_{\varepsilon 3}G_b) - C_{\varepsilon 2}\rho\frac{\varepsilon^2}{k} - R_{\varepsilon} \tag{3.6}$$

The effective viscosity is defined as,

$$\mu_{eff} = \mu + \mu_t \tag{3.7}$$

Where μ is the molecular viscosity of the fluid and μ_t is the turbulent viscosity.

The turbulent viscosity is then computed using the following equation,

$$\mu_t = \rho C_{\mu}\frac{k^2}{\varepsilon} \tag{3.8}$$

Where ρ is the density of the fluid, C_{μ} is a model constant and C_{μ}= 0.085 which has been derived using the Renormalization Group (RNG) theory. The term G_k denotes the generation of turbulence kinetic energy as a result of the mean velocity gradients. This term arises from the fact that mean velocity gradients in the fluid can induce the formation of turbulent eddies, which in turn generate turbulence kinetic energy. G_k depends on the Reynolds stress tensor [170, 181]. It can be expressed as,

$$G_k = -\rho\overline{u_i' u_j'}\frac{\partial u_j}{\partial x_i} \tag{3.9}$$

Where u_j is the velocity component in the j-th direction and x_i is the spatial coordinate in the i-th direction. The term G_b represents the rate at which turbulence kinetic energy is generated due to the effects of buoyancy [182]. It can be expressed as,

$$G_b = -g_i\frac{\mu_t}{Pr_t\mu}\frac{\partial p}{\partial x_i} \tag{3.10}$$

Where Pr_t is the turbulent Prandtl number and g_i is the component of the gravity vector in the i-th direction. The default value of the turbulent Prandtl number for the standard and realizable k- ε models is 0.85. However, In the case of the RNG k-ε model [170, 183],

$$Pr_t = \frac{1}{\alpha_{eff}} \text{ and } \alpha = \frac{1}{Pr} = \frac{k}{\rho c_p} \tag{3.11}$$

The α_{eff} is given by [183],

$$\left|\frac{\alpha_{eff}-1.3929}{\alpha-1.3929}\right|^{0.6321}\left|\frac{\alpha_{eff}+2.3929}{\alpha+2.3929}\right|^{0.3679}=\frac{\mu}{\mu_{eff}} \tag{3.12}$$

ρ is the density of the fluid, c_p is the specific heat at constant pressure, α_{eff} is the effective thermal diffusivity, α is the molecular thermal diffusivity. μ is the molecular viscosity or viscosity of the fluid and μ_{eff} is the effective viscosity.

The degree to which ε is impacted by the buoyancy is determined by the constant $C_{\varepsilon 3}$. The constant $C_{\varepsilon 3}$ in the RNG k-ε turbulence model can be determined using the following equation [170, 184]:

$$C_{\varepsilon 3}=\tanh\left|\frac{v}{u}\right| \tag{3.13}$$

The terms "v" and "u" refer to the components of the velocity vector that are parallel and perpendicular to the direction of gravity, respectively. Therefore, when the flow direction is perpendicular (normal) to the direction of gravity, the value of $C_{\varepsilon 3}$ is zero. On the other hand, when the flow direction is parallel to the direction of gravity, the value of $C_{\varepsilon 3}$ is equal to 1.

The main difference between the RNG and standard k-ε models lies in the additional term R_ε in the turbulence dissipation rate equation [185]. This term is a correction factor that accounts for the curvature effects on the turbulence structure [186].

$$R_\varepsilon=\frac{C_\mu\rho{\eta_1}^3(1-\frac{\eta_1}{\eta_0})}{1+C_\beta{\eta_1}^3}\frac{\varepsilon^2}{k} \tag{3.14}$$

Where $\eta_1=Sk/\varepsilon$, η_0 =4.38, C_β=0.012

The modulus of the mean rate-of-strain tensor (S) is a scalar quantity used in turbulence modelling to describe the deformation rate of a fluid flow [187]**.** It is defined as,

$$S=\sqrt{2S_{ij}S_{ij}} \tag{3.15}$$

Where S_{ij} is the mean rate-of-strain tensor, which describes the deformation of fluid particles due to the velocity gradient. The mean rate-of-strain tensor is defined as,

$$S_{ij} = \frac{1}{2}\left(\frac{\partial u_i}{\partial x_j} + \frac{\partial u_j}{\partial x_i}\right) \tag{3.16}$$

Where u_i and u_j are the velocity components in the i and j directions, respectively, and x_i and x_j are the corresponding coordinate axes. The inverse effective Prandtl numbers (α_k and α_ε) are calculated using the equation 3.12 and default value in Ansys Fluent are [170], $\alpha_k = \alpha_\varepsilon \approx 1.393$. The default values in Ansys Fluent of the model constants $C_{\varepsilon 1}$ and $C_{\varepsilon 2}$ are 1.42 and 1.68 respectively.

3.2.3 Volume Fraction Equation

The VOF (Volume of Fluid) model is used for tracking the interface between two or more immiscible fluids. It is particularly useful when the position of the interface is of interest. In this model, a single momentum equation is solved across the entire domain, and the resulting velocity field is shared among the different phases [170]. The volume fraction of each fluid is tracked in each computational cell throughout the domain. The VOF formulation is based on the assumption that multiple fluids or phases do not mix each other. When modelling multiple phases, a volume fraction variable is introduced for each phase in every computational cell. The volume fraction represents the ratio of the volume occupied by a particular phase in a cell to the total volume of the mixture or cell. In each control volume (cell), the sum of the volume fractions of all phases is always equal to one. The properties are shared among the phases and represent volume-averaged values. Thus, Depending on the volume fraction values, the properties within a given cell can either purely represent one of the phases or represent a mixture of the phases. In a two-phase system, considering the subscripts "a" and "b" represent the primary and secondary phases, respectively. The volume fractions of these phases in a specific cell are denoted as φ_a and φ_b. In this context, there are three possible scenarios within a given cell: $\varphi_b = 0$: The secondary (b^{th}) phase is absent in the cell. $\varphi_b = 1$: the secondary (b^{th}) phase completely fills the cell. $0 < \varphi_b < 1$: both phases are present in the cell, and there is an interface between the secondary (b^{th}) phase and the primary (a^{th}) phase.

To keep track of the interface(s) between the phases, a continuity equation is solved for the volume fraction of secondary (b^{th}) phase. For secondary (b^{th}) phase, the equation takes the following form,

$$\frac{\partial(\varphi_b \rho_b)}{\partial t} + \nabla.(\varphi_b \rho_b \vec{v}) = \dot{m}_{ab} - \dot{m}_{ba} \tag{3.17}$$

Where $\dot{m}_{ab}$ represents the mass transfer rate from phase a to phase b, and $\dot{m}_{ba}$ represents the mass transfer rate from phase b to phase a. $\vec{v}$ is the velocity vector and t is the time. The primary-phase volume fraction is determined based on the following constraint in a cell,

$$\varphi_a + \varphi_b = 1 \tag{3.18}$$

The properties used in the transport equations are calculated by the presence of the component phases in each control volume. The volume fraction averaged approach is utilized to calculate every mixture property within each cell. For example, the density of a two-phase mixture (ρ) in a cell is determined by,

$$\rho = \varphi_a \rho_a + \varphi_b \rho_b = (1 - \varphi_b)\rho_a + \varphi_b \rho_b \tag{3.19}$$

Where ρ_a represents the density of the phase a, and ρ_b represents the density of the phase b. Similarly, the viscosity of a two-phase mixture in a cell is

$$\mu = (1 - \varphi_b)\mu_a + \varphi_b \mu_b \tag{3.20}$$

3.2.4 Liquid Fraction and Energy Equation

In ANSYS Fluent, the enthalpy-porosity technique is employed to model the solidification process. This technique does not explicitly track the melt interface but instead utilizes a parameter known as the liquid fraction. The liquid fraction represents the fraction of the cell volume that is in the liquid state. During each iteration of the simulation, the liquid fraction is calculated based on an enthalpy balance. By tracking the changes in enthalpy and using the computed liquid fraction, this technique can determine the regions where phase change occurs and the corresponding distribution of solid and liquid phases. The mushy zone refers to a region within a material where both solid and liquid phases coexist and the liquid fraction ranges

between 0 and 1. At the start of solidification, when the material is entirely liquid, the liquid fraction is 1. As solidification proceeds, the liquid fraction gradually decreases as more of the material transforms into a solid phase. When the solidification process is complete in a cell, the liquid fraction in that cell reaches zero. This means that all the material in that cell has solidified. In a fully solidified cell, where the liquid fraction is zero, the velocities within the material also drop to zero. Voller and Prakash [188] employed the enthalpy-porosity method in their research on solidification theory.

The material enthalpy is determined as the sum of the sensible heat (h_1) and latent heat (h_2), as shown below:

$$\mathrm{h} = \mathrm{h}_1 + \mathrm{h}_2 \tag{3.21}$$

$$\mathrm{h}_1 = \mathrm{h}_{\mathrm{ref}} + \int_{\mathrm{T}_{\mathrm{ref}}}^{\mathrm{T}} \mathrm{C_P}\,\mathrm{dT} \tag{3.22}$$

Where h is the total enthalpy. The specific heat at constant pressure is denoted by C_p, the reference temperature is T_{ref}, and h_{ref} represents the reference enthalpy.

The latent heat component can be represented in terms of the latent heat of the material, L, and liquid fraction, β.

$$\mathrm{h}_2 = \beta \mathrm{L} \tag{3.23}$$

The liquid fraction can be addressed as:

$$\beta = \begin{cases} 0 \text{ if } T < T_{so} \\ \dfrac{T - T_{so}}{T_{li} - T_{so}} \text{ if } T_{so} < T < T_{li} \\ 1 \text{ if } T > T_{li} \end{cases} \tag{3.24}$$

Where T_{so} and T_{li} are the solidus and liquidus temperatures of molten metal. The latent heat component (h_2) may vary from zero (for solids) to L (for liquids).

The equation of energy is written as:

$$\frac{\partial(\rho E)}{\partial t} + \nabla.(\vec{v}(\rho E + p)) = \nabla.(\lambda_{eff}\nabla T) + \nabla.(\vec{\bar{\tau}}\vec{v}) + S_h \tag{3.25}$$

$$E = h - \frac{p}{\rho} + \frac{v^2}{2}$$

The Reynolds stress tensor $\bar{\bar{\tau}} = \mu_{eff}\left(\frac{\partial u_i}{\partial x_j} + \frac{\partial u_j}{\partial x_i}\right)$

The effective thermal conductivity (λ_{eff}) is obtained as:

$$\lambda_{eff} = \alpha_{eff} c_p \mu_{eff}$$

The value of α_{eff} is obtained by utilizing equation 3.12. The total energy is denoted by *E* and the effective conductivity is denoted by λ_{eff}. λ_t, pr_t, μ_t, and μ_{eff} are the turbulent thermal conductivity, turbulent Prandtl number, turbulent viscosity, and effective viscosity respectively. Energy transfer resulting from conduction and turbulence energy diffusion are represented by the first two terms on the right-hand side of the energy equation. The first term of left hand side is the rate of change of the total energy density and second term is the convective heat transfer due to the bulk fluid motion. S_h includes any volumetric heat sources and it is zero in this study.

3.2.5 Implementing the Model for Analysis

The system of all equations is solved by taking proper initial and boundary conditions using the Ansys Fluent [170]. The momentum equation was discretized using the implicit approach as suggested by Calderón-Ramos et al. [189]. The PRESTO [189] scheme was employed for pressure interpolation. The QUICK and compressive schemes were used to solve the energy and VOF (Volume of Fluid) equations respectively. The solution method currently utilizes a segregated algorithm based on pressure, such as the SIMPLEC algorithm, to solve the flow equations and determine the velocity field [189]. The evaluation of the turbulence equation coefficients is carried out using a first-order upwind scheme as suggested by Galván et al. [190]. The transient formulation is solved using a first-order implicit scheme [191].

To achieve a stable iterative process, under-relaxation factors are being employed as stated by Xu et al. [192]. The under-relaxation factor is a number used to update the solution variable during each iteration of a numerical process [193]. It helps control the rate of convergence and stability. The under-relaxation factors typically range between 0 and 1. The typical values of under-relaxation factors employed are 0.3 for pressure, 0.8 for density and body force, 0.7 for momentum, 0.5 for volume fraction, 0.9 for liquid fraction, 0.7 for turbulent kinematic energy and turbulent dissipation rate, 0.9 for turbulent viscosity, and 0.8 for liquid fraction and energy.

The iterative solution method is employed to solve the nonlinear equations that govern fluid flow. Convergence is reached when additional iterations become unnecessary, signifying that the solution has attained a stable state and satisfies the equations adequately [194]. In Ansys, the convergence of the solution is determined using a criterion based on the relative error [171], which is calculated as $e = \|\theta_{i+1} - \theta_i\| / \|\theta_i\|$. Here, θ_{i+1} and θ_i are the solutions obtained from consecutive iterations, and $\|\theta\|$ represents the Euclidean norm of θ. To determine convergence in Ansys, the relative error e is compared to the default residual target. Once the error e falls below this target, the solution is considered to have converged, indicating that further iterations are no longer necessary. The default residuals in Ansys for each time step are 0.001, 0.001, 0.000001, and 0.001 for the mass, momentum, energy, and turbulence equations, respectively. For each case, an iterative convergence solution is obtained by performing 4000 iterations at every time step.

Nzebuka et al. [169] also mentioned in their study that a long-time solution was computed until convergence was achieved at each time step**.** A time step of 10^{-5} s is used to initialise the calculation for the temporal convergence of all equations in the simulation. It is later (after 2 s of running the simulation) updated to 10^{-4} s to reduce the overall simulation completion time while maintaining equation convergence. This is being done in accordance with Wu et al [195]. The simulations were conducted on a machine with a Core-i7 processor and 32 GB RAM. Each simulation takes an average of 300-400 hours to complete.

3.3 Validation of the Model

For validation, the proposed model/method is compared with the experimental result of Mozammil et al. [116]. They have considered a bottom gated mould cavity for a plate measuring 100 mm × 50 mm × 25 mm and a bar 40 mm × 13 mm ×13 mm, as shown in figure 3.1. They used the green sand mould for pure aluminium casting. Dimensions of several components employed in the bottom gating casting are shown in table 3.1. They carried out experiments as well as simulations to find out porosity at different temperatures. The casting process involved a pouring time of about 12.5 s and a pouring velocity of about 250 mm/s.

The same mould geometry has been considered for the validation of our model. The casting process has been simulated by our proposed methods/model for various pouring temperatures. A total of 153101 quadrilateral elements were taken in the aluminium casting with sand mould. The mesh view is shown in figure 3.2. The thermophysical properties of aluminium and air are shown in table 3.3. The density, specific heat, and thermal conductivity of sand have been obtained from existing literature sources [196, 197], and their values are 1600 kg/m^3, 1170 J/kg-K, and 0.8655 W/m-K. Molten aluminium metal is poured from sprue inlet. At the inlet, velocity is the same as the pouring velocity of molten metal, and temperature is equal to the pouring temperature of molten metal. During the pouring process, the air is allowed to leave through the riser (outlet). A pressure outlet boundary condition (ambient air pressure) is imposed at the outlet. Six outside boundary surface walls of the mould are exposed to the atmosphere. The porosity in the solidified casting is measured by the ratio of the volume of air present in the solidified casting to the total volume of the casting.

Figure 3.3 and table 3.2 shows the porosity value obtained from the simulation and experimental results of Mozammil et al. [116] at various pouring temperatures. All the results were obtained by maintaining a constant pouring velocity of 250 mm/s and varying the pouring temperatures. According to the experimental results of Mozammil et al. [116], the porosity values at pouring temperatures of about 970 K, 1000 K, 1050 K, and 1075 K were found to be 0.0078, 0.0087, 0.0091, and 0.0095, respectively. On the other hand, their simulation results for porosity yielded

values of about 0.0073, 0.0076, 0.0082, and 0.0085, respectively, for the same pouring temperatures.

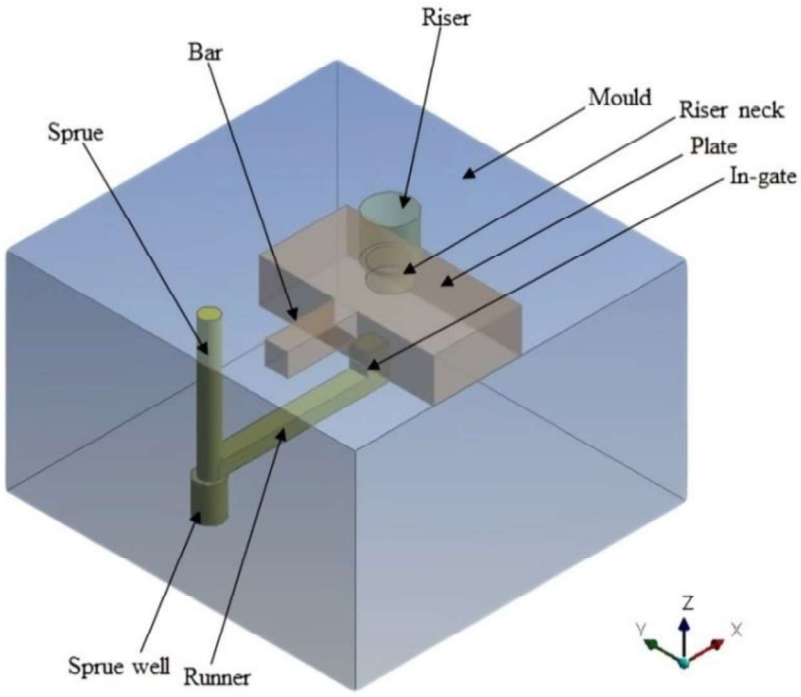

Figure 3.1: Bottom gating casting used by Mozammil et al. **[116]**.

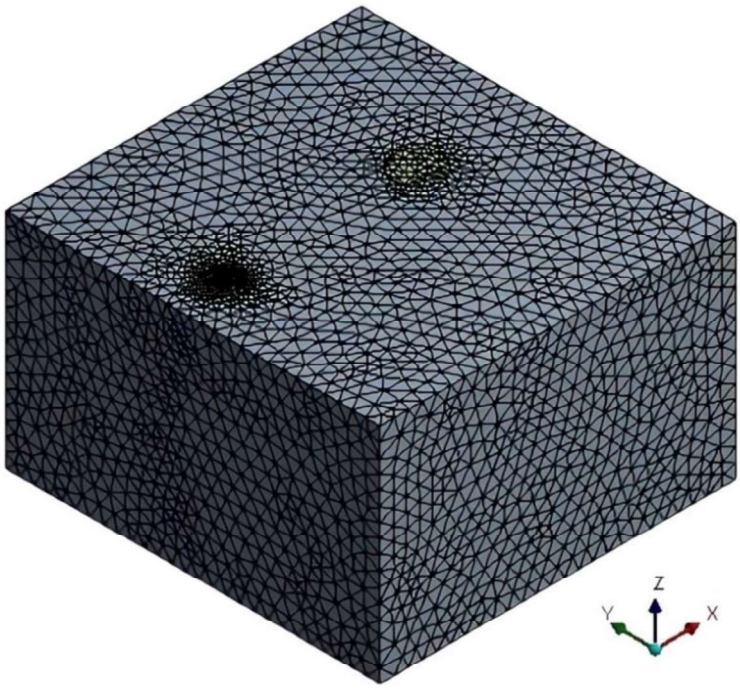

Figure 3.2: Mesh view of bottom gating casting.

In the present study, using our simulation model, the porosity values obtained were 0.0077, 0.0086, 0.0090, and 0.0094 at pouring temperatures of 970 K, 1000 K, 1050 K, and 1075 K, respectively. Based on the porosity values obtained from the present simulation results and the experimental results of Mozammil et al. [116]**,** it can be observed that there is a better agreement between the two. The simulation results show a close similarity to the experimental data, suggesting a strong correlation between the model utilized in the present study and the results obtained by Mozammil et al. [116]**.**

Table 3.1: Dimensions used in bottom gating casting **[116]**.

Name of the Components	**Name of the Parameters**	**Value (in mm)**
Diameter of sprue	Diameter	10
	Length	80
Sprue well	Diameter	15
	Height	20
Runner	Length	90
	Width	8
	Height	10
In-gate	Length	15
	Width	10
	Height	12
Riser	Diameter	25
	Height	25
Riser neck	Diameter	20
	Height	10

Table 3.2: Comparison of porosity results with pouring temperature using the current model.

Pouring Temperature (K)	**Experimental result of Porosity of Mozammil et al.** [116]	**Simulation result of Porosity of Mozammil et al.** [116]	**Porosity measured by our model**
970 K	0.0078	0.0073	0.0077
1000 K	0.0087	0.0076	0.0086
1050 K	0.0091	0.0082	0.0090
1075 K	0.0095	0.0085	0.0094

The present methods/model have been validated to closely resemble the practical scenario, thus a 60 mm × 60 mm × 10 mm pure aluminium casting with a steel mould has been selected for further analysis in this thesis.

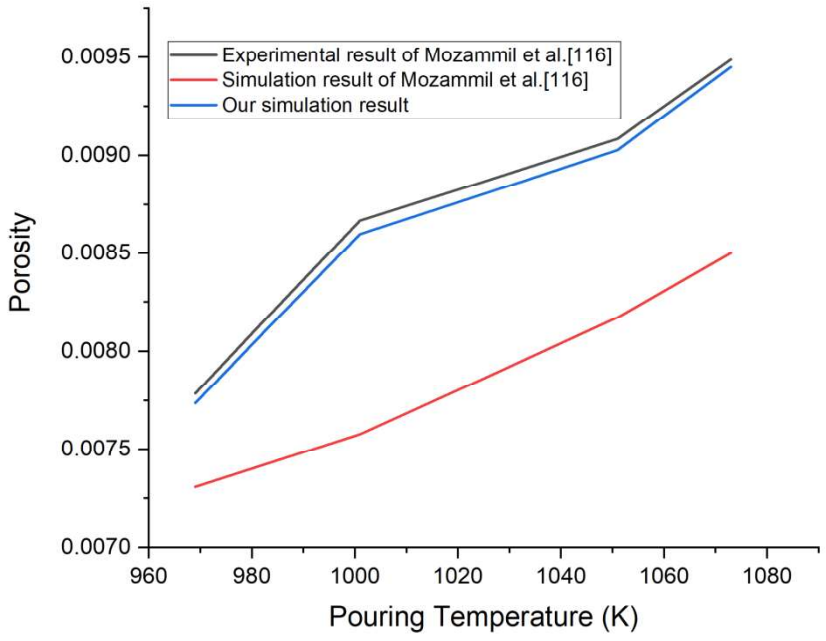

Figure 3.3: Comparative analysis of porosity vs pouring temperature with results of the current model.

3.4 Analysis of the Present Work

The total system of the casting-mould is shown in figure 3.4. Sprue, riser, mould, casting, and mould wall are illustrated in figure 3.4. A mould cavity or chamber that has been made for the casting where molten metal is poured and solidified.

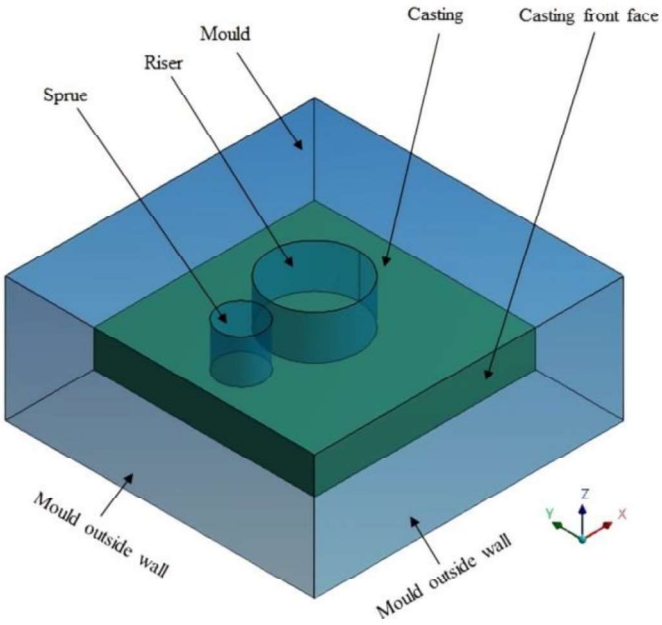

Figure 3.4: Three-dimensional representation of the mould and casting.

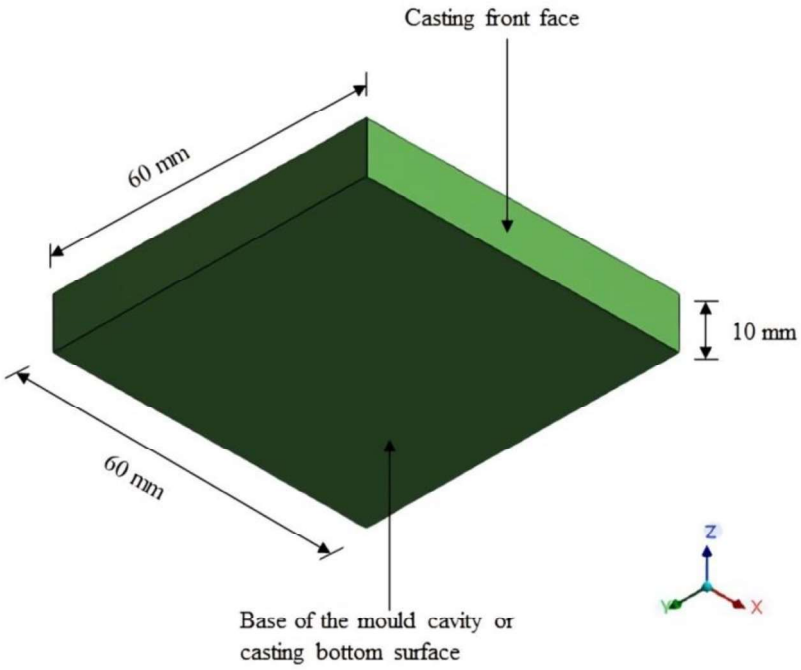

Figure 3.5: Dimensions of mould cavity or casting.

Figure 3.5 shows the mould cavity for the casting, with dimensions of 60 mm length, 60 mm breadth, and 10 mm depth. The different faces or surfaces and walls are shown in figure 3.4 and figure 3.5. Figures 3.6 and 3.7 depict the mesh view of the entire analysed system and the mesh view of the casting, riser, and sprue respectively.

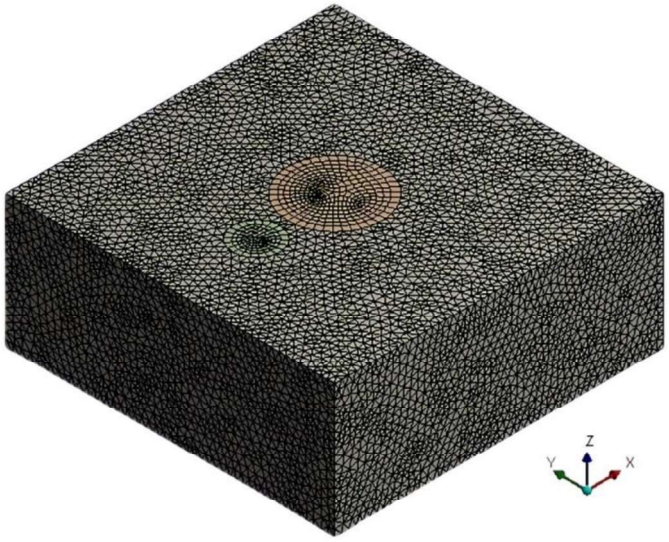

Figure 3.6: Mesh in the analysed system.

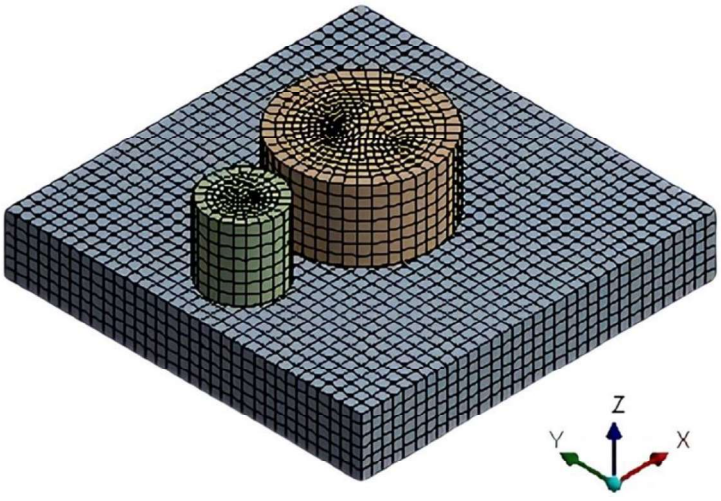

Figure 3.7: Mesh in the casting, riser, and sprue.

The mould is made of 1.5 percent carbon steel of dimension 84 mm × 84 mm × 34 mm. The thermophysical properties of aluminium, steel, and air are shown in table 3.3 [157, 197]. The

riser is placed in the middle of the casting so that it can feed equally in all directions of the casting. Riser design is important in casting processes as it serves as a reservoir of molten metal to compensate for the solidification shrinkage of the casting

3.4.1 Optimizing Riser Configuration and Mould Cavity Design

The shape and size of the riser are determined by Caine's method [155]. According to Caine's method, the time it takes for solidification to occur is directly proportional to the square of the ratio of volume to the surface area. To neglect shrinkage porosity it was taken into account that aluminium experiences a volumetric shrinkage of about 6.5% during solidification [155].

According to Caine's method [155, 198], the solidification time of casting or riser is related to the square of the ratio of its volume to surface area. This relationship can be expressed as

$$t_s = K_m(\frac{V}{A})^2 \tag{3.26}$$

Where t_s is the solidification time, V is the volume, A is the surface area, and K_m is the mould constant. In the context of riser design, the molten metal inside the riser serves to compensate for the volume reduction caused by shrinkage during solidification. As a result, the molten metal in the riser must solidify at a later stage than the molten metal in the casting cavity. However, using a large riser to achieve a longer solidification time is not practical due to the varying shrinkage characteristics of different metals. Therefore, it is important to choose the dimensions of the riser in a way that minimizes the A/V ratio while ensuring an adequate volume based on shrinkage considerations. It is important to note that the liquid metal flows from the riser into the mould only during the early part of the solidification process. As a result, the minimum volume of the riser should be approximately three times that dictated by shrinkage considerations alone, which can be calculated as Volume of riser [155] = 3 x shrinkage x volume of casting. To ensure that the solidification time in the riser is large, it is necessary to choose the dimensions of the riser carefully. The diameter/height ratio of the riser should be chosen in a way that minimizes the surface area for a given volume. The sphere might seem like a good option because it has a low

surface area-to-volume ratio, but it is challenging to feed because the hottest metal is located in its centre. Therefore, a cylindrical form is the second-best option and is mostly used.

The surface area of top riser (one surface is open to the atmosphere)

$$A_R = \pi D_r H_r + \frac{\pi}{4} {D_r}^2 \tag{3.27}$$

Where D_r is the diameter of the riser and H_r is the height of the riser

The volume of riser (V_r) is

$$V_r = \frac{\pi}{4} {D_r}^2 H_r \tag{3.28}$$

From the equation 3.28

$$H_r = \frac{4V_r}{\pi {D_r}^2} \tag{3.29}$$

Substitute the value of H_r into the equation 3.27

$$A_r = \frac{4V_r}{D_r} + \frac{\pi}{4} {D_r}^2 \tag{3.30}$$

For A_R to be minimum $\quad \frac{\partial A_r}{\partial D_r} = 0$

Or, $\quad \frac{-4V}{{D_r}^2} + \frac{\pi D_r}{2} = 0$

$$\text{Or, } {D_r}^3 = \frac{8V_r}{\pi} \tag{3.31}$$

Substitute the relation ${D_r}^3 = \frac{8V_r}{\pi}$ in the equation 3.29

$$H_r = \frac{D_r}{2} \tag{3.32}$$

As a result, the surface area of the riser would be minimized when the height-to-diameter ratio

of the riser was set to 1/2.

The dimensions of the cavity are ℓ mm in length, b mm in breadth, and d mm in depth.

Volume of the casting $V_c = \ell bd$ mm^3 (3.33)

Aluminium experiences a volumetric shrinkage of about 6.5% during solidification [155].

Therefore, volume of the riser, $V_r = 3 \times 0.065 \times V_c$ mm^3 (3.34)

The surface area of the casting can be calculated by excluding the area bottom surfaces of riser and sprue because of purpose of heat dissipation.

$$A_c = 2\ell b + 2bd + 2d\ell - \frac{\pi}{4}{D_{sp}}^2 - \frac{\pi}{4}{D_r}^2 \quad (3.35)$$

Where D_{sp} is the diameter of sprue and D_r is the diameter of riser

$$A_c = a_c - \frac{\pi}{4}{D_{sp}}^2 - \frac{\pi}{4}{D_r}^2 \quad (3.36)$$

Assume $a_c = 2\ell b + 2bd + 2d\ell$

The riser is designed to solidify last, we need $(\frac{A}{V})_r \leq (\frac{A}{V})_c$

Or, $$\frac{6}{D_r} \leq \frac{a_c - \frac{\pi}{4}{D_{sp}}^2 - \frac{\pi}{4}{D_r}^2}{V_C}$$

Or, $$a_c D_r - \frac{\pi}{4} D_r {D_{sp}}^2 - \frac{\pi}{4}{D_r}^3 \leq 6V_c$$

Or, $$\frac{\pi}{4}{D_r}^3 - a_c D_r + \frac{\pi}{4} D_r {D_{sp}}^2 \geq -6V_c$$

Or, $$\frac{\pi}{4}{D_r}^3 - D_R\left(\frac{\pi}{4}{D_{sp}}^2 - a_c\right) + 6V_c \geq 0$$

Or,

$$D_r{}^3 + D_r\left(D_{sp}{}^2 - \frac{4}{\pi}a_c\right) + \frac{24}{\pi}V_c \geq 0$$

Or,

$$\frac{6}{D_r} \leq \frac{a_c - \frac{\pi}{4}D_{sp}{}^2 - \frac{\pi}{4}D_r{}^2}{V_c} \tag{3.37}$$

Equation (3.37) can be used to compute the diameter of the riser.

The dimensions of the cavity are 60 mm in length (ℓ), 60 mm in breadth (b), and 10 mm in depth (d). Therefore, by applying equation 3.33 and equation 3.34, the values of V_C (volume of the casting) and V_R (volume of the riser) can be determined.

Volume of the casting $V_c = \ell bd$ =60 x 60 x 10= 36000 mm^3

Volume of the riser, V_r= 3 x 0.065 x V_c =7020 mm^3

The diameter of the sprue (D_{sp}) is taken to be 12 mm.

By using the trial and error method to calculate equation 3.37, it is determined that the diameter of the riser (D_r) is equal to 24 mm.

According to equation 3.32, the height of the riser (H_r) is determined to be 12 mm.

Figure 3.8 provides a representation of the dimensions of the mould cavity for casting, as well as the dimensions and position of the sprue and riser. The riser is positioned at the centre of the cavity to allow for equal feeding in every direction [53, 62]. This ensures that the molten material can distribute evenly throughout the casting.

3.4.2 Pouring Time

Pouring time is measured as the ratio between the total volume (mould cavity, sprue, and riser) and the volume of molten metal entering per unit time through the inlet [53, 199].

Total Cavity volume (V) = volume of the sprue+ volume of the riser+ casting volume

$$=\frac{\pi}{4}D_{sp}{}^{2}H_{sp}+\frac{\pi}{4}D_{r}{}^{2}H_{r}+\ell bd$$

$$=\frac{\pi}{4}12^{2}x12+\frac{\pi}{4}24^{2}x12+60x60x10$$

=1356.48+5425.92+36000

=42782.4 mm^3

At inlet of the sprue,

$$\frac{\pi}{4}D_{sp}{}^{2}v_{p}t_{p}=V \tag{3.38}$$

Where, pouring velocity= v_p, and t_p =pouring time.

Therefore, pouring time (t_p) is given by,

$$t_{p}=\frac{4V}{\pi D_{sp}{}^{2}v_{p}} \tag{3.38}$$

Five different pouring velocities of 380 mm/s, 415 mm/s, 450 mm/s, 485 mm/s, and 520 mm/s were used, resulting in calculated pouring times of 1 s, 1 s, 0.9 s, 0.8 s, and 0.8 s respectively. Some pouring times are the same due to rounding to the nearest number.

The Reynolds number at inlet of the sprue [200],

$$Re=\frac{\rho v_{p}D_{sp}}{\mu}$$

The Reynolds number is greater than 2000 for all pouring velocities at inlet of the sprue, indicating that the flow inside the mould cavity is turbulent.

3.4.3 Initial and Boundary Conditions

Initially, the mould cavity, riser, and sprue are filled with air at atmospheric temperature. The temperature of the analysed system at the beginning is equal to the atmospheric temperature, which is 30°C. When mould is preheated, initially this temperature will be preheating temperature. During the filling process, the molten metal enters the mould cavity through the sprue inlet. At the inlet zone, velocity is the same as the pouring velocity of molten metal, and temperature is equal to the pouring temperature of molten metal. The primary and

secondary phases in this two-phase system are air and aluminium, respectively. During the pouring process, the air is allowed to leave through the riser outlet. A pressure outlet boundary condition is imposed at the outlet zone where ambient air pressure is specified. Six outside boundary surface walls of the mould are exposed to the atmosphere, where natural convection occurs. The convection heat transfer coefficients are calculated by taking air properties [197] (thermal conductivity, kinematic viscosity, and Prandtl number) at mean film temperature to determine the natural convection between the mould surface wall and atmospheric air.

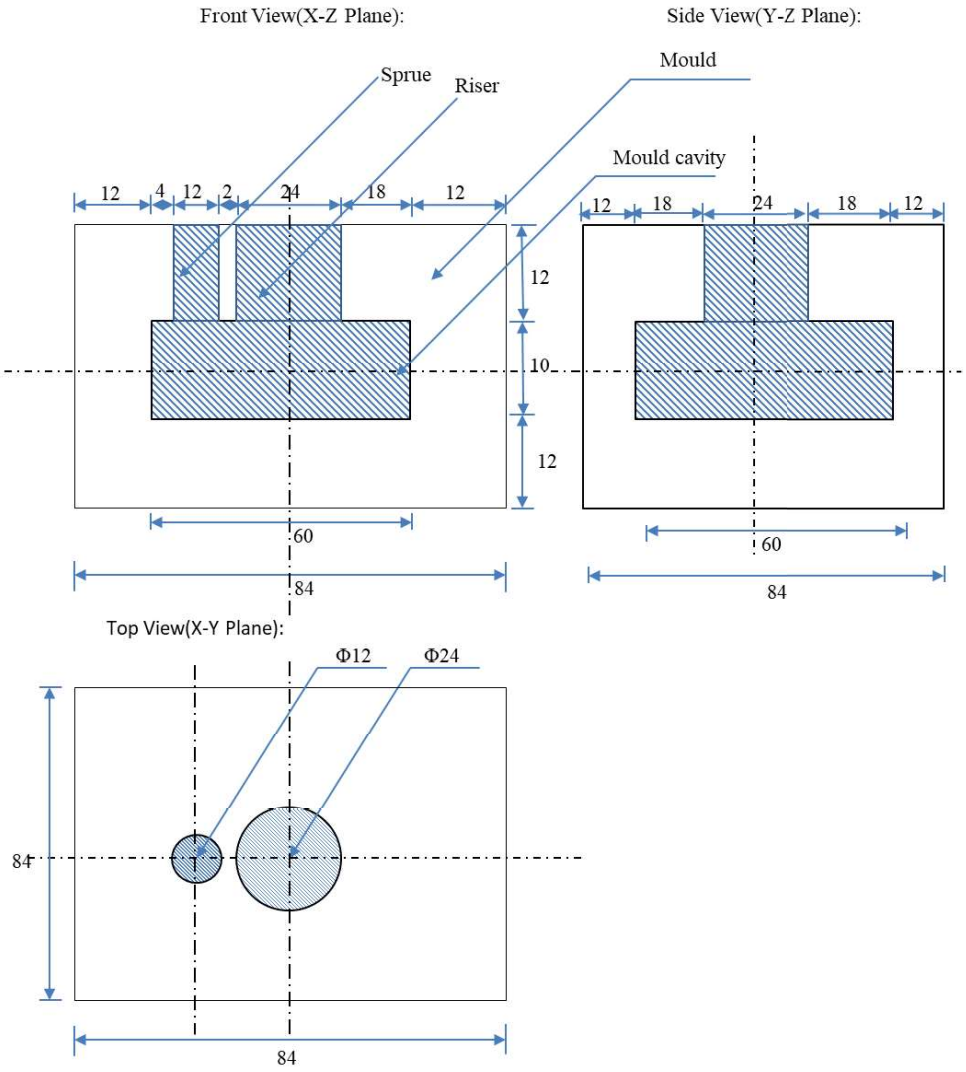

Figure 3.8: Casting dimension with sprue and riser in mm.

Table 3.3: Thermo-physical properties of the aluminium, air, and steel used in the simulations.

Name	Property	Value	Unit
Aluminium	Thermal conductivity (liquid)	100	W/m K
	Thermal conductivity (solid)	200	W/m K
	Specific heat (liquid)	1200	J/kg K
	Specific heat (solid)	1060	J/kg K
	Density	2690	kg/m^3
	Viscosity	0.001	kg/m s
	Freezing Temperature	933	K
	Latent heat of solidification	391	kJ/kg
Air	Thermal conductivity	0.0336	W/m K
	Specific heat	1014	J/kg K
	Density	0.8826	kg/m^3
	Viscosity	2.286e-05	kg/m s
Steel	Thermal conductivity	33	W/m K
	Specific heat	486	J/kg K
	Density	7753	kg/m^3

3.4.3.1 Calculation of Heat Transfer Coefficient

For different Rayleigh number (Ra) ranges, the convection heat transfer coefficient calculation formula has been applied [197].

The Rayleigh number is given by,

$$Ra = \frac{g\delta_a {L_o}^3 {\rho_a}^2 \Delta T Pr_a}{{\gamma_a}^2}$$

Where ΔT denotes the difference in temperature between the casting surface and atmosphere, γ_a is the kinematic viscosity of air [m^2/s], L_o is the length of the outside wall surface of the mould

[m], δ_a is the volumetric coefficient of thermal expansion of air [K^{-1}], and Pr_a is the Prandtl number of air.

The convection heat transfer coefficient (denoted by h_c) [W/m^2 K] for different types of surface geometry is calculated by the equations given below.

For vertical surfaces,

$$h_c = \begin{matrix} 1.42\left(\frac{\Delta T}{L_o}\right)^{1/4}, where\ 10^4 < \text{Ra} \leq 10^9 \\ 1.31(\Delta T)^{1/3}, where\ 10^9 < \text{Ra} \leq 10^{13} \end{matrix}$$

For upper-heated horizontal surfaces,

$$h_c = \begin{matrix} 1.32\left(\frac{\Delta T}{L_o}\right)^{1/4}, where\ 10^5 < \text{Ra} \leq 2\text{x}10^7 \\ 1.52(\Delta T)^{1/3}, where\ 2\text{x}10^7 < \text{Ra} \leq 3\text{x}10^{10} \end{matrix}$$

For lower-heated horizontal surfaces,

$$h_c = 0.59\left(\frac{\Delta T}{L_o}\right)^{1/4}, where\ 3\text{x}10^5 < \text{Ra} \leq 3\text{x}10^{10}$$

The process of calculating the average heat transfer coefficients involves the following steps:

(i) Set the atmospheric temperature, T_a=30 °C.

(ii) Select different wall surface temperatures, such as 50, 100, 200, 300, 400, 500, 600, and 700°C.

(iii) Calculate the mean film temperature (T_F) using the formula $T_F = (T_S + T_a)/2$, where T_S is the wall surface temperature.

(iv) Determine the Rayleigh Number at the mean film temperature by considering the properties of air at the same temperature.

(v) Use the corresponding formula to calculate the heat transfer coefficient.

(vi) Repeat the above steps for each wall surface temperature and calculate average heat transfer coefficient between mould outside wall and atmospheric air.

To facilitate the calculations, a computer program written in FORTRAN 95 has been developed. This program allows for the calculation of the average heat transfer coefficient for various wall surface temperatures starting from T_a.

The average heat transfer coefficient for the upper horizontal mould wall (where riser and sprue open) is 10.05 W/m^2 K, for the lower horizontal mould wall (opposite to upper horizontal mould wall) is 4.49 W/m² K, and for the vertical walls is 13.55 W/m² K.

3.4.4 Mesh and Mesh Sensitivity Analysis

The mesh quality influences the convergence and accuracy of the CFD solution. The mesh has been constructed using Ansys-Fluent simulation software. The fine mesh was used in this study to get high accuracy and convergence of the CFD solution

The mesh sensitivity analysis has been studied. Three types of mesh or grid were chosen: coarse, medium, and fine of their mesh number 19764, 50956, and 130276 for the analysis of mesh sensitivity. The coarse, medium, and fine grids are identified by the notations 1, 2, and 3 respectively. The aluminium volume fraction was measured after 0.4 s for coarse, medium, and fine mesh structures at 983 K pouring temperature and 380 mm/s poring velocity. The values obtained are 0.3163, 0.3364, and 0.3388, respectively. These values are represented as f_1, f_2, and f_3 respectively. The grid convergence index (GCI) has been calculated using Richardson extrapolation methods and is an excellent indicator of discretization uncertainty [169]. The steps for investigating grid convergence are as follows [201].

The order of convergence, *oc*, is determined by the following equation:

$$oc = \ln\frac{(f_1 - f_2)}{(f_2 - f_3)} / \ln g_r$$

Where g_r is the grid refinement ratio which is the ratio of the numbers of mesh between two grids. The calculated value of the grid refinement ratio is 2.56.

The relative error (e) between two grids is calculated as

$$e_{1,2} = \left|\frac{f_2 - f_1}{f_2}\right|$$
$$e_{2,3} = \left|\frac{f_3 - f_2}{f_3}\right|$$

The calculated value of relative error for grids 1 and 2 ($e_{1,2}$) is 0.0598 and for grids 2 and 3 ($e_{2,3}$) is 0.0071. The relative error is very small for grids 2 and 3. It is evident that a mesh value of 50956 cells or higher will provide a solution that is independent of the mesh size. All of the predicted results in this thesis have been obtained using a fine mesh.

The following equation is used to calculate the grid convergence index:

$$GCI = \frac{1.25|e|}{{g_r}^{oc} - 1}$$

The grid convergence index for grids 1 and 2 ($GCI_{1,2}$) is 0.0101and for grids 2 and 3 ($GCI_{2,3}$) is 0.0012. The error is 0.0012 or 0.12% for the discretization solution.

It is also important to check whether the solutions are within the asymptotic range of convergence. This can be checked using the following relationship:

$$\frac{GCI_{1,2}}{{g_r}^{oc} GCI_{2,3}} \cong 1$$

The value of the left-hand side of the relationship is 1.0071, which is close to one and implies that the solutions are well in the asymptotic range of convergence.

3.5 Results and Discussion

In this analysis, the pouring velocity, pouring temperature, and mould initial temperature are varied. At first, the mould temperature is set at 30°C (303 K). Then the analysis is extended to include mould initial or preheated temperatures of 130°C (403 K) and 230°C (503 K).

In order to simulate the process, five pouring velocities (in mm/s) have been used: 380, 415, 450, 485, and 520. The aluminium metal is poured into the mould at three different temperatures: 983 K, 1003 K, and 1033 K. These temperatures are above the melting point of aluminium metal, which is 933 K. The first pouring temperature has a superheat of 50, the second has a superheat of 70, and the third has a superheat of 100. Therefore, simulations are

carried out for fifteen cases by varying each pouring velocity with different pouring temperatures. These fifteen cases are analysed for each mould temperature. So, a total of forty-five cases have been studied.

3.5.1 Solidification and Mould Filling Process

The middle plane in the casting is taken to represent the filling and solidification process. The middle plane is located on the z-x axis, 30 mm away from the casting's front face along the y-axis as shown in figures 3.4 and 3.5.

3.5.1.1 Casting with Mould Initial Temperature 30°C (303 K)

Initially, the solidification and mould filling process is explained for a pouring temperature of 983 K and a pouring velocity of 380 mm/s, as depicted in figure 3.9. After that, the solidification and mould filling process is described for various pouring velocities and temperatures.

Solidification and Mould Filling Process at Pouring Velocity of 380 mm/s and a Pouring Temperature of 983 K:

Figure 3.9 shows the solidification and filling process at various times.

(i) At 0 s the mould cavity is filled by air at ambient temperature. Liquid aluminium enters the mould cavity from the sprue outlet boundary at 0.1 s as shown in figure 3.9a. The air mixes with liquid aluminium metal and forms a liquid aluminium -air layer due to the high solubility of air in molten liquid at a higher temperature. The liquid aluminium is surrounded by a liquid aluminium-air mixture layer. At first, the liquid aluminium-air layer comes in contact with the bottom of the mould cavity as shown in figure 3.9a.

(ii) After 0.1 s, the molten aluminium makes contact with the cavity's bottom and left side wall as indicated in figure 3.9b. Some liquid aluminium solidifies at the left side wall of the cavity, producing a liquid-solid aluminium mixture. Simultaneously liquid aluminium moves to the cavity's right side. The air is displaced as liquid aluminium filled the area. Instead of quick solidification of liquid aluminium in air, liquid aluminium -air layer is formed around the flow of liquid aluminium. It is because the

rate of heat transfer between the liquid aluminium and the air through advection is relatively slow.

(iii) Around 0.25 s, the liquid aluminium starts to solidify. Before complete solidification, an intermediate phase liquid-solid aluminium mixture forms (figure 3.9b and figure 3.9c). Liquid aluminium metal continues to flow smoothly into the mould cavity (figure 3.9c). As molten metal travels, the liquid-solid aluminium mixture layer and liquid aluminium -air layer shift to the right of the cavity.

(iv) Liquid metal commences flowing back from the right wall of the mould cavity. The bottom of the cavity is filled with aluminium metal at around 0.75 s as shown in figure 3.9d. Some liquid metal solidifies from the liquid-solid aluminium mixture near the bottom right corner, where liquid metal begins to flow back.

(v) Pouring is done up to 1 s. Most of the aluminium metal is present in liquid form at this moment, particularly below the sprue as shown in figure 3.9e. Solidification of aluminium gradually increases with time. When liquid metal reaches the right side of the cavity after traveling some distance it loses flowing velocity due to the resistance offered by the mould material. Therefore, initially solidification mainly occurs at this right side of the cavity. A porous solidified area (solid aluminium-air mixture) is formed upon the solidified aluminium metal. All phases such as liquid aluminium, liquid-solid aluminium mixture, solid aluminium, liquid aluminium-air mixture, solid aluminium-air mixture, and air are present at this time as shown in figure 3.9e.

(vi) As seen in figure 3.9f, the depth of aluminium solidified metal is higher at the right and left walls and low in the middle. The riser is placed at the centre of the cavity. Some molten aluminium is present in liquid form in the middle of the cavity below the riser. A liquid aluminium-air mixture layer is also formed below the riser. The porous solidified area (solid aluminium-air mixture) is mainly formed at the upper right portion of the cavity. All phases are present at this time as shown in figure 3.9f.

While pouring, there is a formation of a mixture of liquid and solid aluminium at the left wall due to heat exchange with the wall. This mixture is then disrupted by the

continuous pouring of high-temperature molten metal, which continues until the 1s time. Subsequently, at 1.5 s into the process, it is seen that a solid layer of aluminium has been developed at this wall. This solidification is a result of heat exchange between the material and the wall.

(vii) All aluminium liquid metal solidifies about 2 s (figure 3.9g). The temperature is below 933 K everywhere in the casting. Solid aluminium is formed on the lower side of the cavity. The upper side of the cavity has a solid aluminium-air mixture layer.

(viii) Thus, two layers form in the cavity, one of solid aluminium and the other of the solid aluminium-air mixture. Upon cooling, the layers get small displaced due to volume contraction in the solid metal as shown in figure 3.9h. The cooling is shown up to 10.84 s. After about 2 s, no effective change happens in the solidified casting as shown in figures 3.9g, 3.9h, and 3.9i.

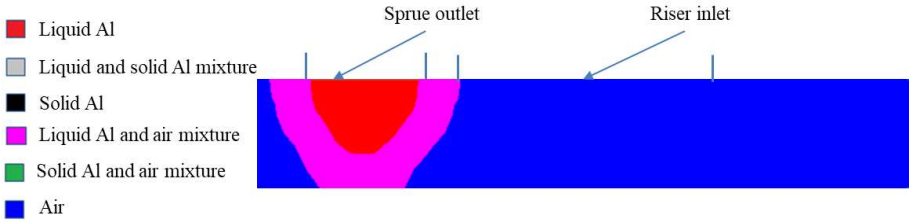

Figure 3.9a: Time 0.1 s

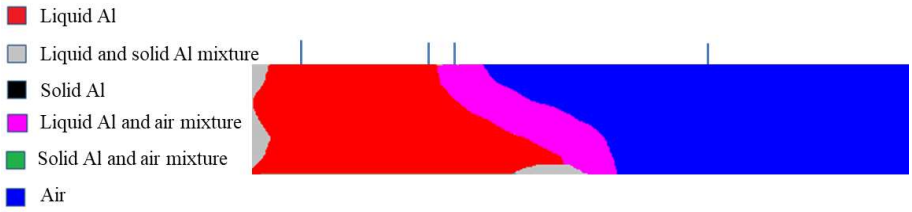

Figure 3.9b: Time 0.25 s

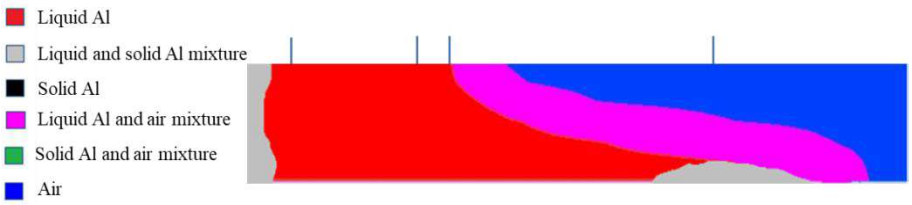

Figure 3.9c: Time 0.5 s

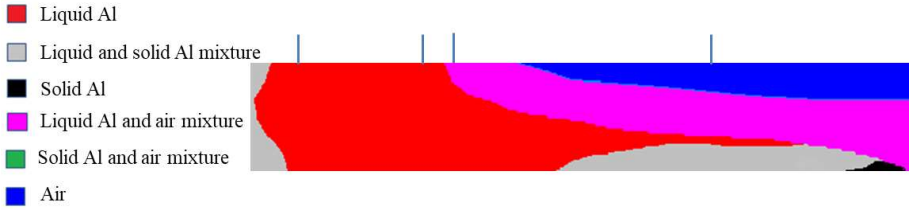

Figure 3.9d: Time 0.75 s

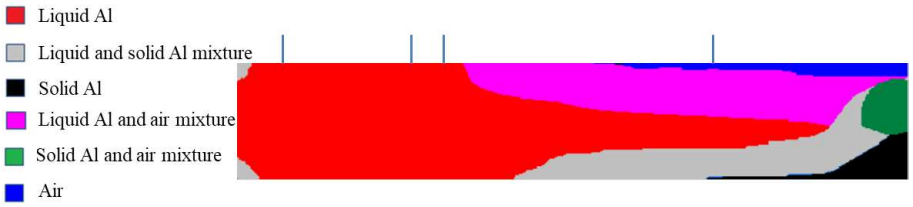

Figure 3.9e: Time 1 s

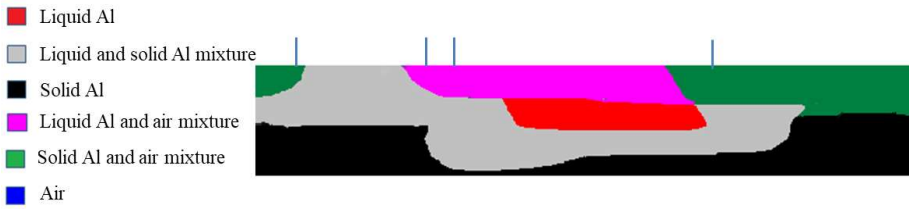

Figure 3.9f: Time 1.5 s

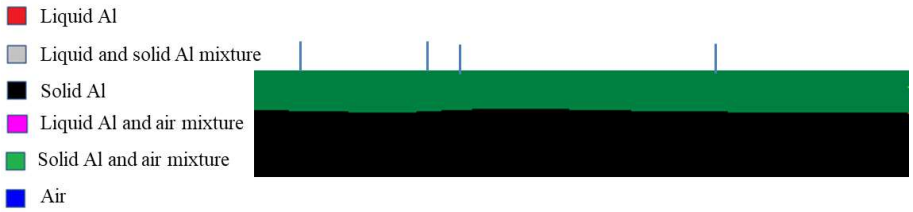

Figure 3.9g: Time 2 s

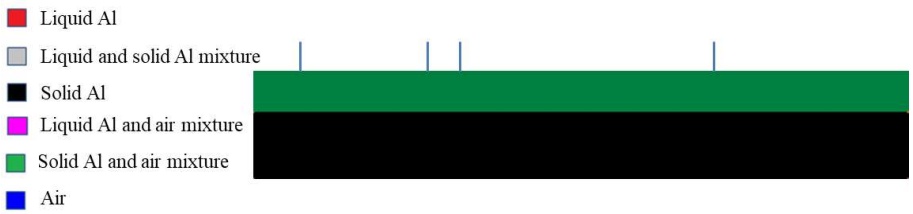

Figure 3.9h: Time 10.84 s

Figure 3.9: Simulation of the solidification and mould filling process with parameters v_p=380 mm/s, T_p=983 K, and T_0=303 K.

Comparative Analysis of Solidification Process for Various Pouring Velocities and Temperatures:

The solidification and free surface of the filling process for all pouring velocities and pouring temperatures are represented at different times which are shown in figure 3.10. The solidification front has been represented for 0.1 s, 0.5 s, 1 s, 1.5 s, and at the end of solidification for all pouring velocities and pouring temperatures. The solidification front moves in a specific direction, rather than uniformly across the entire casting. This occurs because of temperature gradients that develop within the casting during solidification, and the direction of solidification is typically determined by the shape of the mould and the position of the riser.

Liquid aluminium enters the mould cavity from the sprue outlet boundary at 0.1 s. After 0.1 s, the molten aluminium makes contact with the cavity's bottom and left side wall as indicated. Some liquid aluminium solidifies at the left side wall of the cavity, producing a liquid-solid aluminium mixture. Simultaneously liquid aluminium moves to the cavity's right side. The air is displaced as liquid aluminium filled the area. Initially, a liquid aluminium-air layer is formed around the flow of liquid aluminium instead of quick solidification of liquid aluminium in air. It is because the rate of heat transfer between the liquid aluminium and the air through advection is significantly low. Around 0.5 s, the liquid aluminium starts to solidify. Before complete solidification, an intermediate phase liquid-solid aluminium mixture forms. Liquid aluminium metal continues to flow smoothly into the mould cavity. As molten metal travels, the liquid-solid aluminium mixture layer and liquid aluminium-air layer shift to the right of the cavity. At 450 mm/s and 520 mm/s velocity some metal has been solidified and create solid aluminium and

air mixture, and solid aluminium at different pouring temperatures. This is because, when the pouring velocity is high, the molten metal enters the mould cavity more quickly, causing the metal to come into contact with the mould surface at a higher velocity. This increased velocity can result in increased turbulence and movement of the metal, which in turn can increase the rate of heat transfer between the metal and the mould surface.

At 1 s, most of the aluminium metal is present in liquid form at this moment, particularly below the sprue as shown in figure 3.10. Solidification of aluminium gradually increases with time. When liquid metal reaches the right side of the cavity after traveling some distance it loses flowing velocity due to the resistance offered by the mould material. Therefore, initially solidification mainly occurs at this right side of the cavity. A porous solidified area (solid aluminium-air mixture) is formed upon the solidified aluminium metal. Almost all phases such as liquid aluminium, liquid-solid aluminium mixture, solid aluminium, liquid aluminium-air mixture, solid aluminium-air mixture, and air are present at different pouring parameters at this time.

At 1.5 s the solidification process continue in the mould cavity. The depth of aluminium solidified metal is higher at the right and left walls and low in the middle below the riser. Some molten aluminium is present in liquid form in the middle of the cavity below the riser. This is because the walls of the mould act as a heat sink and draw heat away from the molten metal more quickly than the centre, causing the solidification more rapidly at the walls. The riser also acts as a heat source, which can cause the metal in that area to solidify more slowly.

A liquid aluminium-air mixture layer is also formed below the riser from 380-450 mm/s velocity. When the entrained air reaches the bottom of the riser, it can become trapped and form a layer of liquid aluminium-air mixture. At 520 mm/s velocity, the liquid aluminium-air mixture layer below the riser is not formed. This is because all metal is filled in the mould cavity at 520 mm/s at this time.

At the end of solidification, the whole liquid metal is solidified. At 520 mm/s velocity the mould cavity is fully filled by the solidified metal. The porous solidified area (solid aluminium-air mixture) is formed at 380-450 mm/s velocity at the upper right portion of the cavity.

Pouring velocity, Pouring temperature	0.1 s	0.5 s	1 s	1.5 s	End of solidification
380 mm/s, 983 K					
380 mm/s, 1003 K					
380 mm/s, 1033 K					
450 mm/s, 983 K		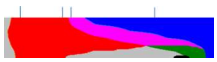			
450 mm/s, 1003 K				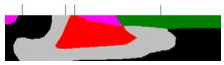	

Pouring velocity, Pouring temperature	0.1 s	0.5 s	1 s	1.5 s	End of solidification
450 mm/s, 1033 K		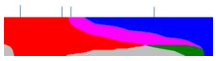			
520 mm/s, 983 K					
520 mm/s, 1003 K					
520 mm/s, 1033 K					

Liquid Al
Liquid and solid Al mixture
Solid Al
Liquid Al and air mixture
Solid Al and air mixture
Air

Figure 3.10: Solidification analysis for various pouring velocities and temperatures at a mould temperature of 303 K.

3.5.1.2. Casting with Mould Initial Temperature 130°C (403 K)

Solidification and Mould Filling Process at Pouring Velocity of 380 mm/s and a Pouring Temperature of 983 K:

Figure 3.11 shows the solidification and filling process at various times. At 0.1 s, liquid aluminium enters the mould cavity through the sprue outlet boundary and makes contact with the bottom wall. The preheated mould at 403 K enhances the fluidity of the molten metal, allowing it to travel a greater distance compared to a non-preheated mould. Instead of immediate solidification in air, a liquid aluminium-air layer forms around the flow of liquid aluminium. At 0.5 s, a mixture of liquid and solid aluminium starts forming on the bottom wall, and the flow of liquid aluminium continues smoothly into the cavity. Between 0.5 s and 0.75 s, some air is trapped within the solid aluminium at the right side of the wall and air leaves from solid aluminium as mould filling progresses (figure 3.11d). The liquid-solid aluminium mixture layer and liquid aluminium-air layer shift towards the right side of the cavity as the molten metal travels. With a mould initial temperature of 403 K, the bottom of the cavity is filled with liquid aluminium around 0.5 s, while it takes until around 0.75 s for a mould with a 303 K initial temperature. Some solidification occurs near the bottom right corner where the liquid metal starts to flow back. As the liquid metal reaches the right side of the cavity and loses velocity, solidification primarily occurs there initially. Pouring is completed by 1 s, and most of the aluminium remains in liquid form. After 1 s, solidification gradually increases, resulting in deeper solidified metal at the right and left walls and less in the middle. Some molten aluminium remains in liquid form below the riser in the middle of the cavity. The amount of molten aluminium in liquid form is more for high preheating temperature and decreases with decreasing mould preheating temperature at a time. At 2.2 s, air is present with the liquid aluminium below the riser. After solidification, a solid aluminium-air mixture layer forms below the riser (figure 3.11g).

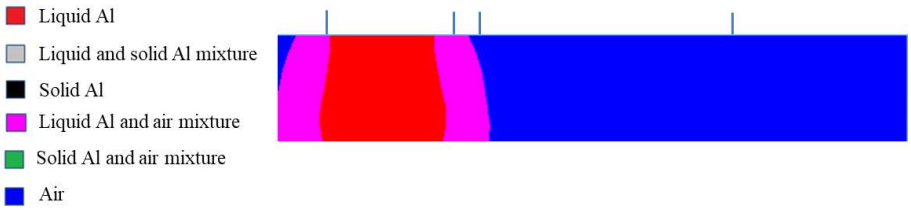

Figure 3.11a: Time=0.1 s

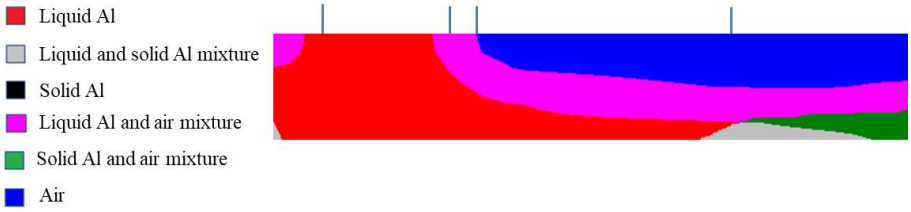

Figure 3.11b: Time=0.5 s

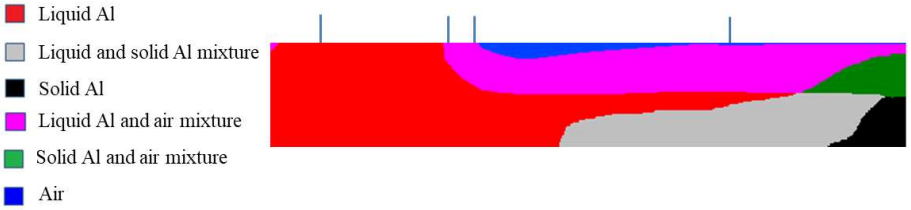

Figure 3.11c: Time=0.75 s

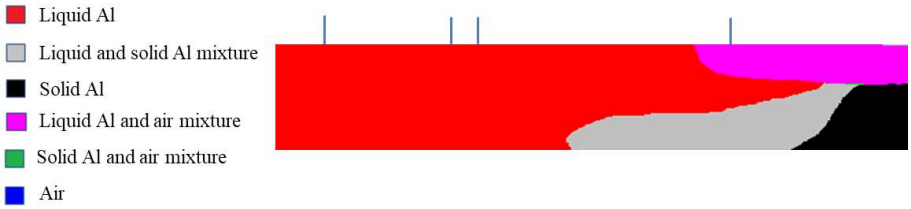

Figure 3.11d: Time=1 s

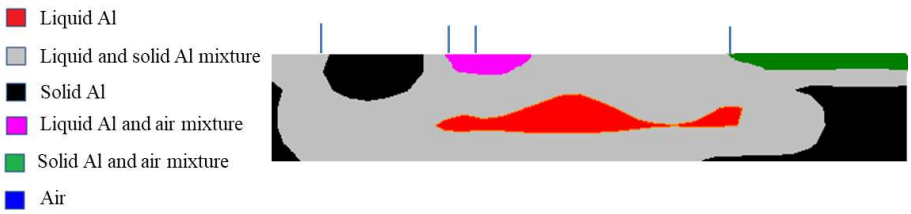

Figure 3.11e: Time=1.5 s

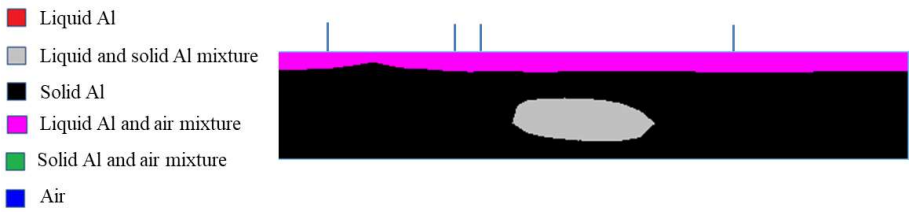

Figure3.11f: Time=2.2 s

Figure3.11g: Time=10 s

Figure 3.11: Simulation of the solidification and mould filling process with parameters v_p=380 mm/s, T_p=983 K, and T_0=403 K.

Comparative analysis of Solidification Process for Various Pouring Velocities and Temperature:

Figure 3.12 illustrates the solidification and free surface of the filling process at various times for different pouring velocities and temperatures. The solidification front is depicted at 0.1 s, 0.5 s, 1 s, 1.5 s, and at the end of solidification for all pouring conditions. After 0.1 s, the molten aluminium makes contact with the cavity's bottom and left side wall as indicated. Simultaneously liquid aluminium moves to the cavity's right side. The air is displaced as liquid aluminium filled the area. A liquid aluminium-air layer is formed initially around the flow of liquid aluminium. Around 0.5 s, the liquid aluminium reached the left side of mould cavity and starts to solidify. As molten metal travels, the liquid-solid aluminium mixture layer and liquid aluminium -air layer shift to the right of the cavity. Higher pouring velocity results in faster metal entry into the mould cavity, increasing the metal solidification rate due to enhanced heat transfer resulting from increased turbulence.

After 1 s, most of the aluminium metal is present in liquid form at this moment, particularly below the sprue as shown in figure 3.12. Initially, solidification mainly occurs at this right side of the cavity. Solidification of aluminium gradually increases with time. When the molten metal enters the mould cavity and travels towards the right side, its flowing velocity decreases due to the resistance offered by the mould material. A porous solidified area (solid aluminium-air mixture) is formed upon the solidified aluminium metal. Almost all phases such as liquid aluminium, liquid-solid aluminium mixture, solid aluminium, liquid aluminium-air mixture, solid aluminium-air mixture, and air are present at different cases at this time. When pouring velocity increases, the metal filling also increases. Thus a more amount of liquid reaches to the right side of the cavity than low pouring velocity.

At 1.5 s the solidification process continue in the mould cavity. The depth of aluminium solidified metal is higher at the right and left walls and low in the middle below the riser. Some molten aluminium is present in liquid form in the middle of the cavity below the riser. A liquid aluminium-air mixture layer is also formed below the riser at all pouring velocities. At the end of solidification, the liquid aluminium-air mixture layer is not found as the air escapes from the metal through riser.

Pouring velocity, Pouring temperature	0.1 s	0.5 s	1 s	1.5 s	End of solidification
380 mm/s, 983 K				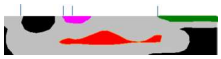	
380 mm/s, 1003 K					
380 mm/s, 1033 K				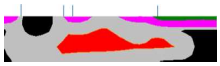	
450 mm/s, 983 K					
450 mm/s, 1003 K					

Pouring velocity, Pouring temperature	0.1 s	0.5 s	1 s	1.5 s	End of solidification
450 mm/s, 1033 K					
520 mm/s, 983 K					
520 mm/s, 1003 K					
520 mm/s, 1033 K					

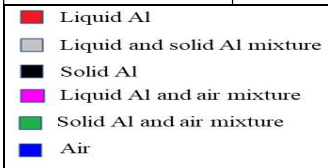

Figure 3.12: Solidification analysis for various pouring velocities and temperatures at a mould temperature of 403 K.

3.5.1.3. Casting with Mould Initial Temperature 230°C (503 K)

Solidification and Mould Filling Process at Pouring Velocity of 380 mm/s and a Pouring Temperature of 983 K.

Figure 3.13 shows the solidification and filling process at various times. At 0.1 s, liquid aluminium enters the mould cavity from the sprue outlet boundary and makes contact with the cavity's bottom and left side wall. Because molten metal removes energy to the wall, liquid aluminium solidifies at the wall of the cavity. The fluidity of molten metal has been increased as the mould is preheated to 503 K, so molten metal travel more path at any time than no preheat mould temperature and 303 K preheated mould temperature. At around 0.4s, liquid aluminium moves to the cavity's right side. Liquid aluminium -air layer is formed around the flow of liquid aluminium. A liquid-solid aluminium mixture phase is formed on the right side wall of the cavity. Liquid aluminium metal continues to flow smoothly into the cavity. As molten metal travels, the liquid-solid aluminium mixture layer and liquid aluminium -air layer shift to the right of the cavity. The bottom of the cavity is filled with aluminium metal before 0.4 s for mould initial temperature 503 K. However, for a mould with an initial temperature of 303 K, the bottom of the cavity is filled with liquid aluminium at around 0.75 s. In the case of a mould with a preheating temperature of 403 K, the bottom of the cavity is filled with liquid aluminium at around 0.4 s. At 0.4 s to 0.5 s, some air is trapped at the right side of the wall within the solid aluminium. Some metal solidifies near the bottom right corner, where liquid metal begins to flow back. When liquid metal reaches the right side of the cavity after traveling some distance it loses flowing velocity. Initially, solidification mainly occurs at this right side of the cavity. Pouring is done up to 1 s. After 1.5 s, the depth of aluminium solidified metal is higher at the right and left walls and low in the middle. Solidification of aluminium gradually increases with time. At 2.2 s, a small amount of molten aluminium is present in liquid form in the middle of the cavity below the riser. A liquid-solid aluminium mixture layer is formed below the riser at 3.2 s. All the liquid metal has solidified after 3.2 s as shown in figure 3.13i.

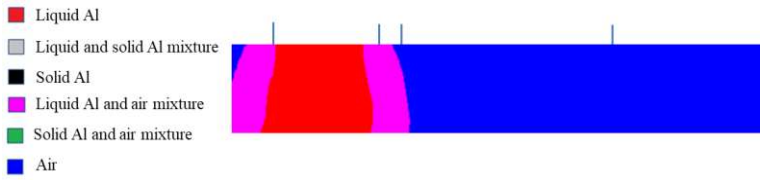

Figure 3.13a: 0.1 s

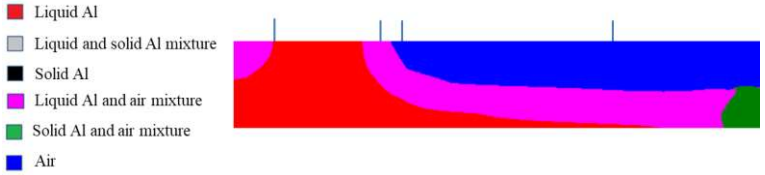

Figure3.13b: 0.4 s

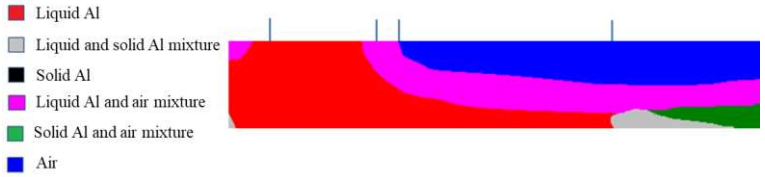

Figure 3.13c:0.5 s

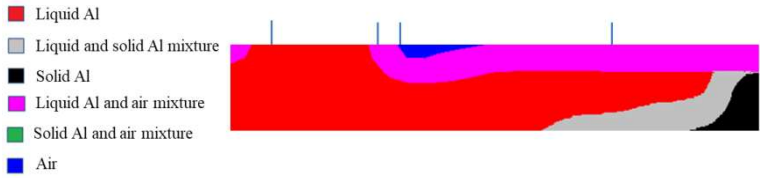

Figure 3.13d: 0.8 s

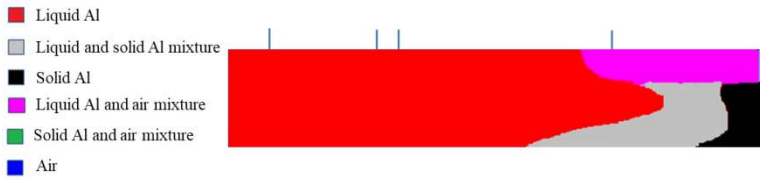

Figure 3.13e: 1 s

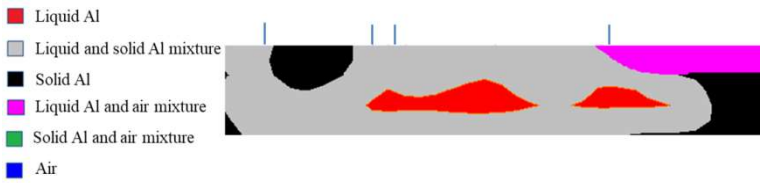

Figure 3.13f: 1.5 s

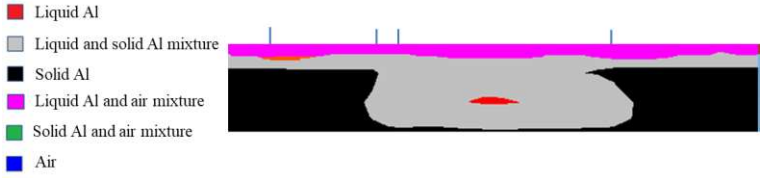

Figure 3.13g: 2.2 s

Figure 3.13h: 3.2 s

Figure 3.13i: 10 s

Figure 3.13: Simulation of the solidification and mould filling process with parameters v_p=380 mm/s, T_p=983 K, and T_0=503 K.

Comparative analysis of solidification process for Various Pouring Velocities and Temperatures:

The solidification and free surface of the filling process for all pouring velocities and pouring temperatures are represented at different times which are shown in figure 3.14. The solidification front has been represented for 0.1 s, 0.5 s, 1 s, 1.5 s, and at the end of solidification for all pouring velocities and pouring temperatures.

After 0.1 s, the molten aluminium makes contact with the cavity's bottom and left side wall as indicated. Simultaneously liquid aluminium moves to the cavity's right side. The air is displaced as liquid aluminium filled the area. A liquid aluminium-air layer is formed initially around the flow of liquid aluminium.

Around 0.5 s, the liquid aluminium reached the left side of mould cavity and starts to solidify. When the pouring velocity is high, the metal enters the mould cavity at a faster rate, leading to an increased metal solidification rate. This is due to the fact that the molten metal comes into contact with the mould surface at a higher velocity, which can cause turbulence and movement of the metal. As a result, the heat transfer rate between the metal and the mould surface increases. Liquid aluminium metal continues to flow smoothly into the cavity. At 0.5 s, some air is trapped at the right side of the wall within the solid aluminium. However, it is not visible at 1 s as the air escapes during solidification process.

After 1 s, most of the aluminium metal is present in liquid form at this moment, particularly below the sprue as shown in figure 3.14. Initially, solidification mainly occurs at this right side of the cavity. Solidification of aluminium gradually increases with time. When liquid metal reaches the right side of the cavity after traveling some distance it loses flowing velocity because when the molten metal enters the mould cavity, its velocity will decrease due to the resistance offered by the mould material. A liquid aluminium-air mixture is formed upon the solidified aluminium metal at the right upper side of the cavity. Between 0.5 s and 1 s, a variety of phases are present, including liquid aluminium, liquid-solid aluminium mixture, solid aluminium, liquid aluminium-air mixture, solid aluminium-air mixture, and air. When pouring velocity increases, the metal filling also increases. Thus a more amount of liquid reaches to the right side of the cavity than low pouring velocity. At 1.5 s the solidification process continue in the mould cavity. The depth of aluminium solidified metal is higher at the right wall and low in the middle below the riser. Some molten aluminium is present in liquid form in the middle of the cavity below the riser.

Pouring velocity, Pouring temperature	0.1 s	0.5 s	1 s	1.5 s	End of solidification
380 mm/s, 983 K					
380 mm/s, 1003 K					
380 mm/s, 1033 K					
450 mm/s, 983 K				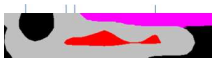	
450 mm/s, 1003 K				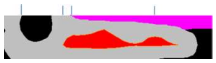	

Pouring velocity, Pouring temperature	0.1 s	0.5 s	1 s	1.5 s	End of solidification
450 mm/s, 1033 K				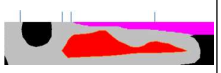	
520 mm/s, 983 K					
520 mm/s, 1003 K				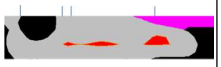	
520 mm/s, 1033 K					

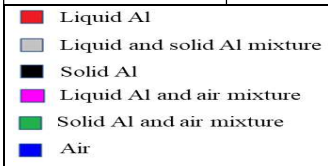

Figure 3.14: Solidification analysis for various pouring velocities and temperatures at a mould temperature of 503K.

A liquid aluminium-air mixture layer is also formed at right upper side of the cavity at all pouring velocities. At the end of solidification, the liquid aluminium-air mixture layer is not found as the air escapes from the metal through riser.

3.5.2 Hot Spot

In Figure 3.10, Figure 3.12, and Figure 3.14, the solidification processes are depicted at 1.5 s before complete solidification. This thesis primarily focuses on investigating the hot spot zones during casting at 1.5 s. It should be noted that at 1.5 s, there is still some liquid aluminium present below the riser. As liquid aluminium exhibit higher temperature compared to the surrounding areas, Hence, the hot spots are averagely located below the riser. However, as the solidification progresses and reaches completion, all the liquid aluminium solidifies, and almost no uneven solidification zones are observed. It is important to note that, prior to solidification, hot spots or areas of uneven solidification/cooling are observed below the riser. The same observation regarding the location of the hot spot was recognized by Zhou et al. [139].

3.5.2.1. Mould Initial Temperature 30°C (303 K)

The hot spot zones are mostly found at pouring velocities ranging from 380-450 mm/s, as liquid aluminium exists below the riser. When compared to other pouring temperatures, the size of the hot spot zone below the riser at 983 K is relatively small. Moreover, at a pouring velocity of 520 mm/s, this zone is not detected at 983 K. These observations suggest that high pouring velocities and low pouring temperatures have relatively small or negligible hot spot zones. Higher pouring velocities and lower pouring temperatures which can help to minimize the formation of hot spots by promote more uniform solidification. Increasing pouring velocities and lowering pouring temperatures ensures more uniform mould filling and maintain a more controlled and uniform temperature throughout the casting at the end stage of solidification. The use of risers can also help to reduce the formation of hot spots by providing additional metal to compensate for shrinkage during solidification [202]. This can help to promote more uniform cooling and minimize the formation of hot spots.

3.5.2.2. Mould Initial Temperature 130°C (403 K)

The observations in Figure 3.12 indicate that when the mould is preheated to 403 K, the location of the hot spot and the impact of pouring velocity and temperature on the hot spot closely resemble the observations made at the mould's initial temperature of 303 K.

3.5.2.3. Mould Initial Temperature 230°C (503 K)

Based on the observations presented in Figure 3.14, it has been noted that when the mould is preheated to 503 K, the location of the hot spot and the impact of pouring velocity and temperature on the hot spot are closely similar to those observed at the mould's initial temperatures of 303 K and 403 K.

Therefore, the location of the hot spot and the influence of pouring velocity and pouring temperature on the hot spot are almost independent of the mould initial temperature. The present thesis focuses on identifying the average hot spot location, but their impact has not been thoroughly investigated. Hot spots may result the defects like porosity, shrinkage, and cracking [64]. While porosity has been examined in this study, the analysis of other defects will be pursued in future research.

3.5.3 Measurement of Porosity and its Characteristics

3.5.3.1 Mould Initial Temperature 30°C (303 K)

Porosity of the casting is determined at each simulation variant and the relationship between porosity with pouring temperature and pouring velocity is illustrated in figure 3.15 and table 3.4. The summary of results is depicted in table 3.5 where the percentage of decrease of porosity is presented. At 983 K (figure 3.15), porosity decreases gradually with increasing pouring velocity, with values of 0.1706, 0.0914, 0.0481, 0.0044, and 0.0023 for pouring velocities of 380, 415, 450, 485, and 520 mm/s, respectively. Porosity decreases significantly by around 98.6%, from 0.1706 to 0.0023, when pouring velocity increases from 380 mm/s to 520 mm/s (table 3.5). This trend is consistent at 1003 K where porosity decreases gradually with increasing pouring velocity, with values of 0.1706, 0.1007, 0.0858, 0.0044, and 0.0024 for pouring velocities of

380, 415, 450, 485, and 520 mm/s, respectively. Here, porosity decreases considerably from 0.1706 to 0.0024, a reduction rate of around 98.6%, when pouring velocity rises from 380 mm/s to 520 mm/s (table 3.5). Similarly, at 1033 K pouring temperature, the values of porosity are 0.1854, 0.1038, 0.0906, 0.0045, and 0.0024 for pouring velocities of 380, 415, 450, 485, and 520 mm/s, respectively. At 1033 K, porosity decreases gradually with increasing pouring velocity, with a similar trend as seen in the other pouring temperatures. Porosity decreases considerably from 0.1854 to 0.0024 when pouring velocity increases from 380 mm/s to 520 mm/s at 1033 K, with a reduction rate of around 98.7%, as shown in table 3.5. It can be observed that porosity reduces gradually with the increase in pouring velocity for a constant pouring temperature. Similar findings were reported by Xu et al. [203] in their research, where they showed that porosity could be minimized to 0.9% by increasing injection velocity, with the minimum porosity being attained at 0.7 m/s of aluminium alloy.

Porosity decreases with pouring velocity because the increase in the velocity of the molten metal results in increased turbulence in the cavity, which helps to escape the trapped air from the metal through the riser. A riser can act as a venting system, allowing air to escape from the metal.

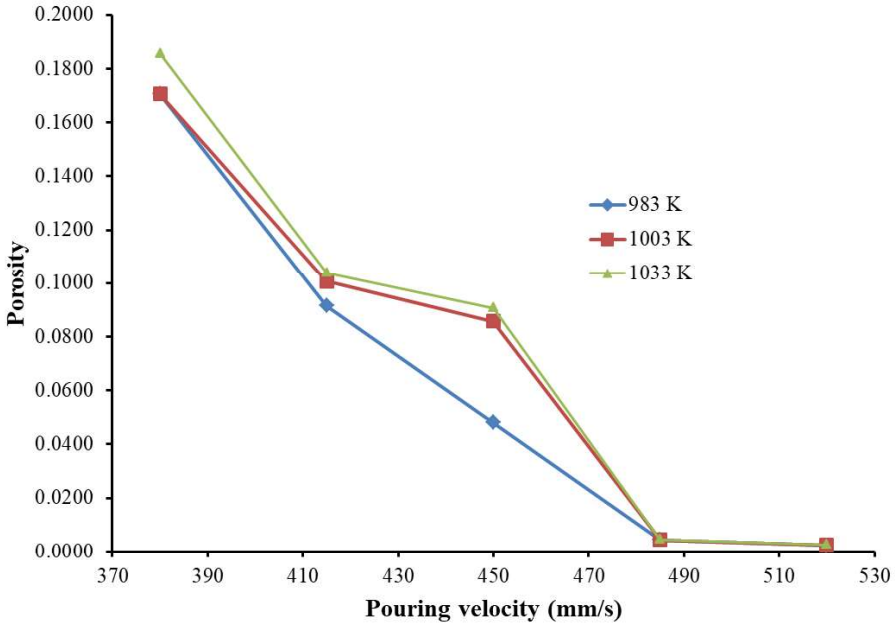

Figure 3.15: Variation of porosity with pouring velocities and temperatures at T_0=303 K.

It is observed that (figure 3.15 and table 3.4) at a velocity of 380 mm/s, the porosity remains almost unchanged over the temperature range of 983 K to 1003 K, but then increases with temperature beyond that range, from 0.1706 to 0.1854. At a pouring velocity of 415 mm/s, the porosity increases with temperature, with values of 0.0914, 0.1007, and 0.1038 observed at pouring temperatures of 983 K, 1003 K, and 1033 K, respectively.

Table 3.4: Porosity variations across different combinations of pouring temperatures, pouring velocities, and mould initial temperatures.

Pouring temperature (K)	**Pouring velocity (mm/s)**	**Porosity for mould initial temperature 303 K**	**Porosity for mould initial temperature 403 K**	**Porosity for mould initial temperature 503 K**
983	380	0.1706	0.0108	0.0088
	415	0.0914	0.0095	0.0052
	450	0.0481	0.0068	0.0029
	485	0.0044	0.0029	0.0020
	520	0.0023	0.0017	0.0012
1003	380	0.1706	0.0119	0.0091
	415	0.1007	0.0110	0.0063
	450	0.0858	0.0100	0.0058
	485	0.0044	0.0033	0.0021
	520	0.0024	0.0018	0.0013
1033	380	0.1854	0.0191	0.0099
	415	0.1038	0.0142	0.0086
	450	0.0906	0.0141	0.0077
	485	0.0045	0.0037	0.0023
	520	0.0024	0.0021	0.0019

The simulation results depicted in figure 3.15 indicate that, at 415 mm/s, the porosity slowly increases from around 9 to 10% as the pouring temperature rises from 983 K to 1033 K. Similarly, at a pouring velocity of 450 mm/s, the porosity increases with pouring temperature, with values of 0.0481, 0.0858, and 0.0906 observed for pouring temperatures of 983 K, 1003 K, and 1033 K, respectively. At 983 K and a pouring velocity of 450 mm/s, the porosity is only 4.8%, compared to about 8.6% and 9% at 1003 K and 1033 K, respectively. For velocities of 485 mm/s and 520 mm/s, the porosity is found to be very small. At 485 mm/s, the porosity remains almost constant over the temperature range of 983 K to 1003 K, but then increases as the pouring temperature reaches 1033 K. At a velocity of 485 mm/s, the porosity is low (about 0.4 %) and remains nearly constant as the pouring temperature rises.

Similarly, at a velocity of 520 mm/s, the porosity is 0.0023 for pouring at 983 K, 0.0024 for pouring at 1003 K, and 0.0024 for pouring at 1033 K. The porosity increases with pouring temperature from 983 K to 1003 K, then remains almost constant up to 1033 K. At 520 mm/s, the porosity is very small, just around 0.2%, throughout the range of 983 K to 1033 K. Overall, the results demonstrate that the porosity value is found to be extremely low for velocities of 485 mm/s and 520 mm/s, and the porosity is nearly constant whatever the pouring temperature.

Table 3.5: Effects of different pouring and mould initial temperatures on the percentage of porosity reduction from 380 to 520 mm/s velocity.

Pouring Temperature (K)	**The percentage of porosity decreased from a velocity 380 to 520 mm/s**		
	For mould initial temperature 303 K	**For mould initial temperature 403 K**	**For mould initial temperature 503 K**
983	98.6	84.26	86.4
1003	98.6	84.87	85.7
1033	98.7	89	80.8

As a findings, porosity is almost constant within a certain temperature range and increases in another temperature range for pouring velocities of 380 mm/s, 485 mm/s, and 520 mm/s. Mozammil et al**.** [116] and Jahangiri et al. [17] have previously reported that porosity tends to increase with pouring temperature. In the current investigation, it is observed that porosity does not always increase with temperature and may remain constant or nearly constant in certain temperature ranges. However, the data revealed that porosity increases with pouring temperature for the velocities of 380 mm/s, 485 mm/s, and 520 mm/s when the temperature range is large, but the rate of increase is slow. Air porosity typically arises in the metal casting due to the high solubility of air in aluminium metal at higher temperatures. This air solubility tends to increase as the pouring temperature rises, leading to a corresponding increase in porosity.

The decrease in porosity is observed when the pouring temperature is reduced and the pouring velocity is increased. While the rate of porosity reduction with decreasing temperature is relatively slow, the rate of porosity reduction with increasing velocity is significantly high. These observations lead to the conclusion that porosity is less dependent on pouring temperature compared to pouring velocity.

3.5.3.2 Mould Initial Temperature 130°C (403 K)

The relationship between porosity, pouring temperature, and pouring velocity is illustrated in figure 3.16 and table 3.4 at mould Temperature 130°C. At a pouring temperature of 983 K (figure 3.16), there is a gradual decrease in porosity with increasing pouring velocity. The values of porosity are 0.0108, 0.0095, 0.0068, 0.0029, and 0.0017 for pouring velocities of 380, 415, 450, 485, and 520 mm/s, respectively. Porosity decreases significantly by approximately 84.26% when the pouring velocity increases from 380 mm/s to 520 mm/s (table 3.5).

This trend is also observed at a pouring temperature of 1003 K, where porosity gradually decreases with increasing pouring velocity. The values of porosity are 0.0119, 0.0110, 0.0100, 0.0033, and 0.0018 for pouring velocities of 380, 415, 450, 485, and 520 mm/s, respectively. Here, porosity decreases considerably from 0.0327 to 0.0038, with a reduction rate of around 84.87%, when pouring velocity increases from 380 mm/s to 520 mm/s (table 3.5).

Similarly, at a pouring temperature of 1033 K, the values of porosity are 0.0191, 0.0142, 0.0141, 0.0037, and 0.0021 for pouring velocities of 380, 415, 450, 485, and 520 mm/s, respectively. Porosity decreases gradually with increasing pouring velocity, following a similar trend as observed at the other pouring temperatures. The porosity decreases significantly from 0.0381 to 0.0021 when the pouring velocity increases from 380 mm/s to 520 mm/s at 1033 K, with a reduction rate of around 89%, as presented in table 3.5.

At a velocity of 380 mm/s, it is observed (figure 3.16 and table 3.4) that porosity increases with pouring temperature, with values of 0.0108, 0.0119, and 0.0191at pouring temperatures of 983 K, 1003 K, and 1033 K, respectively. Similarly, at a pouring velocity of 415 mm/s, porosity also increases with temperature, with values of 0.0095, 0.0110, and 0.0142 for pouring temperatures of 983 K, 1003 K, and 1033 K, respectively.

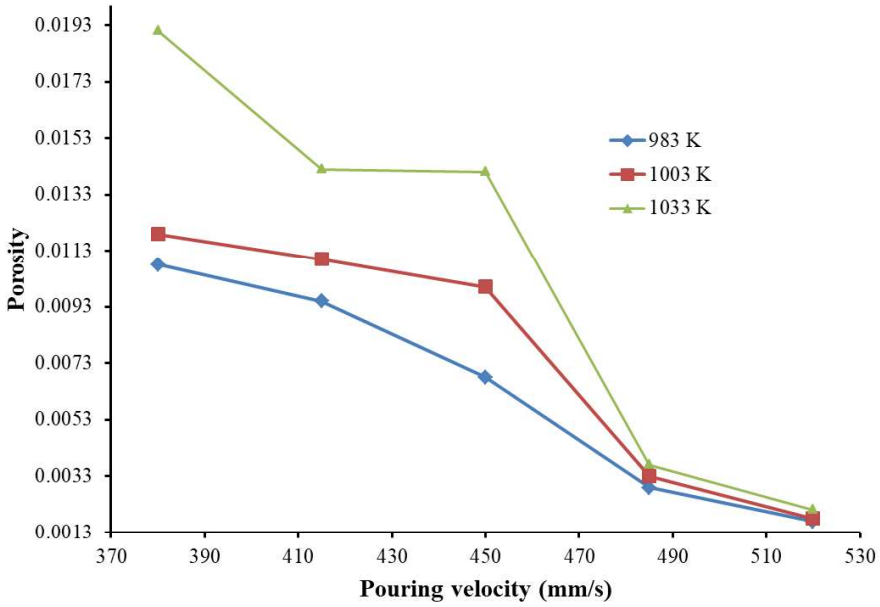

Figure 3.16: Variation of porosity with pouring velocities and temperatures at T_0=403 K.

Figure 3.16 shows that at 415 mm/s, porosity gradually increase from around 0.95% to 1.42% as pouring temperature rises from 983 K to 1033 K. In addition, at a pouring velocity of 450 mm/s, porosity increases with pouring temperature, with values of 0.0068, 0.0100, and 0.0141 for pouring temperatures of 983 K, 1003 K, and 1033 K, respectively. Furthermore, at a pouring

velocity of 485 mm/s, porosity increases with pouring temperature, with values of 0.0029, 0.0033, and 0.0037 for pouring temperatures of 983 K, 1003 K, and 1033 K, respectively. At a pouring velocity of 520 mm/s, porosity also increases with pouring temperature, with values of 0.0017, 0.0018, and 0.0021 for pouring temperatures of 983 K, 1003 K, and 1033 K, respectively.

The results show that increasing the pouring velocity while maintaining a constant pouring temperature results in a gradual decrease in porosity. Furthermore, increasing the pouring temperature causes an increase in porosity, but at a slow rate. Notably, the same patterns were observed at 303 K mould temperature.

3.5.3.3 Mould Initial Temperature 230°C (503 K)

Figure 3.17 and table 3.4 shows the variation in porosity with pouring temperature and pouring velocity at 230°C mould temperature. At a pouring temperature of 983 K, there is a gradual decrease in porosity with increasing pouring velocity. The values of porosity are 0.0088, 0.0052, 0.0029, 0.0020, and 0.0012 for pouring velocities of 380, 415, 450, 485, and 520 mm/s, respectively. The porosity decreases significantly by approximately 86.4% when the pouring velocity increases from 380 mm/s to 520 mm/s (table 3.5). This trend is also observed at a pouring temperature of 1003 K, where porosity gradually decreases with increasing pouring velocity. The values of porosity are 0.0091, 0.0063, 0.0058, 0.0021, and 0.0013 for pouring velocities of 380, 415, 450, 485, and 520 mm/s, respectively. Here, porosity decreases considerably from 0.0091 to 0.0013, with a reduction rate of around 85.7%, when pouring velocity increases from 380 mm/s to 520 mm/s (table 3.5). Similarly, at a pouring temperature of 1033 K, the values of porosity are 0.0099, 0.0086, 0.0077, 0.0023, and 0.0019 for pouring velocities of 380, 415, 450, 485, and 520 mm/s, respectively. Porosity decreases gradually with increasing pouring velocity, following a similar trend as observed at the other pouring temperatures. The porosity decreases significantly from 0.0099 to 0.0019 when the pouring velocity increases from 380 mm/s to 520 mm/s at 1033 K, with a reduction rate of around 80.8%, as presented in table 3.5.

At a velocity of 380 mm/s, it is observed (figure 3.17 and table 3.4that porosity increases with pouring temperature, with values of 0.0088, 0.0091, and 0.0099 at pouring temperatures of 983 K, 1003 K, and 1033 K, respectively. Similarly, at a pouring velocity of 415 mm/s, porosity also increases with temperature, with values of 0.0052, 0.0063, and 0.0086 for pouring temperatures of 983 K, 1003 K, and 1033 K, respectively. In addition, at a pouring velocity of 450 mm/s, porosity increases with pouring temperature, with values of 0.0029, 0.0058, and 0.0077 for pouring temperatures of 983 K, 1003 K, and 1033 K, respectively. Furthermore, at a pouring velocity of 485 mm/s, porosity increases with pouring temperature, with values of 0.0020, 0.0021, and 0.0023 for pouring temperatures of 983 K, 1003 K, and 1033 K, respectively. At a pouring velocity of 520 mm/s, porosity also increases with pouring temperature, with values of 0.0012, 0.0013, and 0.0019 for pouring temperatures of 983 K, 1003 K, and 1033 K, respectively.

The findings indicate that by increasing the pouring velocity while keeping the pouring temperature constant, porosity gradually decreases. Moreover, raising the pouring temperature leads to an increase in porosity, but at a slower rate. Importantly, the same trends were observed at mould temperatures of 303 K and 403 K. In general, lowering the pouring temperature and increasing the pouring velocity lead to a reduction in porosity. While the decrease in porosity is relatively slow with decreasing temperature, it is significantly higher with increasing velocity. From these observations, it can be concluded that porosity is more dependent on pouring velocity than on pouring temperature. In general, for many castings including aluminium, a porosity range of 2- 4% is considered acceptable [204]. In this thesis, all porosity values are shown for different pouring parameters. A porosity below 0.0099 (0.99%) is assumed to be negligible in the aluminium volume fraction contour diagram due to its extremely small valued impact on the visual representation using color coding.

3.5.4 Location of Porosity

Once the porosity is measured, it is important to identify the location of porosity and location of maximum porosity over the thickness of the casting. This information can help determine the

thickness of the casting with no or negligible pores (i.e. filled by about 100% aluminium metal) for different casting parameters.

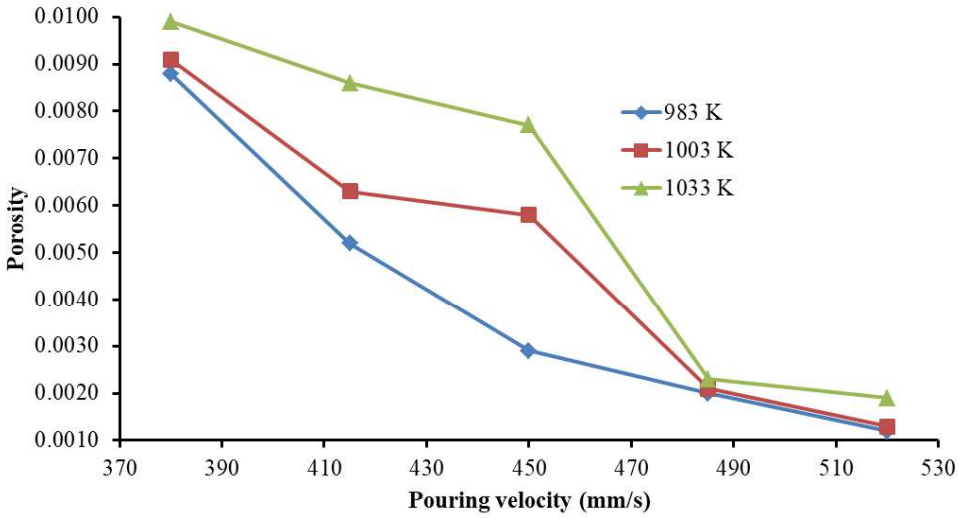

Figure 3.17: Variation of porosity with pouring velocities and temperatures at T_0=503 K.

To accomplish this, the contours of the aluminium volume fraction are generated for different planes in the casting domain. The volume fractions of aluminium are drawn on three cross-sectional planes on the z-x plane. The front face of the casting, located in the z-x plane as shown in figures 3.4 and 3.5, is the first plane. The second plane is situated 15 mm away from the front face along the y-axis, and the third plane is in the middle of the casting, 30 mm away from the front face along the y-axis. The contour diagram displays dark red fill color to represent approximately 100% aluminium volume fraction, while dark blue fill color represents around 0% aluminium volume fraction (i.e. indicating 100% air volume fraction). Other colors represent a mixture of air and aluminium volume fraction, where the percentage of aluminium volume fraction is indicated by the corresponding color. Thomas et al. [205] also observed the contour of the volume fraction in centrifugal casting and measured the concentration of particles using it.

3.5.4.1 Mould Initial Temperature 30°C (303 K)

The contours of the aluminium volume fraction at pouring velocity 380 mm/s and pouring temperature 983 K are shown in figure 3.18 after the solidification time.

Figures 3.18(a), (b), and (c) indicate that the aluminium volume fraction decreases as it approaches the top of the cavity due to air moving towards the top and escaping through the riser. The contours of the aluminium volume fraction is found to be the same on any z-x plane for various values of y for a specific set of casting conditions.

Figure 3.18 shows that the contours of the aluminium volume fraction were uniform on the three planes.

The study also analysed the contours of the aluminium volume fraction for other pouring parameter combinations on the same three planes. After careful observation, it is determined that the contours of the aluminium volume fraction are identical on any z-x plane for different y values under specific casting parameter conditions.

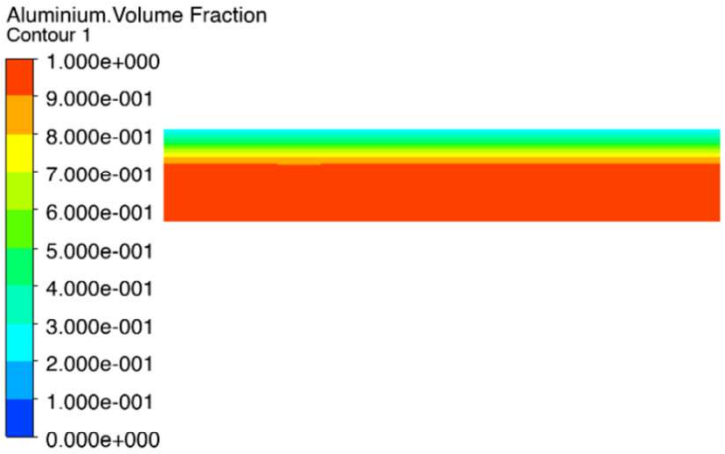

Figure 3.18a: At first plane.

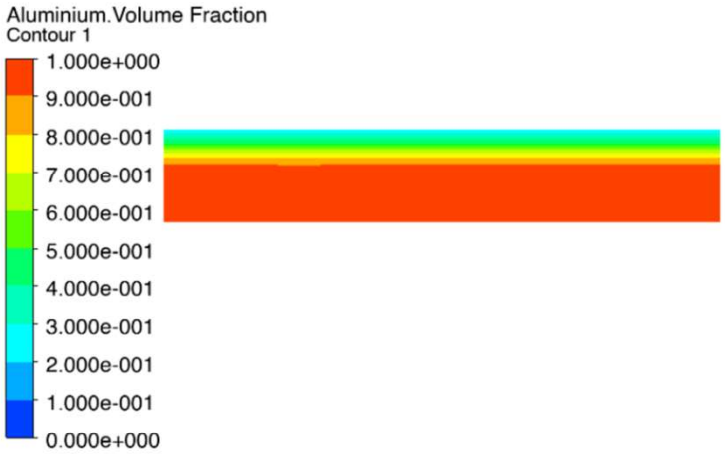

Figure 3.18b: At second plane.

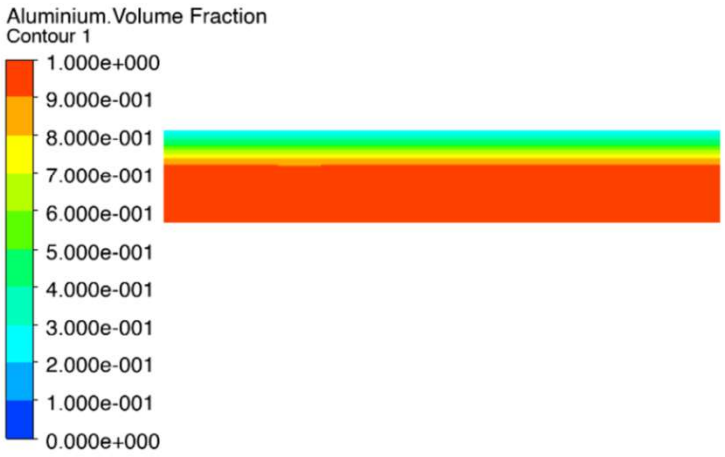

Figure 3.18c: At third plane

Figure 3.18: Contours of aluminium volume fraction at 380 mm/s (v_p) and 983 K (T_p), illustrated after completion of solidification at T_0=303 K.

Therefore, figure 3.19 represents the contours of the aluminium volume fraction for other pouring parameter combinations at the middle plane. All the contours have been drawn after the completion of solidification time.

Based on the generalized observations shown in Figure 3.19, it can be concluded that the percentage of porosity increases gradually from almost zero value (near the 100% aluminium region) to its maximum value along the thickness of the casting, reaching its highest value at the top surface of the casting. The presence of porosity is observed to be most prominent on the top surface of the casting, as shown in Figure 3.19.

This observation is same with the findings of Cao et al. [206]. At 380 mm/s pouring velocity and 983 K pouring temperature, the top surface of the casting contains 70% of the total porosity. A pouring velocity of 485 mm/s or 520 mm/s appears to result in a negligible amount of porosity (less than 0.45%), indicating that the aluminium volume fraction is almost 100%. As shown in figure 3.9 and figure 3.11, two layers are formed in the solidified casting after solidification, one of pure solid aluminium and the other of a solid aluminium-air mixture. It has been observed that the layer of solid aluminium-air mixture is primarily responsible for the creation of porosity.

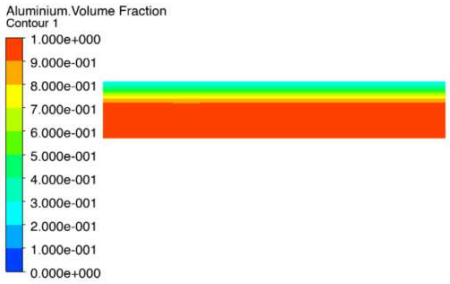

(i): 380 mm/s, 983 K

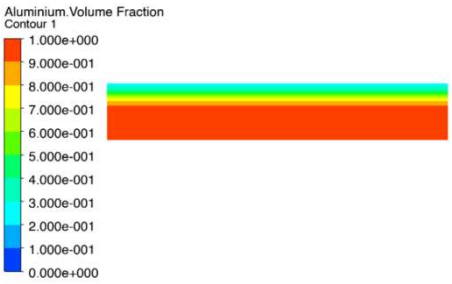

(ii): 380 mm/s, 1003 K

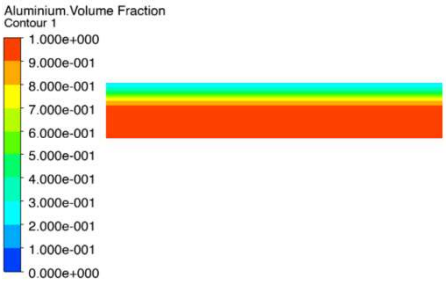

(iii): 380 mm/s, 1033 K

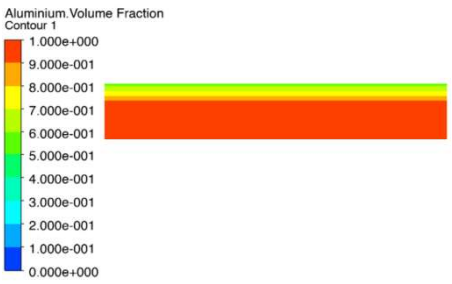

(iv): 415 mm/s, 983 K

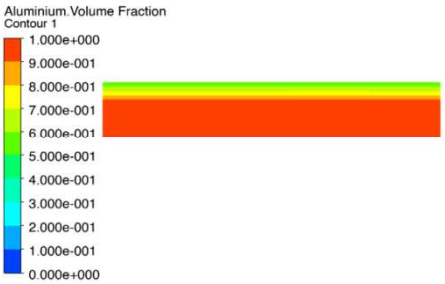

(v): 415 mm/s, 1003 K

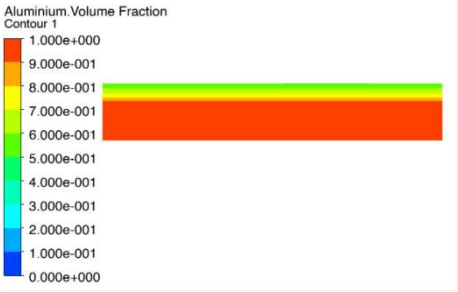

(vi): 415 mm/s, 1033 K

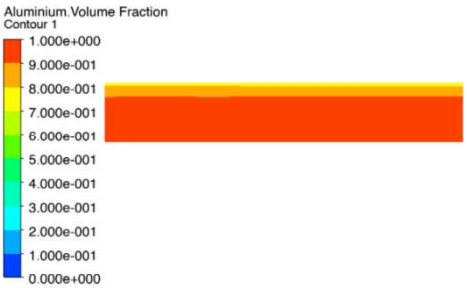

(vii): 450 mm/s, 983 K

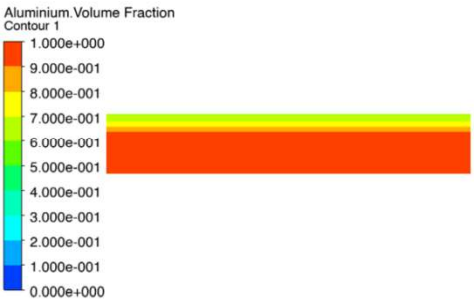

(viii): 450 mm/s, 1003 K

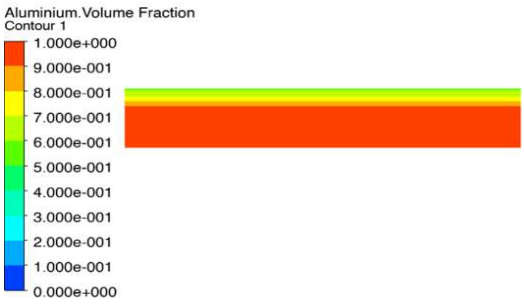

(ix): 450 mm/s, 1033 K

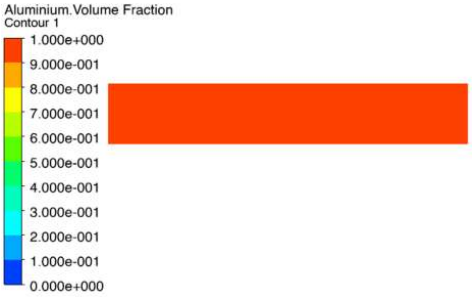

(x): 485 mm/s, 983 K

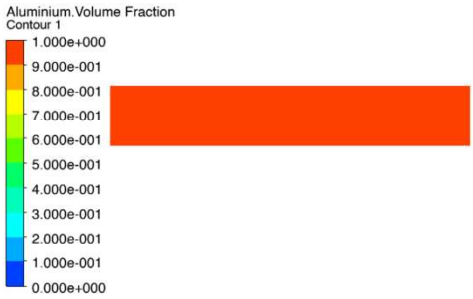

(xi): 485 mm/s, 1003 K

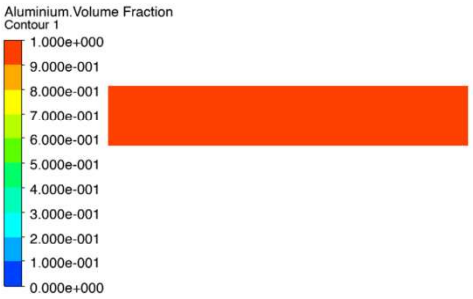

(xii): 485 mm/s, 1033 K

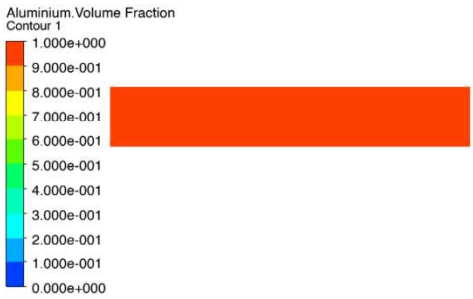

(xiii): 520 mm/s, 983 K

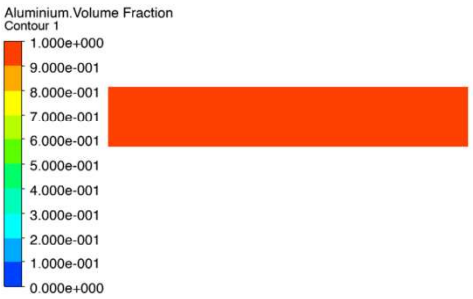

(xiv): 520 mm/s, 1003 K

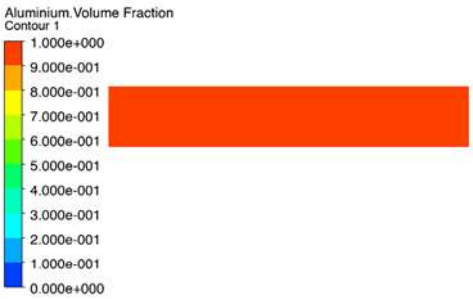

(xv): 520 mm/s, 1033 K

Figure 3.19: Contours of aluminium volume fraction for different pouring velocities and temperatures after the completion of solidification at T_0=303 K.

3.5.4.2 Mould Initial Temperature 130°C (403 K)

Figure 3.20 depicts the contours of the aluminium volume fraction at the middle plane, drawn after the completion of solidification time. Based on the generalized observations shown in figure 3.20, it can be concluded that the porosity is primarily located on the top surface of the casting. The presence of porosity is observed only at a pouring velocity of 380 mm/s, while other pouring velocities result in negligible amounts of porosity, indicating that the aluminium volume fraction is almost 100%

3.5.4.3 Mould Initial Temperature 230°C (503 K)

Figure 3.21 illustrates the contours of the aluminium volume fraction at the middle plane, and all the contours are drawn after the completion of the solidification time. Based on the generalized observations shown in figure 3.21, negligible amounts of porosity is present at all pouring velocities and pouring temperatures, indicating that the aluminium volume fraction is almost 100%.

In general, the air porosity is concentrated on the upper surface of the casting. The solidified casting typically consists of two layers: one layer comprising pure solid aluminium and the other consisting of a mixture of solid aluminium and air. Notably, the layer composed of solid aluminium-air mixture is primarily responsible for the formation of air porosity.

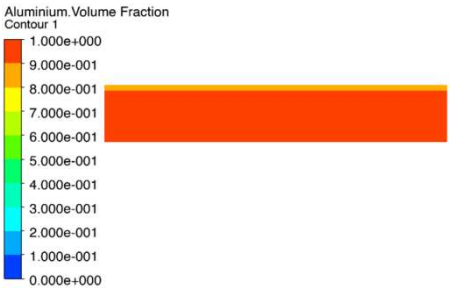

(i): 380 mm/s, 983 K

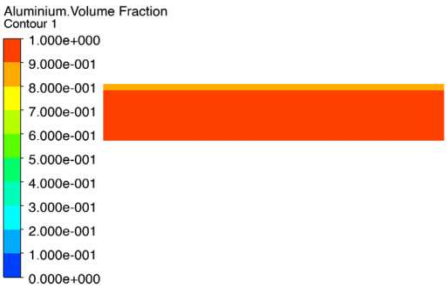

(ii): 380 mm/s, 1003 K

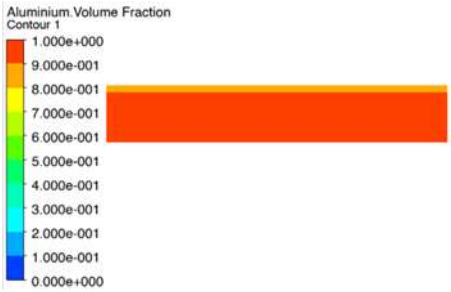

(iii): 380 mm/s, 1033 K

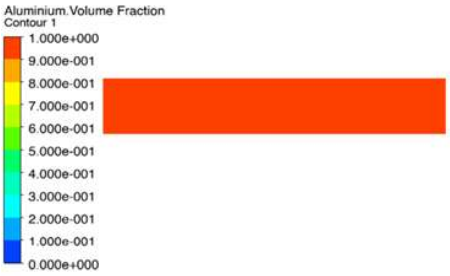

(iv): 415 mm/s, 983 K

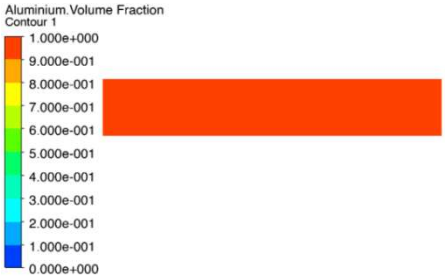

(v): 415 mm/s, 1003 K

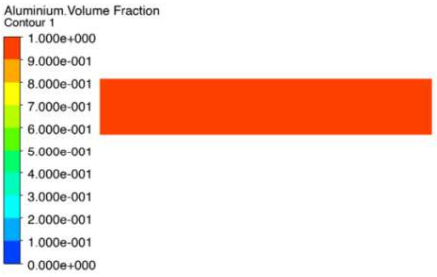

(vi): 415 mm/s, 1033 K

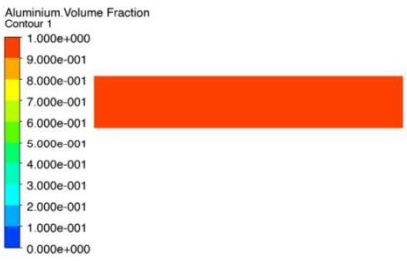

(vii): 450 mm/s, 983 K

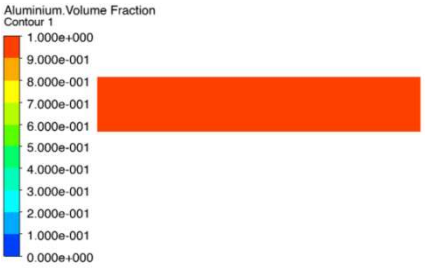

(viii): 450 mm/s, 1003 K

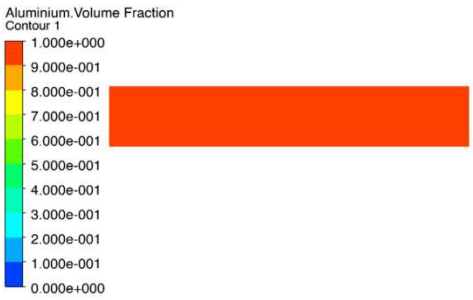

(ix): 450 mm/s, 1033 K

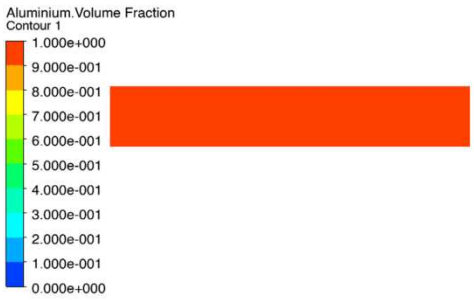

(x): 485 mm/s, 983 K

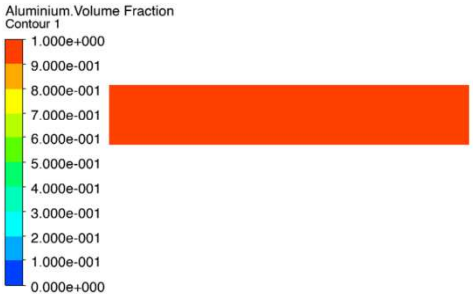

(xi): 485 mm/s, 1003 K

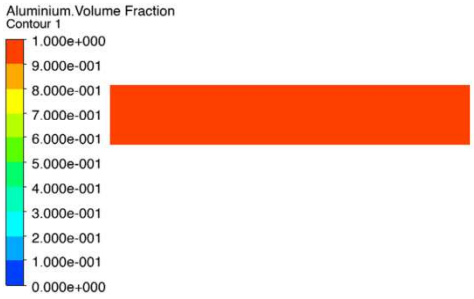

(xii): 485 mm/s, 1033 K

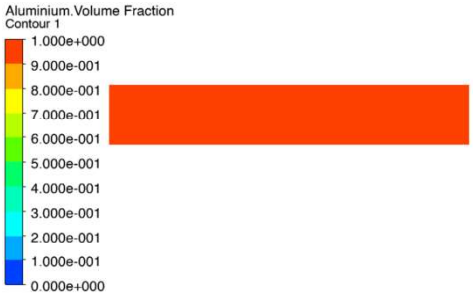

(xiii): 520 mm/s, 983 K

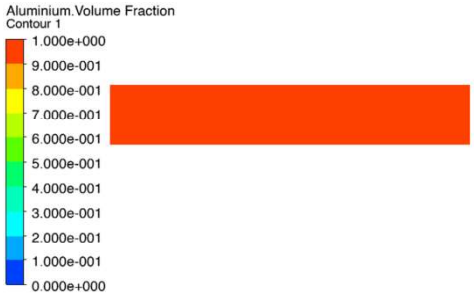

(xiv): 520 mm/s, 1003 K

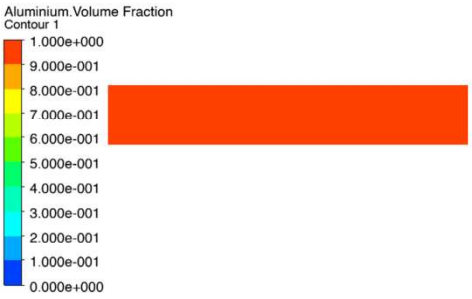

(xv): 520 mm/s, 1033 K

Figure 3.20: Contours of aluminium volume fraction for different pouring velocities and temperatures after the completion of solidification at T_0=403 K.

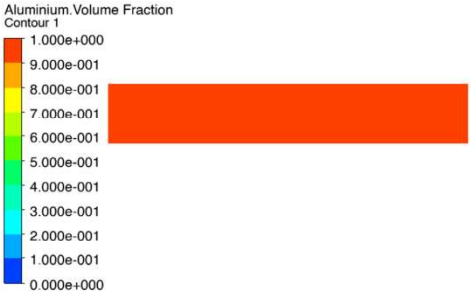

(i): 380 mm/s, 983 K

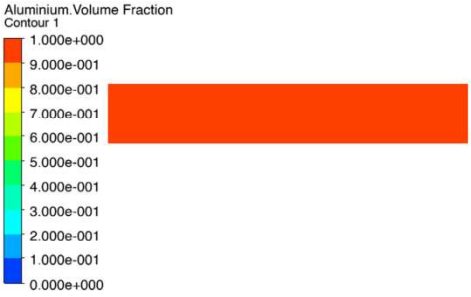

(ii): 380 mm/s, 1003 K

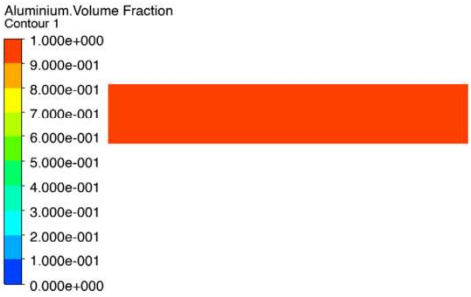

(iii): 380 mm/s, 1033 K

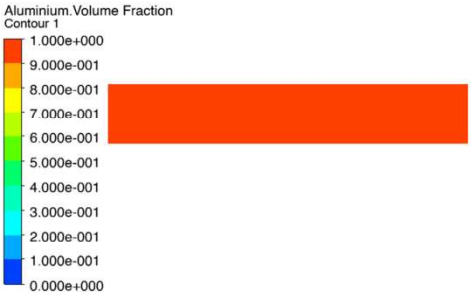

(iv): 415 mm/s, 983 K

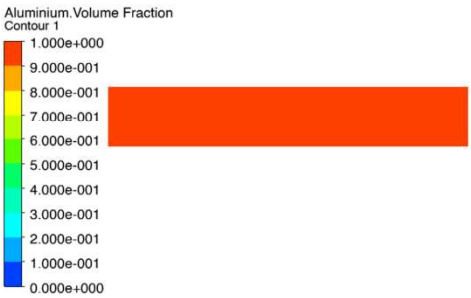

(v): 415 mm/s, 1003 K

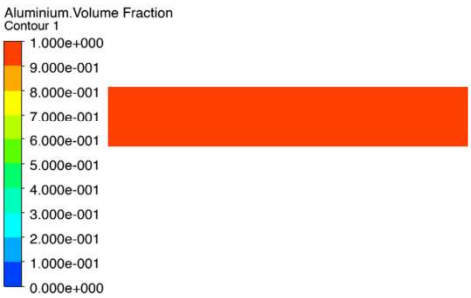

(vi): 415 mm/s, 1033 K

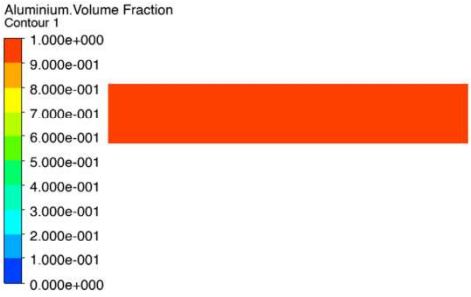

(vii): 450 mm/s, 983 K

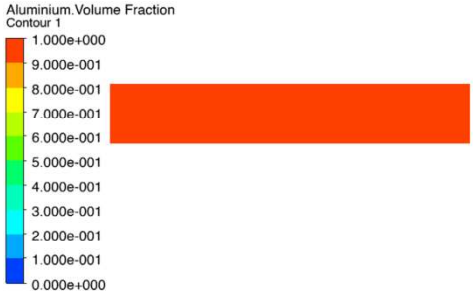

(viii): 450 mm/s, 1003 K

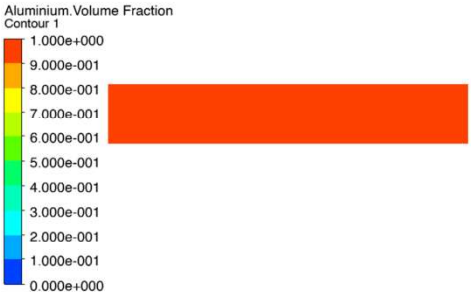

(ix): 450 mm/s, 1033 K

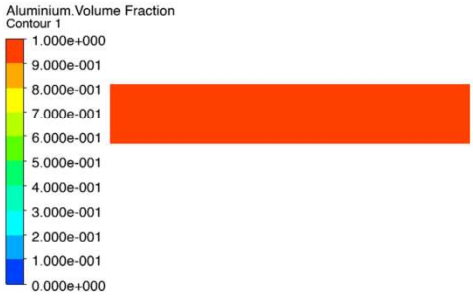

(x): 485 mm/s, 983 K

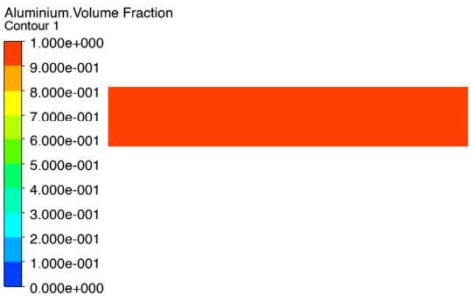

(xi): 485 mm/s, 1003 K

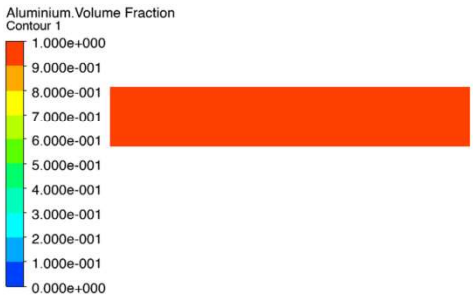

(xii): 485 mm/s, 1033 K

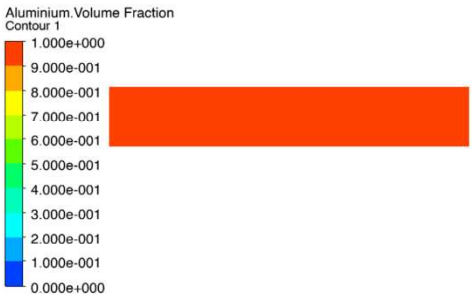

(xiii): 520 mm/s, 983 K

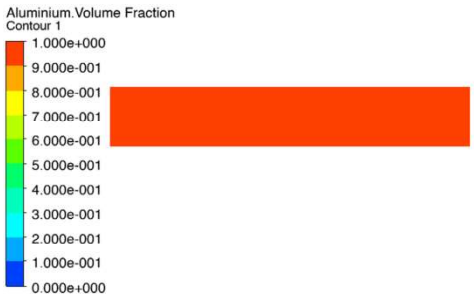

(xiv): 520 mm/s, 1003 K

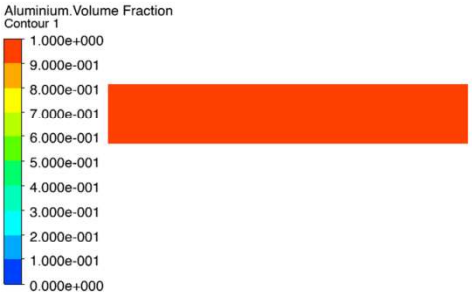

(xv): 520 mm/s, 1033 K

Figure 3.21: Contours of aluminium volume fraction for different pouring velocities and temperatures after the completion of solidification at T_0=503 K.

3.5.5 Metal Solidified Length

Table 3.6 illustrate the changes in the length of solidified aluminium (approximately 100% aluminium) filled from the base of the mould cavity (mm) under various pouring conditions.

3.5.5.1 Mould Initial Temperature 30°C (303 K)

Figure 3.22 and table 3.6 depict the variation of the length of solidified aluminium (approximately 100% aluminium) with pouring velocity and temperature at a mould temperature of 303 K. At 983 K, the length of solidified aluminium (approximately 100% aluminium) gradually increases from the base of the cavity with an increase in pouring velocity. The corresponding values are 6.5 mm, 6.7 mm, 7.7 mm, 10 mm, and 10 mm at pouring velocities [in mm/s] of 380, 415, 450, 485, and 520, respectively. A similar trend is observed at 1003 K, with

the length increasing progressively with pouring velocity, with values of 6.3 mm, 6.5 mm, 6.9 mm, 10 mm, and 10 mm for pouring velocities [in mm/s] of 380, 415, 450, 485, and 520. Likewise, at 1033 K, the length also gradually increases with pouring velocity, with values of 6.1 mm, 6.4 mm, 6.8 mm, 10 mm, and 10 mm at pouring velocities [in mm/s] of 380, 415, 450, 485, and 520. Based on the general observations, the length of solidified aluminium (approximately 100% aluminium) from the base of the mould cavity gradually increases with an increase in pouring velocity at a constant pouring temperature. Conversely, it increases with a decrease in pouring temperature for a constant pouring velocity. This is due to the fact that as the porosity decreases with increasing pouring velocity, the length of approximately 100% solid aluminium filled from the base of the mould cavity also increases. Similarly, due to the decrease in porosity with a decrease in pouring temperature for a constant pouring velocity, this length increases.

Figures 3.15, 3.19, and 3.22 illustrate that pouring velocities of 485 mm/s and 520 mm/s result in almost no porosity and lead to approximately 100% aluminium filling in the entire mould cavity. The results indicate that casting with negligible porosity is achieved at pouring velocities of 485 mm/s and 520 mm/s. Based on these observations, it is likely that the filling of the mould cavity with 100% aluminium (negligible porosity) occurs at a pouring velocity near 500 mm/s. At a pouring velocity of 380 mm/s, it can be observed that the upper surface of the mould cavity fills with less than 50% aluminium. If the pouring velocity is too low, the metal will solidify before it can fill the entire mould cavity, and lower pouring velocity result in a decrease in the percentage of aluminium in the casting. Conversely, pouring at a high velocity is not advisable as it can cause turbulence, leading to defects such as gas bubbles [116].The determination of pouring velocity is based on the height of the pouring basin [155]. The higher pouring velocity would require a higher pouring basin height, which in turn would increase the initial cost. An optimal pouring velocity should be maintained to achieve the best casting quality without incurring additional costs.

Table 3.6: Variation of solid aluminium filled from the base of cavity for different combinations of pouring velocities, pouring temperatures, and mould temperatures.

Pouring Temperature (K)	**Pouring Velocity (mm/s)**	**Length of fully-filled solidified aluminium from the base of the mould cavity for mould temperature 303 K (mm)**	**Length of fully-filled solidified aluminium from the base of the mould cavity for mould temperature 403 K (mm)**	**Length of fully-filled solidified aluminium from the base of the mould cavity for mould temperature 503 K (mm)**
983	380	6.5	8.5	10
	415	6.7	10	10
	450	7.7	10	10
	485	10.0	10	10
	520	10.0	10	10
1003	380	6.3	8.4	10
	415	6.5	10	10
	450	6.9	10	10
	485	10.0	10	10
	520	10.0	10	10
1033	380	6.1	8.3	10
	415	6.4	10	10
	450	6.8	10	10
	485	10.0	10	10
	520	10.0	10	10

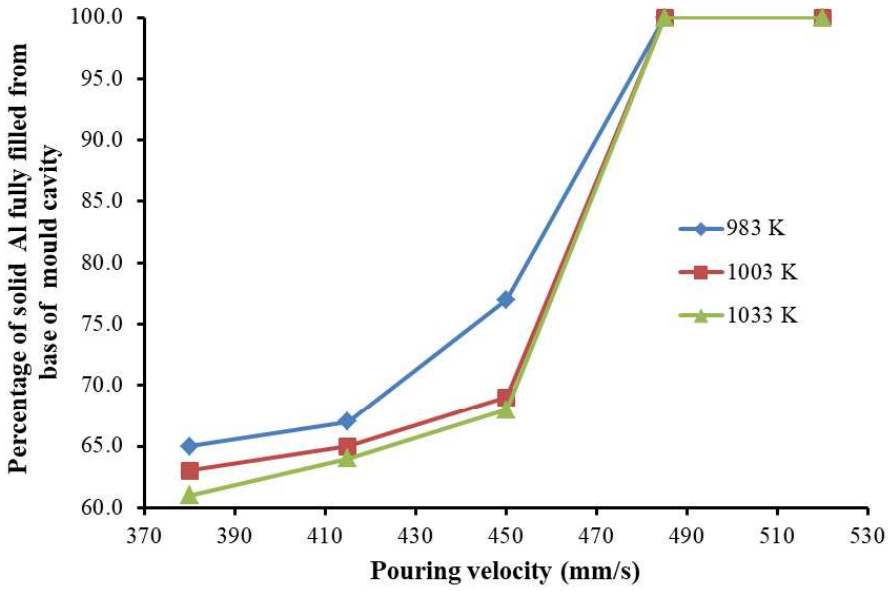

Figure 3.22: Variation of solidified aluminium length from the base of the mould cavity for different pouring velocities and temperatures at T_0=303 K.

Therefore, it is important to maintain an optimal pouring velocity. Based on the findings of the study, it can be concluded that the optimum pouring velocity is around 500 mm/s, as it resulted in casting with minimal porosity. Additionally, a nearly porous-free casting was observed at this pouring velocity. When the pouring temperature is high (as indicated in table 3.4), the casting tends to have high porosity, which leads to a decrease in strength. On the other hand, decreasing the pouring temperature reduces the fluidity of the molten metal. In the simulation, pouring temperatures of 983 K, 1003 K, and 1033 K are being used, and it is observed that the porosity is low at 983 K.

3.5.5.2 Mould Initial Temperature 130°C (403 K)

Table 3.6 presents the changes in solid aluminium filling from the base of the cavity under various pouring parameters at 403 K mould temperature. The length of solidified aluminium from the base of the mould cavity is 10 mm at pouring velocities ranging from 415-520 mm/s. Negligible porosity is observed for pouring velocities between 415-520 mm/s when the mould temperature is maintained at 403 K. This is due to the fact that an increase in mould temperature

leads to an increase in the fluidity of the metal, which results in a decrease in porosity. At 380 mm/s pouring velocity, the length of solidified aluminium from the base of the mould cavity is 8.5 mm, 8.4 mm, and 8.3 mm for pouring temperature of 983 K, 1003 K, and 103 K respectively. The length of solidified aluminium from the base of the mould cavity decreases with pouring temperature. This is due to the porosity increases with pouring temperature.

3.5.5.3 Mould Initial Temperature 230°C (503 K)

Table 3.6 presents the variation in solid aluminium filling from the base of the cavity under various pouring parameters at 503 K mould temperature. The length of solidified aluminium from the base of the mould cavity is 10 mm at pouring velocities ranging from 380-520 mm/s. Negligible porosity is observed for pouring velocities between 380-520 mm/s when the mould temperature is maintained at 403 K. This is due to the fact that an increase in mould temperature leads to an increase in the fluidity of the metal, which results in a decrease in porosity

Overall, for all mould temperatures, it is observed that the porosity is low at approximately 500 mm/s pouring velocity. This suggests that the optimum pouring velocity remains the same for all mould temperatures. Additionally, it is notable that for all mould temperatures, the porosity is low when the pouring temperature is 983 K.

3.5.6 Solidification Time

Table 3.7 presents the variation of solidification time at different pouring velocities and pouring temperatures for various mould temperatures.

3.5.6.1 Mould Initial Temperature 30°C (303 K)

Figure 3.23 and table 3.7 depict the variation of the solidification time with pouring velocity and temperature at a mould temperature of 303 K. At a pouring temperature of 983 K, the solidification times are 2 s, 1.98 s, 1.96 s, 1.91 s, and 1.9 s for 380, 415, 450, 485, and 520 mm /s pouring velocity respectively. As the pouring velocity increases, the solidification time decreases gradually. At a pouring temperature of 1003 K, the solidification times are 2.15 s, 2.05 s, 2 s, 1.97 s, and 1.92 s for 380, 415, 450, 485, and 520 mm /s pouring velocity

respectively. Similarly, for a pouring temperature of 1033 K, the solidification times are 2.2 s, 2.1 s, 2.05 s, 1.98 s, and 1.95 s for 380, 415, 450, 485, and 520 mm /s pouring velocity respectively.

Table 3.7: Variation of solidification time for different combinations of pouring velocities, pouring temperatures, and mould temperatures.

Pouring temperature (K)	**Pouring velocity (mm/s)**	**Solidification time (s) for mould initial temperature 303 K**	**Solidification time (s) for mould initial temperature 403 K**	**Solidification time (s) for mould initial temperature 503 K**
983	380	2	2.5	3.3
	415	1.98	2.45	3.25
	450	1.96	2.4	3.2
	485	1.91	2.3	3.1
	520	1.9	2.2	2.8
1003	380	2.15	2.6	3.5
	415	2.05	2.5	3.4
	450	2	2.45	3.3
	485	1.97	2.4	3.15
	520	1.92	2.3	3
1033	380	2.2	2.8	3.6
	415	2.1	2.7	3.5
	450	2.05	2.6	3.4
	485	1.98	2.5	3.3
	520	1.95	2.35	3.1

As observed, the solidification time decreases gradually as the pouring velocity increases, while it increases gradually with increasing pouring temperature. The solidification time during casting depends on a combination of factors, including the specific metal being cast, the mould material and design, and the casting parameters [138]. Increasing the pouring velocity during casting can decrease the solidification time. This is because the faster flow of the molten metal through the mould can result in a more efficient heat transfer process, which can lead to faster cooling and solidification of the metal. However, the solidification time depend all the parameters combined. The pouring temperature can affect the solidification time during casting. When the pouring temperature is increased, the molten metal has a higher thermal energy which increases the solidification time.

The average solidification time is determined by calculating the mean of all solidification times obtained across different pouring velocities and temperatures at a given mould temperature. At 303 K of mould temperature, the average solidification time is approximately 2.008 s or 2 s.

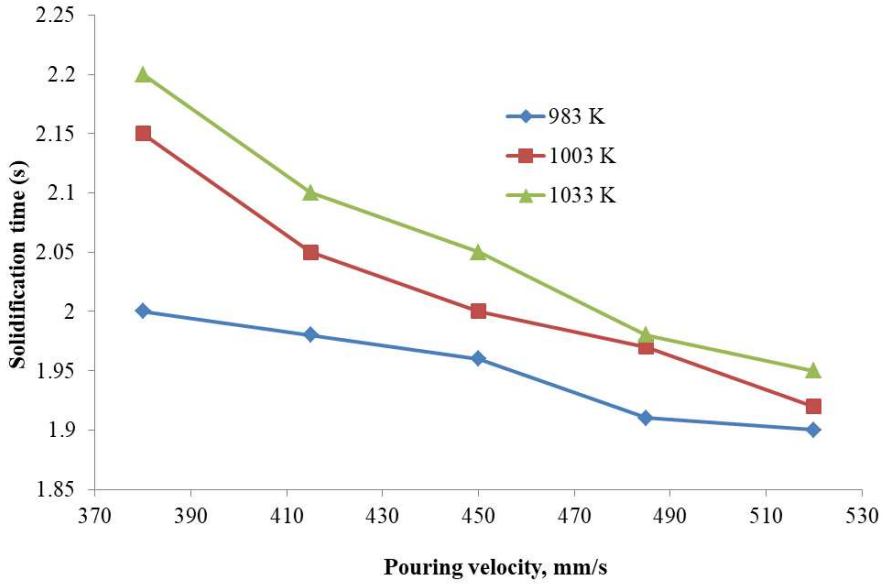

Figure 3.23: Variation of solidification time for different pouring velocities and temperatures at T_0=303 K.

3.5.6.2 Mould Initial Temperature 130°C (403 K)

The table 3.7 and figure 3.24 shows the solidification time for different pouring velocities and pouring temperatures at mould temperature of 403 K. At a pouring temperature of 983 K, the solidification times are 2.5 s, 2.45 s, 2.4 s, 2.3 s, and 2.2 s for 380, 415, 450, 485, and 520 mm /s pouring velocity respectively. As the pouring velocity increases, the solidification time decreases gradually. At a pouring temperature of 1003 K, the solidification times are 2.6 s, 2.5 s, 2.45 s, 2.4 s, and 2.3 s for 380, 415, 450, 485, and 520 mm /s pouring velocity respectively. Similarly, for a pouring temperature of 1033 K, the solidification times are 2.8 s, 2.7 s, 2.6 s, 2.5 s, and 2.35 s for 380, 415, 450, 485, and 520 mm /s pouring velocity respectively.

As observed, the solidification time decreases gradually as the pouring velocity increases, while it increases gradually with increasing pouring temperature. At 403 K of mould temperature, the average solidification time is 2.47 s.

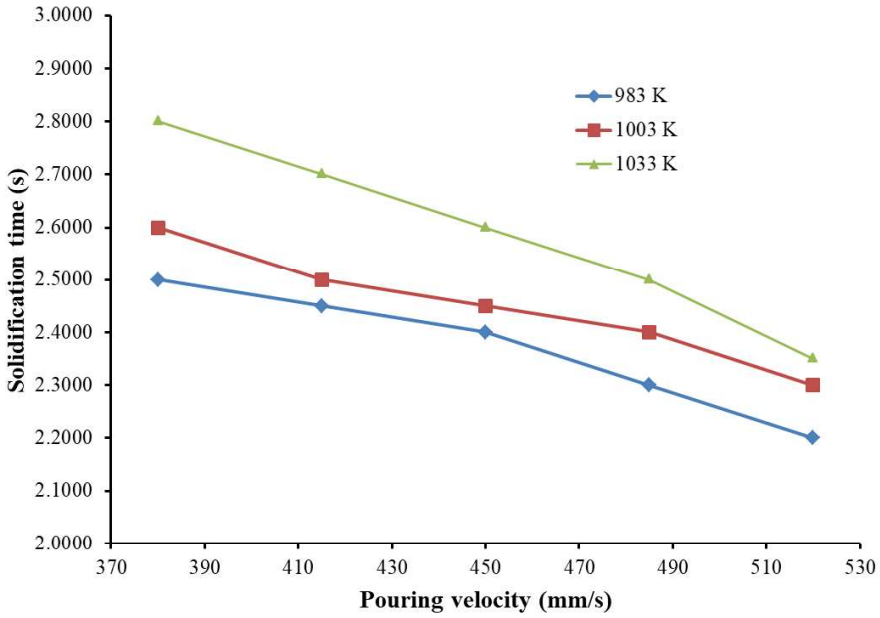

Figure 3. 24: Variation of solidification time for different pouring velocities and temperatures at T_0=403 K.

3.5.6.3 Mould Initial Temperature 230°C (503 K)

Table 3.7 and figure 3.25 present the solidification time for various pouring velocities and pouring temperatures at a mould temperature of 503 K. At a pouring temperature of 983 K, the solidification times are 3.3 s, 3.25 s, 3.2 s, 3.1 s, and 2.8 s for 380, 415, 450, 485, and 520 mm /s pouring velocity respectively. As the pouring velocity increases, the solidification time decreases gradually. At a pouring temperature of 1003 K, the solidification times are 3.5 s, 3.4 s, 3.3 s, 3.15 s, and 3 s for 380, 415, 450, 485, and 520 mm /s pouring velocity respectively. Similarly, for a pouring temperature of 1033 K, the solidification times are 3.6 s, 3.5 s, 3.4 s, 3.3 s, and 3.1 s for 380, 415, 450, 485, and 520 mm /s pouring velocity respectively.

As observed, the solidification time decreases gradually as the pouring velocity increases, while it increases gradually with increasing pouring temperature. At 503 K of mould temperature, the average solidification time is approximately 3.26 s. As the mould initial temperature increases, the solidification time also increases, because higher mould temperature contains more thermal energy.

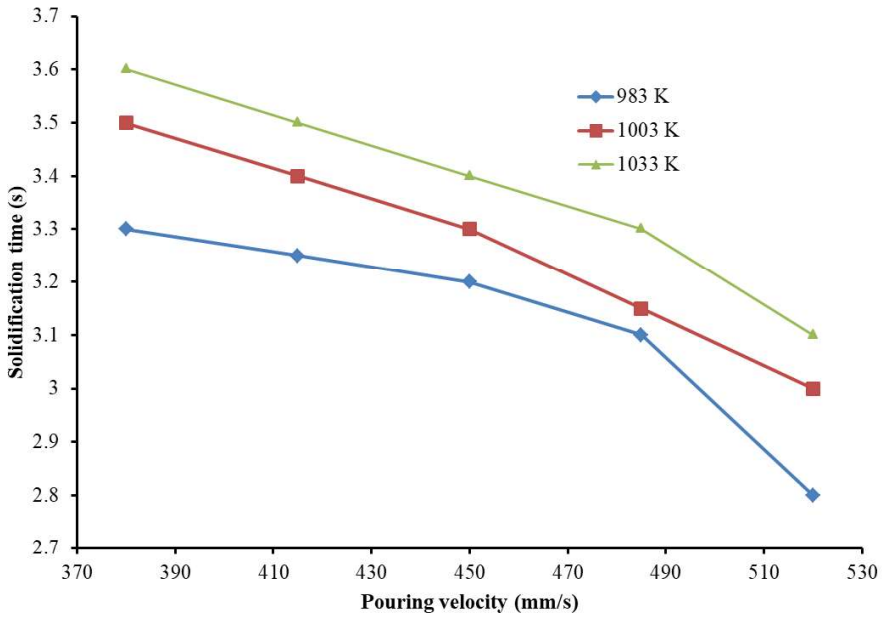

Figure 3.25: Variation of solidification time for different pouring velocities and temperatures at T_0=503 K.

3.5.7 Comparative Analysis

3.5.7.1 Comparative Analysis of Porosity for Different Mould Temperatures

Figures 3.26, 3.27, and 3.28 depict the relationship between porosity and pouring velocity and mould temperature at different pouring temperatures: 983 K, 1003 K, and 1033 K, respectively.

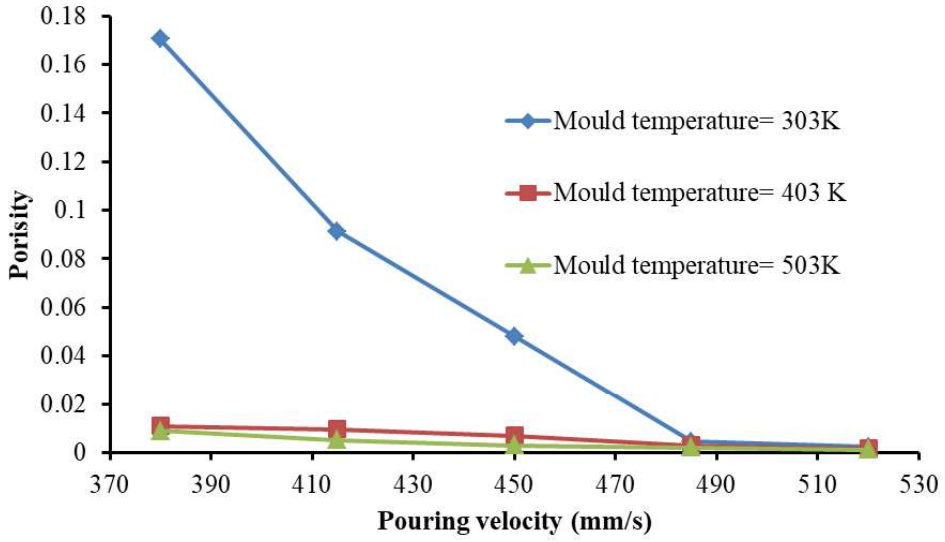

Figure 3.26: Variation of porosity with different pouring velocities and mould initial temperatures at 983 K pouring temperature.

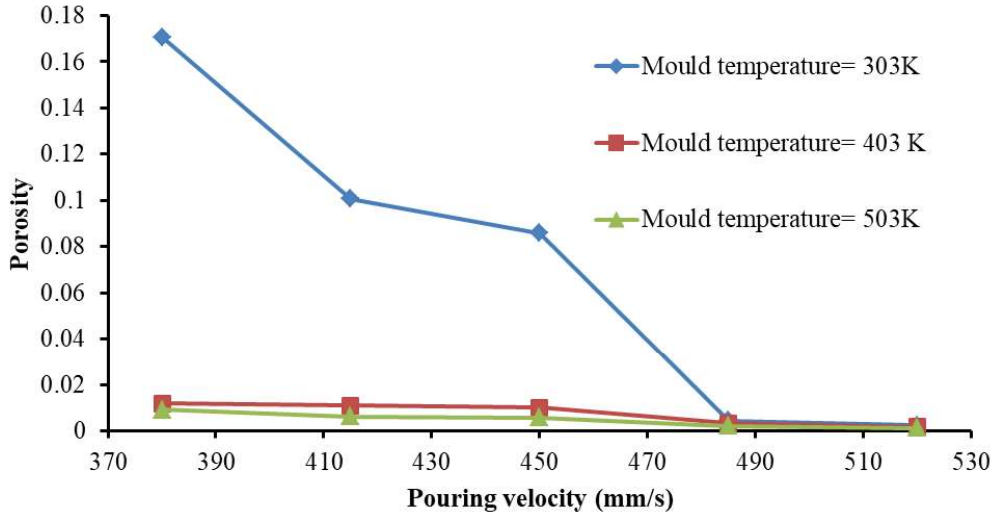

Figure 3.27: Variation of porosity with different pouring velocities and mould initial temperatures at 1003 K pouring temperature.

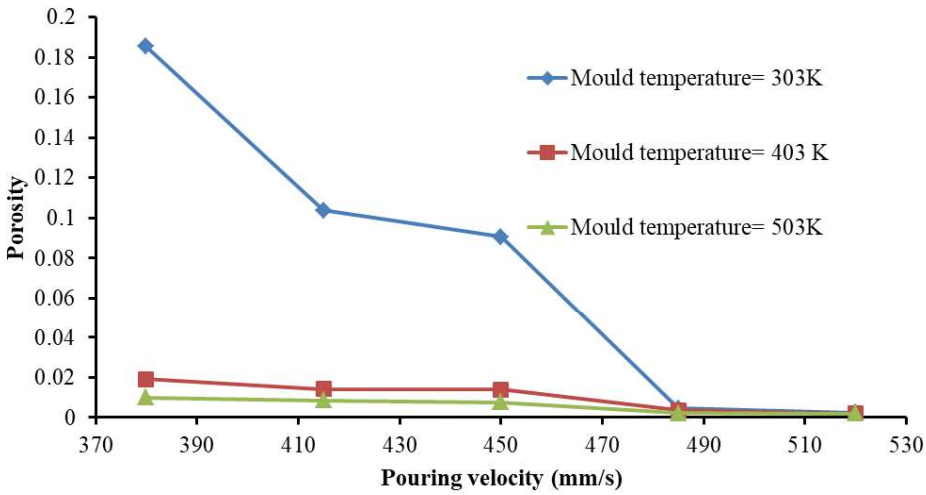

Figure 3.28: Variation of porosity with different pouring velocities and mould initial temperatures at 1033 K pouring temperature.

The comparative analysis is summarized in table 3.8. Porosity is found to decrease with an increase in mould temperature. It is due to the fluidity of the metal increases with mould temperature. When the mould is preheated to 403 K or 503 K, the porosity is relatively low. The rate of porosity decrease is high at pouring velocities of 385 mm/s and 415 mm/s, with the percentage of porosity decreasing by about 90% at all pouring temperatures. As the mould temperature increases from 303 K to 403 K, the rate of decrease in porosity decreases with increasing pouring velocity at a specific pouring temperature. For instance, at a pouring temperature of 983 K, the rate of porosity reduction is 93.67, 89.61, 85.86, 34.09, and 26.09 for 385, 415, 450, 485, and 520 mm/s pouring velocity respectively. The rate of porosity reduction decreases with increasing pouring velocity when the mould temperature is raised from 303 K to 403 K. This trend is observed for other pouring temperatures as well. Similarly as the mould temperature increases from 303 K to 503 K, the rate of decrease in porosity decreases with increasing pouring velocity at a specific pouring temperature. At pouring velocities of 485 mm/s and 520 mm/s, the porosity remains almost constant, regardless of the mould temperature.

Table 3.8: Effect of increase of mould temperature on porosity reduction with varying pouring velocity and temperature.

Pouring temperature (K)	Pouring Velocity (mm/s)	Percentage of porosity decrease from 303 K to 403 K mould temperature	Percentage of porosity decrease from 303 K to 503 K mould temperature
983	380	93.67	94.84
	415	89.61	94.31
	450	85.86	93.97
	485	34.09	54.55
	520	26.09	47.83
1003	380	93.02	94.67
	415	89.08	93.74
	450	88.34	93.24
	485	25.00	52.27
	520	25.00	45.83
1033	380	89.70	94.66
	415	86.32	91.71
	450	84.44	91.50
	485	17.78	48.89
	520	12.50	20.83

A general relationship between porosity and pouring temperature, pouring velocity, and mould initial temperature has been approximated using multiple linear regression analysis [207]. Regression analysis is a statistical technique for modelling the relationship between one or more independent variables and a dependent variable. The porosity can be approximated as:

$$Porosity = 0.2393 - 0.0005v_p + 0.0001T_p - 0.0003T_0$$

Where v_p is the pouring velocity [mm/s], T_p is the pouring temperature [K], and T_0 is the mould initial temperature [K].

3.5.7.2 Comparative Analysis of Solidification Time for Different Mould Temperatures

The average solidification times at mould temperatures of 303 K, 403 K, and 503 K are approximately 2 s, 2.47 s, and 3.26 s, respectively. A general relationship between solidification time and pouring temperature, pouring velocity, and mould temperature has been approximated using multiple linear regression analysis. The general solidification time (s) can be approximated as using multiple linear regression analysis:

$$t_s = -2.6741 - 0.0024\, v_p + 0.0038\, T_p + 0.0063\, T_0$$

3.6 Conclusions

The parameters relating to the porosity defect that impacts casting quality were investigated. The optimal pouring velocity is near 500 mm/s. When the velocity is close to 500 mm/s, it is seen that the porosity value is extremely low, and the porosity is almost constant regardless of the pouring temperature. The length of fully-filled solid aluminium from the base of the mould cavity rises with pouring velocity and reaches its maximum value close to 500 mm/s. Additionally, this length gradually increases with decreasing pouring temperature for a constant pouring velocity.

After solidification two layers are formed in the solidified casting, one of pure solid aluminium and the other of the solid aluminium-air mixture. This solid aluminium-air combination layer is responsible for porosity formation. The porosity gradually decreases with increasing pouring velocity for a fixed pouring temperature. The porosity is almost constant to a certain extent of temperature or gradually increases with increasing pouring temperature for a fixed pouring velocity at mould temperature 30°C. At others mould temperature (130°C and 230°C) the porosity increases with increasing pouring temperature for a fixed pouring velocity. A pouring temperature of 983 K showed the best results for getting low porous casting. Porosity has little dependence on pouring temperature rather than pouring velocity. The percentage of porosity

increases from zero value (adjacent to the 100% aluminium existing) to maximum value along the thickness of the casting. It achieves its highest value at the casting's top surface. Porosity is found to decrease with an increase in mould temperature. At pouring velocities of 485 mm/s and 520 mm/s, the porosity remains almost constant, regardless of the mould temperature. As the mould temperature increases, it is observed that the rate of decrease in porosity decreases with an increase in pouring velocity at a specific pouring temperature.

The aluminium mould filling and solidification have been studied, involving a two-phase system consisting of air and aluminium. This system has included a mixture of liquid and solid phases of aluminium. Throughout the study, the solidification front has been carefully observed and extensively analysed. The current observations indicate that increasing the preheating temperature of the mould leads to a greater quantity of molten aluminium in its liquid form. Conversely, reducing the preheating temperature of the mould decreases the amount of liquid aluminium present. Initially, solidification mainly occurs on the right side of the cavity. The behaviour of solidification plays a crucial role in determining the characteristics of hotspots. Hotspot zones are primarily found below the riser. High pouring velocities and low pouring temperatures have relatively small or negligible hotspot zones. The location of the hotspot and the impact of pouring velocity and temperature on the hotspot are largely independent of the initial temperature of the mould.

Furthermore, the solidification time exhibits a gradual decrease with increasing pouring velocity, whereas it increases gradually with higher pouring temperatures. On average, the solidification times are approximately 2 s, 2.47 s, and 3.26 s at mould temperatures of 303 K, 403 K, and 503 K, respectively.

CHAPTER 4: CONCLUSIONS AND FUTURE SCOPES

4.1 Conclusions

The research findings in the present thesis emphasize the importance of considering multiple parameters, such as pouring temperature, pouring velocity, and mould initial temperature, in order to accurately predict and control the solidification process and porosity formation in metal casting. It highlighted the need for a more practical model to specifically focus on porosity calculation and prediction. Overall, this study contributes to the understanding of solidification phenomena in metal casting and provides insights for optimizing the casting process to achieve high-quality castings with minimal porosity. It serves as a foundation for further research in developing more advanced models and techniques to address the complex nature of the casting process and improve the overall quality and efficiency of casting operations.

In Chapter 2, two one-dimensional casting solidification models have been simulated using the FORTRAN 95 programming software. The first model allowed for the calculation of the solidification front and solidification time, revealing an average solidification rate of 1.88 mm/s. The results indicate that rapid solidification occurs initially. However, the pouring temperature could not be altered during the simulation in the first model, which is a crucial parameter impacting both the solidification time and the position of the solidification front. The second model addressed this limitation by allowing variations in both pouring temperature and mould initial temperature. This model utilizes the error function and complementary error function to simulate the solidification process and calculate solidification times for different pouring temperatures and mould initial temperatures. The simulation results demonstrate that the solidification time increases with pouring temperature at a constant mould initial temperature, and it also increases with mould initial temperature at a constant pouring temperature. The solidification front is also calculated using this model, revealing initial rapid solidification followed by a relatively slow cooling process. The average solidification rate decreases with

increasing pouring temperature at a constant mould initial temperature and with increasing mould initial temperature at a constant pouring temperature.

However, it is important to note that in both models, pouring velocity is not varied, and the calculation of porosity is not included. Additional models would be required to predict or measure porosity formation in the casting. In Chapter 3, the investigation focuses on the parameters related to the porosity defect that impacts casting quality. The study reveals that the optimal pouring velocity is near 500 mm/s. At this velocity, the porosity value is extremely low and remains almost constant regardless of the pouring temperature. The length of fully-filled solid aluminium from the base of the mould cavity increases with pouring velocity, reaching its maximum value close to 500 mm/s. Additionally, this length gradually increases with decreasing pouring temperature for a constant pouring velocity.

The solidified casting consists of two layers, one of pure solid aluminium and the other of a solid aluminium-air mixture. The solid aluminium-air combination layer is responsible for porosity formation. The porosity gradually decreases with increasing pouring velocity at a fixed pouring temperature. It remains almost constant up to a certain temperature range and then gradually increases with further increases in pouring temperature for a fixed pouring velocity, except at a mould temperature of 30°C. At other mould temperatures (130°C and 230°C), the porosity increases with increasing pouring temperature for a fixed pouring velocity. A pouring temperature of 983 K shows the best results for obtaining a low-porosity casting, indicating that porosity has little dependence on pouring temperature compared to pouring velocity. The percentage of porosity increases from a zero value (adjacent to the 100% aluminium) to a maximum value along the thickness of the casting, with the highest value observed at the casting's top surface. Moreover, porosity is found to decrease with an increase in mould temperature. At pouring velocities of 485 mm/s and 520 mm/s, the porosity remains almost constant, regardless of the mould temperature. Additionally, it is observed that as the mould temperature increases, the rate of decrease in porosity decreases with increasing pouring velocity at a specific pouring temperature.

The study also examines the aluminium mould filling and solidification using a two-phase system comprising air and aluminium, as well as a mixture of liquid and solid phases of aluminium. The solidification front and the behaviour of hot spots are investigated. It is observed that initially, solidification mainly occurs on the right side of the cavity. The characteristics of the hot spot zones, which are primarily present below the riser, are determined by the solidification behaviour. Higher pouring velocities and lower pouring temperatures result in relatively small or negligible hot spot zones. Interestingly, the location of the hot spot and the influence of pouring velocity and pouring temperature on the hot spot are found to be almost independent of the initial temperature of the mould. This suggests that the hot spot behaviour is primarily influenced by the pouring parameters rather than the mould initial temperature or mould preheating temperature.

Furthermore, the study calculates the solidification time for different pouring parameters. It is observed that the solidification time gradually decreases as the pouring velocity increases, indicating a faster solidification process. Conversely, the solidification time increases gradually with increasing pouring temperature, suggesting a slower solidification process. The average solidification times at mould temperatures of 303 K, 403 K, and 503 K are approximately 2 s, 2.42 s, and 3.26 s, respectively. These findings highlight the significant impact of pouring velocity and temperature on the solidification time.

This research examines into the process of aluminium mould filling and solidification using two-phase systems and a mixture of liquid and solid phases of aluminium. The study utilizes simulation models to analyse the solidification process, solidification time, and porosity. The results provide insights into the effects of parameters, such as pouring velocity, pouring temperature, and mould temperature, on porosity formation, solidification time, and hot spot behaviour. These findings emphasize the significance of optimizing these parameters to minimize porosity defects and achieve efficient solidification processes.

4.2 Future Scopes

This thesis focuses on the permanent mould casting of pure aluminium (99.9% pure aluminium) using a steel mould, utilizing a computational fluid dynamics (CFD) model to analyse various casting parameters. While this study provides valuable insights into porosity, solidification time, solidification front, and the length of aluminium metal, there are several possibilities for future research and expansion in this field.

Firstly, future studies may explore the casting of other metals using similar computational models. The extension of this research to different metal alloys can provide a comparative analysis of their solidification behaviours, porosity formation, and casting quality. In addition to exploring different metals, future research can also investigate alternative gating systems. This thesis focuses on the top gating system, but other gating designs such as bottom gating or side gating offer potential for optimization of casting parameters and reduction of porosity defects. By comparing and analysing the effects of different gating systems on porosity formation and casting quality, researchers can identify the most efficient and effective gating design for specific applications.

Furthermore, future studies can delve into the optimization of casting parameters for other defects beyond porosity. While this thesis primarily addresses porosity defects, there are various other defects that can affect casting quality, such as shrinkage, misruns, and cold shuts. By expanding the scope of analysis to include these defects, researchers can develop comprehensive models and optimize casting parameters to minimize or eliminate these defects. Additionally, exploration of other mould materials may also be a possibility for future research.

REFERENCES

[1] T. R. Rao, Metal Casting: Principles and Practice, New Age International, 2007.

[2] P. Lynch, C. R. Hasbrouck, J. Wilck, M. Kay and G. Manogharan, "Challenges and Opportunities To Integrate the Oldest and Newest Manufacturing Processes: Metal Casting and Additive Manufacturing," *Rapid Prototyping Journal,* vol. 26, no. 6, pp. 1145-1154, 2020.

[3] C. M. Cheah, C. K. Chua, C. W. Lee, C. Feng and K. Totong, "Rapid Prototyping and Tooling Techniques: A Review of Applications for Rapid Investment Casting," *The International Journal of Advanced Manufacturing Technology,* vol. 25, pp. 308-320, 2005.

[4] M. A. A. Khan and A. K. Sheikh, "A Comparative Study of Simulation Software for Modelling Metal Casting Processes," *International Journal of Simulation Modelling,* vol. 17, no. 2, pp. 197-209, 2018.

[5] H. Haferkamp, R. Boehm, U. Holzkamp, C. Jaschik, V. Kaese and M. Niemeyer, "Alloy Development, Processing and Applications in Magnesium Lithium Alloys," *Materials Transactions,* vol. 42, no. 7, pp. 1160-1166, 2001.

[6] T. Dursun and C. Soutis, "Recent Developments in Advanced Aircraft Aluminium Alloys," *Materials & Design (1980-2015),* vol. 56, pp. 862-871, 2014.

[7] M. Tiryakioğlu, P. Yousefian and P. D. Eason, "Quantification of Entrainment Damage in A356 Aluminum Alloy Castings," *Metallurgical and Materials Transactions A,* vol. 49, pp. 5815-5822, 2018.

[8] S. Zhang, Z. Xu and Z. Wang, "Numerical Modeling and Simulation of Water Cooling-

Controlled Solidification for Aluminum Alloy Investment Casting," *The International Journal of Advanced Manufacturing Technology,* vol. 91, no. 1, pp. 763-770, 2017.

[9] N. Souissi, S. Souissi, C. Le Niniven, M. B. Amar, C. Bradai and F. Elhalouani, "Optimization of Squeeze Casting Parameters for 2017 a Wrought Al Alloy using Taguchi Method," *Metals,* vol. 4, no. 2, pp. 141-154, 2014.

[10] G. Krauss, "Martensite in Steel: Strength and Structure," *Materials science and engineering: A,* vol. 273, pp. 40-57, 1999.

[11] K. N. Seetharamu, R. Paragasam, G. A. Quadir, Z. A. Zainal, B. S. Prasad and T. Sundararajan, "Finite Element Modelling of Solidification Phenomena," *Sadhana,* vol. 26, pp. 103-120, 2001.

[12] L. M. Galantucci and L. Tricarico, "A Computer-Aided Approach for the Simulation of the Directional-Solidification Process for Gas Turbine Blades," *Journal of Materials Processing Technology,* vol. 77, no. 1-3, pp. 160-165, 1998.

[13] S. Mohapatra, H. Sarangi and U. K. Mohanty, "Effect of Processing Factors on the Characteristics of Centrifugal Casting," *Manufacturing Review,* vol. 7, p. 26, 2020.

[14] J. M. Boileau, J. W. Zindel and J. E. Allison, "The Effect of Solidification Time on the Mechanical Properties in A Cast A356-T6 Aluminum Alloy," *SAE transactions,* pp. 63-74, 1997.

[15] J. Suthar, J. Persis and R. Gupta, "Critical Parameters Influencing the Quality of Metal Castings: A Systematic Literature Review," *International Journal of Quality & Reliability Management,* vol. 40, no. 1, pp. 53-82, 2023.

[16] M. M. K. Basah and A. Saleh, "Design of Pouring Stand With Adjustable Pouring Height for Metal Moulding Flask in Green Sand-Casting Application," *Progress in Engineering*

Application and Technology, vol. 2, no. 2, pp. 770-779, 2021.

[17] A. Jahangiri, S. P. H. Marashi, M. Mohammadaliha and V. Ashofte, "The Effect of Pressure and Pouring Temperature on the Porosity, Microstructure, Hardness and Yield Stress of AA2024 Aluminum Alloy," *Journal of Materials Processing Technology,* vol. 245, pp. 1-6, 2017.

[18] L. Wang, T. Nguyen, G. Savage and C. Davidson, "Thermal and Flow Modelling of Ladling and Injection in High-Pressure Die Casting Process," *International Journal of Cast Metals Research,* vol. 16, no. 4, pp. 409-417, 2003.

[19] K. M. Daws, Z. I. Al-Dawood and S. H. Al-Kabi, "Selection of Metal Casting Processes: A Fuzzy Approach," *Jordan Journal of Mechanical and Industrial Engineering,* vol. 2, no. 1, 2008.

[20] J. Linder, M. Axelsson and H. Nilsson, "The Influence of Porosity on the Fatigue Life for Sand and Permanent Mould Cast Aluminium," *International Journal of Fatigue,* vol. 28, no. 12, pp. 1752-1758, 2006.

[21] S. Vignesh, "A Review of Advanced Casting Techniques," *Research Journal of Engineering and Technology,* vol. 8, no. 4, pp. 440-446, 2017.

[22] J. L. Jorstad, "Permanent Mould: Casting Processes," *Advanced Materials & Processes,* vol. 166, no. 4, pp. 30-34, 2008.

[23] S. Otarawanna and A. K. Dahle, "Casting of Aluminium Alloys," in *Fundamentals of aluminium metallurgy*, Woodhead Publishing, 2011, pp. 141-154.

[24] F. P. Peters, "Mass Production Metal-Forms," *Scientific American,* vol. 170, no. 5, pp. 199-201, 1944.

[25] R. W. Ruddle, “The Running and Gating of Sand Casting,” *Institute of Metals Monograph and Report Series,* vol. 19, 1956.

[26] J. Szekely, J. W. Evans and J. K. Brimacombe, The Mathematical and Physical Modeling of Primary Metals Processing Operations, vol. 261, John Wiley & Sons, Inc., 1988.

[27] D. Ceotto and F. Miani, “Empirical Model for the Estimation of Thermophysical Properties of Liquid Metal Alloys,” *High Temperature,* vol. 52, no. 3, pp. 385-389, 2014.

[28] B. Hernandez-Morales and A. Mitchell, “Review of Mathematical Models of Fluid Flow, Heat Transfer, and Mass Transfer in Electroslag Remelting Process,” *Ironmaking & steelmaking,* vol. 26, no. 6, pp. 423-438, 1999.

[29] J. Suthar, J. Persis and R. Gupta, “Analytical Modeling of Quality Parameters in Casting Process–Learning-Based Approach,” *International Journal of Quality & Reliability Management,* Vols. ahead-of-print, 2022.

[30] L. Zhang, “Computational Fluid Dynamics Modeling: Application to Transport Phenomena during the Casting Process,” *JOM,* vol. 64, no. 9, pp. 1059-1062, 2012.

[31] D. M. Stefanescu, Science and Engineering of Casting Solidification, Springer, 2015.

[32] H. Bayani, S. M. H. Mirbagheri, M. Barzegari and S. Firoozi, “Simulation of Unconstrained Solidification of A356 Aluminum Alloy on Distribution of Micro/Macro Shrinkage,” *Journal of Materials Research and Technology,* vol. 3, no. 1, pp. 55-70, 2014.

[33] D. Chen, J. Wang and C. Zhang, “Coupling Phase-Field Model and CFD for Hot Cracking Predictions of Al-Li Alloys,” *Computational Materials Science,* vol. 192, p. 110361, 2021.

[34] M. Rappaz, “Modeling and Characterization of Grain Structures and Defects in

Solidification," *Current Opinion in Solid State and Materials Science,* vol. 20, no. 1, pp. 37-45, 2016.

[35] MAGMA 5., "Magmasoft," 2016.

[36] M. Widad and D. K. Pratiwi, *Simulasi Pengecoran Aluminium Skrap Metode Gravity Die Casting Menggunakan Esi Procast (Doctoral dissertation),* Sriwijaya University, 2022.

[37] J. Dańko, R. Dańko and J. Lelito, "Modelling of Flow Phenomena in the Process of Filling the Model Die Mould-An Application of the Novaflow Program," *Archives of Foundry Engineering,* vol. 8, no. 4, pp. 31-36, 2008.

[38] P. H. Huang, J. Y. Luo, S. C. Hung, C. J. Lin and H. H. Cheng, "Optimal Pouring System Design for Investment Casting of Cladding Thin-Plate Heater using Metallic Mold Flow Analyses," *Applied Mechanics and Materials,* vol. 627, pp. 46-49, 2014.

[39] A. N. S. Y. S. CFX-Solver, Theory Guide Release ll, 2006.

[40] J. E. Matsson, An Introduction to ANSYS Fluent 2022, SDC Publications, 2022.

[41] H. Li and S. S. Mulay, Meshless Methods and their Numerical Properties, CRC press, 2013.

[42] G. R. Liu, Meshfree Methods: Moving Beyond the Finite Element Method, CRC press, 2009.

[43] G. Kosec and B. Šarler, "Simulation of Macrosegregation with Mesosegregates in Binary Metallic Casts By a Meshless Method," *Engineering analysis with boundary elements,* vol. 45, pp. 36-44, 2014.

[44] P. W. Cleary, J. Ha, M. Prakash and T. Nguyen, "3D SPH Flow Predictions and Validation for High Pressure Die Casting of Automotive Components," *Applied*

Mathematical Modelling, vol. 30, no. 11, pp. 1406-1427, 2006.

[45] P. W. Cleary, M. Prakash, J. Ha, N. Stokes and C. Scott, "Smooth Particle Hydrodynamics: Status and Future Potential," *Progress in Computational Fluid Dynamics, an International Journal,* vol. 7, no. 2-4, pp. 70-90, 2007.

[46] M. Jolly and L. Katgerman, "Modelling of Defects in Aluminium Cast Products," *Progress in Materials Science,* vol. 123, p. 100824, 2022.

[47] Y. Li, H. Li, L. Katgerman, Q. Du, J. Zhang and L. Zhuang, "Recent Advances in Hot Tearing during Casting of Aluminium Alloys," *Progress in Materials Science,* vol. 117, p. 100741, 2021.

[48] A. Mortensen and S. Suresh, "Functionally Graded Metals and Metal-Ceramic Composites: Part 1 Processing," *International materials reviews,* vol. 40, no. 6, pp. 239-265, 1995.

[49] S. Namchanthra, C. Suvanjumrat, W. Chookaew, W. Wijitdamkerng and M. Promtong, "A CFD Investigation into Molten Metal Flow and its Solidification under Gravity Sand Moulding in Plumbing Components," *GEOMATE Journal,* vol. 22, no. 92, pp. 100-108, 2022.

[50] D. R. Gunasegaram, D. J. Farnsworth and T. T. Nguyen, "Identification of Critical Factors Affecting Shrinkage Porosity in Permanent Mold Casting using Numerical Dimulations based on Design of Experiments," *Journal of materials processing technology,* vol. 209, no. 3, pp. 1209-1219, 2009.

[51] S. Ge, S. Chang, T. Wang, L. E. Calzado, M. Isac, J. Kozinski and R. I. Guthrie, "Mathematical modeling and microstructure analysis of low carbon steel strips produced by horizontal single belt casting (HSBC)," *Metallurgical and Materials Transactions B,*

vol. 47, 2016.

[52] M. I. H. Siddiqui, A. Albaqami, L. Arifudin, K. Alluhydan and I. A. Alnaser, “Simulation of Inclusion Particle Motion Behavior under Interfacial Tension in Continuous Casting Mold,” *Materials,* vol. 15, no. 21, p. 7458, 2022.

[53] S. Chakravarti and S. Sen, “An Investigation on the Solidification and Porosity Prediction in Aluminium Casting Process,” *Journal of Engineering and Applied Science,* vol. 70, no. 1, pp. 1-24, 2023.

[54] M. E. Glicksman, Principles of Solidification: An Introduction to Modern Casting and Crystal Growth Concepts, Springer Science & Business Media, 2010.

[55] M. Zeng, L. Li, X. Zhu and L. Fu, “A Liquid Metal Reaction System for Advanced Material Manufacturing,” *Accounts of Materials Research,* vol. 2, no. 8, pp. 669-680, 2021.

[56] Y. Shibuta, S. Sakane, E. Miyoshi, S. Okita, T. Takaki and M. Ohno, “Heterogeneity in Homogeneous Nucleation from Billion-Atom Molecular Dynamics Simulation of Solidification of Pure Metal,” *Nature communications,* vol. 8, no. 1, p. 10, 2017.

[57] M. M. Kirka, P. Nandwana, Y. Lee and R. R. Dehoff, “Solidification and Solid-State Transformation Sciences in Metals Additive Manufacturing,” *Scripta Materialia,* vol. 125, pp. 130-134, 2017.

[58] J. J. Valencia and P. N. Quested, “Thermophysical Properties,” in *Modeling for casting and solidification processing*, CRC press, 2001, pp. 189-237.

[59] M. Şimşir, L. C. Kumruoğlu and A. Özer, “An Investigation Into Stainless-Steel/Structural-Alloy-Steel Bimetal Produced by Shell Mould Casting,” *Materials & design,* vol. 30, no. 2, pp. 264-270, 2009.

[60] M. V. Gielen, R. de Ruiter, R. B. Koldeweij, D. Lohse, J. H. Snoeijer and H. Gelderblom, "Solidification of Liquid Metal Drops during Impact," *Journal of fluid mechanics,* vol. 883, p. A32, 2020.

[61] R. G. Bhandare and P. M. Sonawane, "Preparation of Aluminium Matrix Composite by using Stir Casting Method," *International Journal of Engineering and Advanced Technology (IJEAT),* vol. 3, no. 3, pp. 61-65, 2013.

[62] B. T. Bekele, J. Bhaskaran, S. D. Tolcha and M. Gelaw, "Simulation and Experimental Analysis of Re-Design the Faulty Position of the Riser to Minimize Shrinkage Porosity Defect," *Materials Today: Proceedings,* vol. 59, pp. 598-604, 2022.

[63] N. Hebsur and S. Mangshetty, "Casting Simulation for Sand Casting of Flywheel," *International Journal of Research in Advent Technology,* vol. 2, no. 8, pp. 82-86, 2014.

[64] H. Iqbal, A. K. Sheikh, A. Al-Yousef and M. Younas, "Mold Design Optimization for Sand Casting of Complex Geometries using Advance Simulation Tools," *Materials and Manufacturing Processes,* vol. 27, no. 7, pp. 775-785, 2012.

[65] J. K. Brimacombe and K. Sorimachi, "Crack Formation in the Continuous Casting of Steel," *Metallurgical transactions B,* vol. 8, pp. 489-505, 1977.

[66] P. X. Fu, X. H. Kang, Y. C. Ma, K. Liu, D. Z. Li and Y. Y. Li, "Centrifugal Casting of Tial Exhaust Valves," *Intermetallics,* vol. 16, no. 2, pp. 130-138, 2008.

[67] F. M. Najjar, B. G. Thomas and D. E. Hershey, "Numerical Study of Steady Turbulent Flow Through Bifurcated Nozzles in Continuous Casting," *Metallurgical and Materials Transactions B,* vol. 26, pp. 749-765, 1995.

[68] W. Rodi, Turbulence Models and Their Application in Hydraulics, CRC Press, 1993.

[69] C. Foias, D. D. Holm and E. S. Titi, “The Navier–Stokes-Alpha Model of Fluid Turbulence,” *Physica D: Nonlinear Phenomena,* vol. 152, pp. 505-519, 2001.

[70] G. A. Birajdar, “Numerical Solution of Time Fractional Navier-Stokes Equation by Discrete Adomian Decomposition Method,” *Nonlinear Engineering,* vol. 3, no. 1, pp. 21-26, 2014.

[71] F. R. Menter, “Review of the Shear-Stress Transport Turbulence Model Experience from an Industrial Perspective,” *International journal of computational fluid dynamics,* vol. 23, no. 4, pp. 305-316, 2009.

[72] A. Ramadhan Al-Obaidi, “Effects of Different Turbulence Models on Three-Dimensional Unsteady Cavitating Flows in the Centrifugal Pump and Performance Prediction,” *International Journal of Nonlinear Sciences and Numerical Simulation,* vol. 20, no. 3-4, pp. 487-509, 2019.

[73] G. Alfonsi, “Reynolds-Averaged Navier–Stokes Equations for Turbulence Modeling,” *Applied Mechanics Reviews,* vol. 62, no. 4, 2009.

[74] S. M. Salim, K. C. Ong and S. C. Cheah, “Comparison of RANS, URANS and LES in the Prediction of Airflow and Pollutant Dispersion,” in *Proceedings of the world congress on engineering and computer science*, San Francisco, USA, 2011.

[75] C. Mockett, M. Fuchs and F. Thiele, “Progress in DES for Wall-Modelled LES of Complex Internal Flows,” *Computers & Fluids,* vol. 65, pp. 44-55, 2012.

[76] R. H. Bush, T. S. Chyczewski, K. Duraisamy, B. Eisfeld, C. L. Rumsey and B. R. Smith, “Recommendations for Future Efforts in RANS Modeling and Simulation,” in *In AIAA scitech 2019 forum*, San Diego, United States, 2019.

[77] A. J. Lew, G. C. Buscaglia and P. M. Carrica, “A Note on the Numerical Treatment of the

K-Epsilon Turbulence Model," *International Journal of Computational Fluid Dynamics,* vol. 14, no. 3, pp. 201-209, 2001.

[78] A. A. Troshko and Y. A. Hassan, "A Two-Equation Turbulence Model of Turbulent Bubbly Flows," *International Journal of Multiphase Flow,* vol. 27, no. 11, pp. 1965-2000, 2001.

[79] G. Alvarez, P. E. Bournet and D. Flick, "Two-Dimensional Simulation of Turbulent Flow and Transfer through Stacked Spheres," *International Journal of Heat and Mass Transfer,* vol. 46, no. 13, pp. 2459-2469, 2003.

[80] N. K. Sharma, S. K. Dewangan and P. K. Gupta, "Numerical Simulation of Three-Dimensional Circular Free Turbulent Jet Flow using Different Reynolds Average Navier-Stokes Turbulence Models," *Computational Thermal Sciences: An International Journal,* vol. 15, no. 3, 2023.

[81] V. Haroutunian and M. S. Engelman, "On Modeling Wall-Bound Turbulent Flows Using Specialized Near-Wall Finite Elements and the Standard K-Epsilon Turbulence Model," in *Advances in Numerical Simulation of Turbulent Flows*, New York, American Society of Mechanical Engineers, 1991, pp. 97-105.

[82] R. M. McMullen, M. C. Krygier, J. R. Torczynski and M. A. Gallis, "Navier-Stokes Equations Do Not Describe the Smallest Scales of Turbulence in Gases," *Physical Review Letters,* vol. 128, no. 11, p. 114501, 2022.

[83] U. Schumann and T. Gerz, "Turbulent Mixing in Stably Stratified Shear Flows," *Journal of Applied Meteorology and Climatology,* vol. 34, no. 1, pp. 33-48, 1995.

[84] V. Yakhot and S. A. Orszag, "Renormalization Group Analysis of Turbulence. I. Basic Theory," *Journal of scientific computing,* vol. 1, no. 1, pp. 3-51, 1986.

[85] T. H. Shih, W. W. Liou, A. Shabbir, Z. Yang and J. Zhu, "A New K-ϵ Eddy Viscosity Model for High Reynolds Number Turbulent Flows," *Computers & fluids,* vol. 24, no. 3, pp. 227-238, 1995.

[86] Q. Chen, "Comparison of Different K-E Models for Indoor Air Flow Computations," *Numerical Heat Transfer, Part B Fundamentals,* vol. 28, no. 3, pp. 353-369, 1995.

[87] A. Escue and J. Cui, "Comparison of Turbulence Models in Simulating Swirling Pipe Flows," *Applied Mathematical Modelling,* vol. 34, no. 10, pp. 2840-2849, 2010.

[88] G. C. Papageorgakis and D. N. Assanis, "Comparison of Linear and Nonlinear RNG-Based K-Epsilon Models for Incompressible Turbulent Flows," *Numerical Heat Transfer: Part B: Fundamentals,* vol. 35, no. 1, pp. 1-22, 1999.

[89] M. A. Waheed, G. C. Nzebuka and C. C. Enweremadu, "Potent Turbulence Model for the Computation of Temperature Distribution and Eddy Viscosity Ratio in a Horizontal Direct-Chill Casting," *Numerical Heat Transfer, Part A: Applications,* vol. 79, no. 4, p. 294–310, 2020.

[90] J. Hashim, L. Looney and M. S. J. Hashmi, "Metal Matrix Composites: Production by the Stir Casting Method," *Journal of materials processing technology,* vol. 92, pp. 1-7, 1999.

[91] R. Monroe, "Porosity in Castings," *AFS Transactions,* vol. 113, pp. 519-546, 2005.

[92] N. Qosim, A. M. Mufarrih, A. Sai'in, A. H. Firdaus, F. A. Fina Andika, R. Monasari and Z. F. Emzain, "Effect of Moisture Content of Green Sand on the Casting Defects," *Journal of Applied Engineering and Technological Science (JAETS),* vol. 2, no. 1, pp. 1-6, 2020.

[93] J. L. Christian, J. D. Forest and M. D. Weisinger, "Aluminum-Boron Composites for Aerospace Structures," General Dynamics Corp., San Diego, Calif., 1970.

[94] H. Nunes, O. Emadinia, M. F. Vieira and A. Reis, “Low-And High-Pressure Casting Aluminum Alloys: A Review,” in *Recent Advancements in Aluminum Alloys* , S. Rajendrachari, Ed., IntechOpen, 2023.

[95] I. W. Donald, “Preparation, Properties and Chemistry of Glass-and Glass-Ceramic-to-Metal Seals and Coatings,” *Journal of materials science,* vol. 28, pp. 2841-2886, 1993.

[96] M. Łagiewka and C. Kolmasiak, “The Porosity of Tin Bronze Castings,” *Metalurgija,* vol. 62, no. 1, pp. 155-157, 2023.

[97] L. Elmquist and A. Diószegi, “Shrinkage Porosity and its Relation to Solidification Structure of Grey Cast Iron Parts,” *International Journal of Cast Metals Research,* vol. 23, no. 1, pp. 44-50, 2010.

[98] J. A. Taylor, “Metal-Related Castability Effects in Aluminium Foundry Alloys,” *Cast Metals,* vol. 8, no. 2, pp. 225-252, 1996.

[99] A. Du Plessis, I. Yadroitsava and I. Yadroitsev, “Effects of Defects on Mechanical Properties in Metal Additive Manufacturing: A Review Focusing on X-Ray Tomography Insights,” *Materials & Design,* vol. 187, p. 108385, 2020.

[100] T. Haskel, G. O. Verran, R. Barbieri, J. da Silva and D. Novak, “Effects of Strontium Addition and T6 Heat Treatment on Uniaxial Fatigue of A356 Aluminum Alloy: Fatigue Life and Cyclic Behavior,” *Fatigue & Fracture of Engineering Materials & Structures,* vol. 45, no. 8, pp. 2159-2173, 2022.

[101] S. Chakravarti and S. Sen, “Study on the Behaviour of Surface Wear and Friction for a Pure Aluminium Casting Product using Permanent Mould,” *Key Engineering Materials,* vol. 944, pp. 41-49, 2023.

[102] A. Samuel, Y. Zedan, H. Doty, V. Songmene and F. H. Samuel, “A Review Study on the

Main Sources of Porosity in Al-Si Cast Alloys," *Advances in Materials Science and Engineering,* vol. 2021, p. 42370, 2021.

[103] C. D. Ridgeway, K. Ripplinger, D. Detwiler and A. A. Luo, "Prediction of Entrained Oxide Inclusions and Oxide Induced Defects during Directional Flow in Aluminum Casting," *AFS Transactions,* vol. 128, pp. 59-70, 2020.

[104] E. Pagone, C. Jones, J. Forde, W. Shaw, M. Jolly and K. Salonitis, "Defect Minimisation in Vacuum-Assisted Plaster Mould Investment Casting through Simulation of High-Value Aluminium Alloy Components," in *TMS Annual Meeting & Exhibition*, Switzerland, 2023.

[105] G. A. Hodbe and B. R. Shinde, "Design and Simulation of LM 25 Sand Casting for Defect Minimization," *Materials Today: Proceedings,* vol. 5, no. 2, pp. 4489-4497, 2018.

[106] A. Baghani, A. Kheirabi, A. Bahmani and H. Khalilpour, "Reducing Melt Surface Turbulence by Employing Surge and Filter in a Conventional Non-Pressurizing Gating System: Simulation and Experiment," *Archives of Metallurgy and Materials,* vol. 66, no. 2, pp. 397-405, 2021.

[107] J. Hardy, D. Cheneler, P. Heasman and A. Dodd, "Review of Ceramic Mold Casting of Metal-based Materials via the Shaw Process," *Engineering Archive,* 2023.

[108] A. Sola and A. Nouri, "Microstructural Porosity in Additive Manufacturing: The Formation and Detection of Pores in Metal Parts Fabricated by Powder Bed Fusion," *Journal of Advanced Manufacturing and Processing,* vol. 1, no. 3, p. e10021, 2019.

[109] M. Divandari and J. Campbell, *Mechanisms of Bubble Damage in Castings (Doctoral Dissertaion),* University of Birmingham, 2001.

[110] A. Raj, S. Ram Kishore, L. Jose, A. K. Karn, U. Chadha and S. K. Selvaraj, "A Survey of

Electromagnetic Metal Casting Computation Designs, Present Approaches, Future Possibilities, and Practical Issues," *The European Physical Journal Plus,* vol. 136, pp. 1-33, 2021.

[111] P. Homayonifar, R. Babaei, E. Attar, S. Shahinfar and P. Davami, "Numerical Modeling of Splashing and Air Entrapment in High-Pressure Die Casting," *The International Journal of Advanced Manufacturing Technology,* vol. 39, pp. 219-228, 2008.

[112] R. M. Pillai, "Hiping--A Potent Post Casting Treatment for High Integrity Aluminium Castings," *Foundry Trade Journal,* vol. 181, no. 3648, pp. 298-301, 2007.

[113] R. P. Taylor, J. Shenefelt, J. T. Berry and R. Luck, "Comparison and Criticism of Casting Criteria Functions," *Transactions of the American Foundry Society,* vol. 110, no. 1, pp. 315-330, 2002.

[114] P. Esser, C. Schankies, V. Khalajzadeh and C. Beckermann, "Advanced Modeling of Shrinkage Porosity in Castings," in *IOP Conference Series: Materials Science and Engineering*, 2020.

[115] S. Li, K. Mine, S. Sanakanishi and K. Anzai, "Quantitative Prediction Method for Shrinkage Porosity Considering Molten Metal Supply by Pressure in Squeeze Casting," *Materials transactions,* vol. 48, no. 8, pp. 2186-2193, 2007.

[116] S. Mozammil, J. Karloopia and P. Jha, "Investigation of Porosity in Al Casting," *Materials Today: Proceedings,* vol. 5, no. 9, p. 17270–17276, 2018.

[117] J. D. Zhu, S. L. Cockcroft and D. M. Maijer, "Modeling of Microporosity Formation in A356 Aluminum Alloy Casting," *Metallurgical and materials transactions A,* vol. 37, pp. 1075-1085, 2006.

[118] L. Liu, A. M. Samuel, F. H. Samuel, H. W. Doty and S. Valtierra, "Influence of Oxides on

Porosity Formation in Sr-Treated Al-Si Casting Alloys," *Journal of materials science,* vol. 38, pp. 1255-1267, 2003.

[119] S. Li, K. Mine, S. Sanakanishi and K. Anzai, "To Develop a Quantitative Method for Predicting Shrinkage Porosity in Squeeze Casting," *China Foundry,* vol. 6, no. 1, pp. 53-56, 2009.

[120] C. Gu and A. A. Luo, "Three-Dimensional Numerical Simulation of Solidification Microporosity and Microstructure of Aluminum Alloys," in *IOP Conference Series: Materials Science and Engineering*, 2020.

[121] A. Zhang, Z. Guo, Q. Wang and S. Xiong, "Multiphase-Field Modelling of Hydrogen Pore Evolution during Alloy Solidification," in *IOP Conference Series: Materials Science and Engineering*, 2020.

[122] A. Hamasaiid, M. S. Dargusch and G. Dour, "The Impact of the Casting Thickness on the Interfacial Heat Transfer and Solidification of the Casting," *Journal of Manufacturing Processes,* vol. 47, pp. 229-237, 2019.

[123] E. Fiorese, F. Bonollo, G. Timelli, L. Arnberg and E. Gariboldi, "New Classification of Defects and Imperfections for Aluminum Alloy Castings," *International Journal of Metalcasting,* vol. 9, pp. 55-66, 2015.

[124] F. Bonollo, E. Fiorese, G. Timelli, L. Arnberg and A. R. Adamane, "Stacast Project: From a Survey of European Aluminium Alloys Foundries to New Standards on Defect Classification and on Mechanical Potential of Casting Alloys," in *71st World Foundry Congress*, Bilbao, Spain, 2014.

[125] M. A. El-Sayed, H. Hassanin and K. Essa, "Effect of Casting Practice on the Reliability of Al Cast Alloys," *International Journal of Cast Metals Research,* vol. 29, no. 6, pp. 350-

354, 2016.

[126] I. P. Nanda, M. H. Jahare, M. H. Idris, S. B. Kumar, M. H. Hassim and A. Arafat, “Effect of Pouring Temperatures on Porosity and Mechanical Properties of Gravity Die Casting Magnesium Alloy,” in *IOP Conference Series: Materials Science and Engineering*, 2019.

[127] Z. Ignaszak and J. Hajkowski, “Contribution to the Identification of Porosity Type in Alsicu High-Pressure-Die-Castings by Experimental and Virtual Way,” *Archives of foundry engineering,* vol. 15, 2015.

[128] S. Thanabumrungkul, W. Jumpol, R. Canyook, N. Meemongkol and J. Wannasin, “Characterization of Microstructure and Shrinkage Porosity of a Semi-Solid Metal Slurry in Gravity Die Casting,” *In Solid State Phenomena,* vol. 285, pp. 161-166, 2019.

[129] D. Dispinar, S. Akhtar, A. Nordmark, F. Syvertsen, M. Di Sabatino and L. Arnberg, “Correlation Between Mechanical Properties and Porosity Distribution of A356 in Gravity Die Casting and Low Pressure Die Casting,” *Advanced materials research,* vol. 445, pp. 283-288, 2012.

[130] J. T. Anderson, D. T. Gethin, R. W. Lewis and J. T. Cross, “Experimental Investigation and Finite Element Modelling in Gravity Die Casting,” *Proceedings of the Institution of Mechanical Engineers, Part B: Journal of Engineering Manufacture,* vol. 211, no. 2, pp. 93-107, 1997.

[131] K. D. Carlson, Z. Lin, R. Hardin, C. Beckermann, G. Mazurkevich and M. Schneider, “Modeling of Porosity Formation and Feeding Flow in Steel Casting,” in *Proceedings of the 56th SFSA technical and operating conference*, Chicago, 2002.

[132] A. Kermanpur, S. Mahmoudi and A. Hajipour, “Numerical Simulation of Metal Flow and Solidification in the Multi-Cavity Casting Moulds of Automotive Components,” *Journal*

of Materials Processing Technology, vol. 206, no. 1-3, pp. 62-68, 2008.

[133] D. Dhaneswara, J. F. Fatriansyah and A. R. Basa, "A Comparative Study between the Addition of NH4Cl and Kcl in Nano3 and Naf-Based Degassers in Aluminum Casting," in *IOP Conference Series: Materials Science and Engineering*, 2019.

[134] S. Chakravarti and S. Sen, "Simulation of Commencement and Size of the Hot Spot in Permanent Mould Casting," *Key Engineering Materials,* vol. 941, pp. 11-18, 2023.

[135] K. Kurtulus, A. Bolatturk, A. Coskun and B. Gürel, "An Experimental Investigation of the Cooling and Heating Performance of a Gravity Die Casting Mold with Conformal Cooling Channels," *Applied thermal engineering,* vol. 194, p. 117105, 2021.

[136] R. W. Lewis and R. S. Ransing, "A Correlation to Describe Interfacial Heat Transfer during Solidification Simulation and its Use in the Optimal Feeding Design of Castings," *Metallurgical and Materials Transactions B,* vol. 29, pp. 437-448, 1998.

[137] A. Grill, K. Sorimachi and J. K. Brimacombe, "Heat Flow, Gap Formation and Break-Outs in the Continuous Casting of Steel Slabs," *Metallurgical Transactions B,* vol. 7, pp. 177-189, 1976.

[138] B. Ravi and M. N. Srinivasan, "Casting Solidification Analysis by Modulus Vector Method," *International Journal of Cast Metals Research,* vol. 9, no. 1, pp. 1-7, 1996.

[139] J. Zhou, M. Wang, Y. Yin, X. Shen, X. Chen, W. Li and D. Zhang, "Feed Paths and Hot Spots Computation based on a Time Gradient Method in Casting," *The International Journal of Advanced Manufacturing Technology,* vol. 93, pp. 261-272, 2017.

[140] W. E. Warriner and C. A. Monroe, "Locating Solidification Hot Spots and Feeder Positions in Casting Geometries by Image Analysis," *International Journal of Metalcasting,* vol. 12, pp. 224-234, 2018.

[141] W. Li and J. Cui, “A New Method for Quickly Locating the Hot Spots in Solidification Simulation of Complicated Castings,” *International Journal of Cast Metals Research,* vol. 15, no. 4, pp. 319-323, 2003.

[142] Y. Xu, K. Zhang, H. L. Zheng, Y. C. Sun and X. L. Tian, “An Improved Geometric Model to Predict Hot Spots of Castings,” *Materials Science Forum,* vol. 689, pp. 29-32, 2011.

[143] D. M. Stefanescu, R. Suarez and S. B. Kim, “90 Years of Thermal Analysis as a Control Tool in the Melting of Cast Iron,” *China Foundry,* vol. 17, pp. 69-84, 2020.

[144] M. Asif, M. M. Sadiq and M. Muaz, “Heat Transfer Analysis at Mould-Casting Interface for Improving the Casting Process,” in *Advances in Modelling and Optimization of Manufacturing and Industrial Systems: Select Proceedings of CIMS 2021*, Springer Nature, Singapore, 2023, pp. 475-485.

[145] C. S. Greco, G. Paolillo, M. Contino, C. Caramiello, M. Di Foggia and G. Cardone, “3D Temperature Mapping of a Ceramic Shell Mould in Investment Casting Process via Infrared Thermography,” *Quantitative InfraRed Thermography Journal,* vol. 17, no. 1, pp. 40-62, 2020.

[146] T. Sivarupan, N. Balasubramani, P. Saxena, D. Nagarajan, M. El Mansori, K. Salonitis, M. Jolly and M. S. Dargusch, “A Review on the Progress and Challenges of Binder Jet 3D Printing of Sand Moulds for Advanced Casting,” *Additive Manufacturing,* vol. 40, p. 101889, 2021.

[147] I. Rajkumar and N. Rajini, “Metal Casting Modeling Software for Small Scale Enterprises to Improve Efficacy and Accuracy,” *Materials Today: Proceedings,* vol. 46, pp. 7866-7870, 2021.

[148] F. Li, J. Xing and Y. Liu, “Thermal Analysis and Stress Analysis of the Heat-Exchange

Pipe Based on ANSYS," in *2011 Fourth International Conference on Information and Computing*, 2011.

[149] A. K. Soni, S. S. Godara, R. Gade, V. Brenia, R. S. Shekhawat, K. K. Saxena and R. Prasad, "Modelling and Thermal Analysis for Automobile Piston using ANSYS," *International Journal on Interactive Design and Manufacturing (IJIDeM),* pp. 1-15, 2022.

[150] M. C. Nisanci and A. Yurddaş, "Compare between the Results of the Casting Simulation and the Results of Experimental Production with Calculating the Interface Heat Transfer Coefficient of the Casting-Mold," *Celal Bayar University Journal of Science,* vol. 16, no. 2, pp. 169-181, 2020.

[151] S. G. Shabestari and M. Malekan, "Thermal Analysis Study of the Effect of the Cooling Rate on the Microstructure and Solidification Parameters of 319 Aluminum Alloy," *Canadian metallurgical quarterly,* vol. 44, no. 3, pp. 305-312, 2005.

[152] B. Petrus, K. Zheng, X. Zhou, B. G. Thomas and J. Bentsman, "Real-Time, Model-Based Spray-Cooling Control System for Steel Continuous Casting," *Metallurgical and materials transactions B,* vol. 42, pp. 87-103, 2011.

[153] M. Paliwal and I. Jung, "1D Solidification Model for the Prediction of Microstructural Evolution in Light Alloys," in *Computational Materials System Design*, Springer, 2018, p. 89–103.

[154] G. Palumbo, V. Piglionico, A. Piccininni, P. Guglielmi, D. Sorgente and L. Tricarico, "Determination of Interfacial Heat Transfer Coefficients in a Sand Mould Casting Process Using an Optimised Inverse Analysis," *Applied Thermal Engineering,* vol. 78, pp. 682-694, 2015.

[155] A. Ghosh and A. Mallik, Manufacturing Science, Ellis Horwood series in Engineering

Science, 1986.

[156] S. Chakravarti, S. Sen and A. Bandyopadhyay, “A Study on Solidification of Large Iron Casting in a Thin Water Cooled Copper Mould,” *Materials Today: Proceedings,* vol. 5, no. 2, p. 4149–4155, 2018.

[157] R. Conde, M. Parra, F. Castro, J. Villafruela, M. Rodrıguez and C. M´endez, “Numerical Model for Two-Phase Solidification Problem in a Pipe,” *Applied thermal engineering,* vol. 24, no. 17-18, pp. 2501-2509, 2004.

[158] L. Sowa, T. Skrzypczak and P. Kwiaton´, “Impact of Metal Pouring Parameters on Basic Physical Processes,” *Acta Physica Polonica, A,* vol. 138, no. 2, pp. 210-213, 2020.

[159] T. Skrzypczak, E. Węgrzyn-Skrzypczak and L. Sowa, “Numerical Modeling of Solidification Process Taking into Account the Effect of Air Gap,” *Applied Mathematics and Computation,* vol. 321, pp. 768-779, 2018.

[160] R. W. Lewis and K. Ravindran, “Finite Element Simulation of Metal Casting,” *International journal for numerical methods in engineering,* vol. 47, no. 1-3, pp. 29-59, 2000.

[161] L. Liu, Y. Jia, Z. Zhou, Z. Xue and Y. Chen, “Numerical Simulation on Impeller Casting Defects and Optimization,” *Mathematical Problems in Engineering,* vol. 2023, 2023.

[162] G. S. Hanumanth, D. M. Scott and T. J. Smith, “A Numerical Study of Heat Transfer during Flow of Melt in a Cylindrical Mould,” *Applied scientific research,* vol. 46, pp. 323-333, 1989.

[163] A. Özdemir, O. N. U. R. A. L. P. Uluer and A. Güldaş, “Flow Front Advancement of Molten Thermoplastic Materials during Filling Stage of a Mold Cavity,” *Polymer Testing,* vol. 23, no. 8, pp. 957-966, 2004.

[164] T. Lochmatter, X. Raemy, L. Matthey, S. Indra and A. Martinoli, “A Comparison of Casting and Spiraling Algorithms for Odor Source Localization in Laminar Flow,” in *2008 IEEE International Conference on Robotics and Automation*, 2008.

[165] S. M. Hosseini and E. Amani, “An Improved Combination of Ruler and Local Electromagnetic Brakes for Continuous Casting Process,” *Journal of Manufacturing Processes,* vol. 85, pp. 1037-1053, 2023.

[166] T. Wang, J. Zhou, L. Wang, Z. Zhang, H. Zhang and X. Xia, “Research and Development of Gating and Riser Process Optimization Integrated System for Steel Casting,” *International Journal of Metalcasting,* pp. 1-17, 2023.

[167] C. Bate, P. King, J. Sim and G. Manogharan, “A Novel Approach To Visualize Liquid Aluminum Flow To Advance Casting Science,” *Materials,* vol. 16, no. 2, p. 756, 2023.

[168] A. K. Eqal and J. A. Yagoob, “Prediction of the Solidification Mechanism of ZA Alloys Using Ansys Fluent,” *Journal of Applied Science and Engineering,* vol. 24, no. 5, pp. 699-706, 2021.

[169] G. C. Nzebuka, C. O. Ufodike and C. P. Egole, “Influence of Various Aspects of Low-Reynolds Number Turbulence Models on Predicting Flow Characteristics and Transport Variables in a Horizontal Direct-Chill Casting,” *International Journal of Heat and Mass Transfer,* vol. 179, p. 121648, 2021.

[170] I. Ansys, ANSYS Fluent User’s Guide, Release 19.0, Canonsburg: ANSYS Inc, 2018.

[171] S. V. Shepel and S. Paolucci, “Numerical Simulation of Filling and Solidification of Permanent Mold Castings,” *Applied Thermal Engineering,* vol. 22, no. 2, pp. 229-248, 2002.

[172] W. C. Reynolds, “Computation of Turbulent Flows,” *Annual Review of Fluid Mechanics,*

vol. 8, no. 1, pp. 183-208, 1976.

[173] V. Nikora, I. McEwan, S. McLean, S. Coleman, D. Pokrajac and R. Walters, "Double-Averaging Concept for Rough-Bed Open-Channel and Overland Flows: Theoretical Background," *Journal of hydraulic Engineering,* vol. 133, no. 8, pp. 873-883, 2007.

[174] A. C. Kheirabadi and D. Groulx, "The Effect of the Mushy-Zone Constant on Simulated Phase Change Heat Transfer," in *Proceedings of CHT-15. 6 th International Symposium on Advances in Computational Heat Transfer*, Begel House Inc., 2015, pp. 528-549.

[175] V. Ramaj, A. Dhori, K. Dhoska, A. Koleci and E. Konjusha, "CFD Code Turbulence Models Validation for Turbulent Flows over a Wavy Surface," in *Annals of DAAAM & Proceedings*, Vienna, Austria, EU, 2010.

[176] E. Saredi, N. T. Ramesh, A. Sciacchitano and F. Scarano, "State Observer Data Assimilation for RANS with Time-Averaged 3D-PIV Data," *Computers & Fluids,* vol. 218, p. 104827, 2021.

[177] S. Laın, D. Bröder, M. Sommerfeld and M. F. Göz, "Modelling Hydrodynamics and Turbulence in a Bubble Column using the Euler–Lagrange Procedure," *International journal of multiphase flow,* vol. 28, no. 8, pp. 1381-1407, 2002.

[178] H. Enwald, E. Peirano and A. E. Almstedt, "Eulerian Two-Phase Flow Theory Applied to Fluidization," *International Journal of Multiphase Flow,* vol. 22, pp. 21-66, 1996.

[179] B. Sun, "Revisiting the Reynolds-Averaged Navier–Stokes Equations," *Open Physics,* vol. 19, no. 1, pp. 853-862, 2022.

[180] J. Aubin, D. F. Fletcher and C. Xuereb, "Modeling Turbulent Flow in Stirred Tanks With CFD: The Influence of the Modeling Approach, Turbulence Model and Numerical Scheme," *Experimental thermal and fluid science,* vol. 28, no. 5, pp. 431-445, 2004.

[181] P. A. Durbin, “A Reynolds Stress Model for Near-Wall Turbulence,” *Journal of Fluid Mechanics,* vol. 249, pp. 465-498, 1993.

[182] V. F. Nicolette, S. R. Tieszen, A. R. Black, S. P. Domino and T. J. O’Hern, “A Turbulence Model for Buoyant Flows Based on Vorticity Generation,” Sandia National Laboratories, Sandia Report SAND2005-6273, 2005.

[183] W. M. Kays, “Turbulent Prandtl Number. Where are we?,” *ASME Journal of Heat Transfer,* vol. 116, no. 2, pp. 284-295, 1994.

[184] R. A. W. M. Henkes, F. F. Van Der Vlugt and C. J. Hoogendoorn, “Natural-Convection Flow in a Square Cavity Calculated with Low-Reynolds-Number Turbulence Models,” *International Journal of Heat and Mass Transfer,* vol. 34, no. 2, pp. 377-388, 1991.

[185] C. Teodosiu, V. Ilie and R. Teodosiu, “Appropriate CFD Turbulence Model for Improving Indoor Air Quality of Ventilated Spaces,” *Modelling in Civil Environmental Engineering,* vol. 10, no. 4, pp. 28-42, 2014.

[186] G. E. Hassan, A. Hassan and M. E. Youssef, “Numerical Investigation of Medium Range Re Number Aerodynamics Characteristics for NACA0018 Airfoil,” *CFD letters,* vol. 6, no. 4, pp. 175-187, 2014.

[187] M. Fulgosi, D. Lakehal, S. Banerjee and V. De Angelis, “Direct Numerical Simulation of Turbulence in a Sheared Air–Water Flow with a Deformable Interface,” *Journal of fluid mechanics,* vol. 482, pp. 319-345, 2003.

[188] V. R. Voller and C. Prakash, “A Fixed Grid Numerical Modelling Methodology for Convection-Diffusion Mushy Region Phase-Change Problems,” *International journal of heat and mass transfer,* vol. 30, no. 8, pp. 1709-1719, 1987.

[189] I. Calderón-Ramos, R. D. Morales, R. Servín-Castañeda, A. Pérez-Alvarado, S. García-

Hernández, J. de Jesús Barreto and S. A. Arreola-Villa, “Modeling Study of Turbulent Flow in a Continuous Casting Slab Mold Comparing Three Ports SEN Designs,” *ISIJ International,* vol. 59, no. 1, pp. 76-85, 2019.

[190] S. Galván, M. Reggio and F. Guibault, “Assessment Study of K-Ɛ Turbulence Models and Near-Wall Modeling for Steady State Swirling Flow Analysis in Draft Tube,” *Engineering Applications of Computational Fluid Mechanics,* vol. 5, no. 4, pp. 459-478, 2011.

[191] M. Rohani and M. H. Afshar, “Simulation of Transient Flow Caused by Pump Failure: Point-Implicit Method of Characteristics,” *Annals of Nuclear Energy,* vol. 37, no. 12, pp. 1742-1750, 2010.

[192] M. Xu, M. Isac and R. I. Guthrie, “A Numerical Simulation of Transport Phenomena during the Horizontal Single Belt Casting Process using an Inclined Feeding System,” *Metallurgical and Materials Transactions B,* vol. 49, pp. 1003-1013, 2018.

[193] R. M. Barron and A. A. Salehi Neyshabouri, “Effects of Under-Relaxation Factors on Turbulent Flow Simulations,” *International journal for numerical methods in fluids,* vol. 42, no. 8, pp. 923-928, 2003.

[194] P. D. Nation, J. R. Johansson, M. P. Blencowe and A. J. Rimberg, “Iterative Solutions to the Steady-State Density Matrix for Optomechanical Systems,” *Physical Review E,* vol. 91, no. 1, p. 013307, 2015.

[195] M. Wu, M. Ahmadein and A. Ludwig, “Premature Melt Solidification during Mold Filling and its Influence on the As-cast Structure,” *Frontiers of Mechanical Engineering,* vol. 13, pp. 53-65, 2018.

[196] J. Campbell, Complete Casting Handbook: Metal Casting Processes, Metallurgy,

Techniques and Design, New York: Elsevier Science, 2015.

[197] M. N. Özışık, Heat Transfer: A Basic Approach, New York: McGraw-Hill, 1985.

[198] D. M. Stefanescu, "Computer Simulation of Shrinkage Related Defects in Metal Castings–A Review," *International Journal of Cast Metals Research,* vol. 19, no. 3, pp. 129-143, 2005.

[199] S. Santhi, B. R. Surya, Jairam, S., J. Jhansi and P. K. S. Subramanian, "Design of Gating and Riser System for Grate Bar Casting," *Indian Foundry Journal,* vol. 61, no. 1, 2015.

[200] K. Ravindran, R. W. Lewis and S. E. Navti, "Effect of Reynolds Number on the Simulated Filling Pattern of a Bench Mark Mould Filling Problem," *International Journal of Cast Metals Research,* vol. 10, no. 5, pp. 283-291, 1998.

[201] P. Roache, "Perspective: A Method for Uniform Reporting of Grid Refinement Studies," *ASME Journal of Fluid Engineering,* vol. 116, pp. 405-413, 1994.

[202] C. M. Choudhari, N. S. l Dalal, A. P. Ghude, P. P. Sankhe and A. M. Dhotre, "Design and Analysis of Riser for Sand Casting," *International Journal of Students Research in Technology & Management,* vol. 1, no. 2, pp. 176-191, 2013.

[203] C. Xu, J. Zhao, A. Guo, H. Li, G. Dai and X. Zhang, "Effects of Injection Velocity on Microstructure, Porosity and Mechanical Properties of a Rheo-Diecast Al-Zn-Mg-Cu Aluminum Alloy," *Journal of Materials Processing Technology,* vol. 249, p. 167–171, 2017.

[204] K. K. Alanemea and A. O. Alukob, "Production and Age-Hardening Behaviour of Borax Premixed Sic Reinforced Al-Mg-Si Alloy Composites Developed by Double Stir-Casting Technique," *The West Indian Journal of Engineering,* vol. 34, no. 1, p. 2, 2012.

[205] H. Thomas, A. Samad and A. M S, “Particle Distribution Simulation of Functionally Graded Az91-SiCp Composite Fabricated by Centrifugal Casting,” in *Proceedings of the International Conference on Systems, Energy and Environment 2022 (ICSEE 2022)*, 2022.

[206] H. Cao, C. Shen, C. Wang, H. Xu and J. Zhu, “Direct Observation of Filling Process and Porosity Prediction in High Pressure Die Casting,” *Materials,* vol. 12, no. 7, p. 1099, 2019.

[207] K. Kumari and S. Yadav, “Linear Regression Analysis Study,” *Journal of the practice of Cardiovascular Sciences,* vol. 4, no. 1, p. 33, 2018.

Sumit chakravarti
26/06/2023